TRANSITION FROM LAMINAR TO TURBULENT FLOW

Qualification of a Supersonic Test Section in a Compression-tube Wind Tunnel

Henny Bottini

Turbomachinery and Propulsion Department, von Karman Institute for Fluid Dynamics, Belgium, bottini@vki.ac.be

Supervisor: Guillermo Paniagua

Associate Professor, Turbomachinery and Propulsion Department, von Karman Institute for Fluid Dynamics, Belgium, paniagua@vki.ac.be.

Abstract

The qualification of a reduced-noise test section for supersonic transition experiments at different Mach numbers is presented. The low-disturbances environment was analyzed by both hot-wire measurements and the assessment of the boundary layer status along the wind-tunnel walls. Maps of the flow static pressure around and downstream of a single roughness element were made by the use of Pressure Sensitive Paint with the lifetime and the intensity methods.

Keywords: Supersonic flow, wind tunnels, mass-flow fluctuations, boundary-layer, Pressure-Sensitive Paint, wall shear stress quantification, thin oil film

1. Introduction

In air-breathing engines, the status of the boundary layer along the intake surface dictates the aerothermal performance. This paper presents the qualification of a quiet wind tunnel to study roughness induced boundary layer transition in an adjustable supersonic regime (M_∞ from 1.5 to 2.2) with Reynolds varying from 3 to $4.6 \cdot 10^7 \; m^{-1}$.

At the intake where pressure gradients and shocks appear the boundary layer should be adequately predicted and controlled. A turbulent boundary layer is more robust than a laminar one, but the higher aerothermal losses must be properly accounted for in the combined vehicle-engines design.Consequently, transition experiments are required to identify the transition onset and the driving physical phenomena. This kind of experiments, however, requires a facility that does not interfere with the transition process on the test article. At the considered supersonic Mach numbers, the facility must not produce strong pressure fluctuations. Namely, the RMS in pressure should be less than 1% of p_∞ [1]. In order to extrapolate the wind tunnel data towards real flight conditions, also the wind tunnel fluctuations should be bounded [2]. Harvey in [3] proved that the main cause of pressure fluctuations inside the test section of a supersonic wind tunnel is the turbulent boundary layer on the test section walls, which radiates pressure disturbances onto the test article. Therefore, the solution for having meaningful transition experiments is to keep the boundary layer laminar on those walls, that is, to have a ”quiet wind tunnel”. The present paper presents results by an oil-dot technique to assess the boundary layer status on the facility internal walls, and by hot-wire measurements to quantify the intensity of the free-stream mass-flow fluctuations.

The first test campaign in the qualified supersonic wind tunnel aimed at mapping the pressure field produced by a single three-dimensional roughness in a supersonic boundary layer. These maps are produced by Pressure Sensitive Paint applied all around the roughness element. Its capabilities were exploited with two different methods, the lifetime method and the intensity method. Both are presented in their main aspects and with their results, along with the paint calibration method and process.

2. Wind Tunnel Qualification

The first tests of this new wind tunnel have been dedicated to its qualification. Firstly the correctness of the wind tunnel starting, i.e. the presence of a shock-free supersonic expansion in the divergent, has been verified experimentally. Secondly, the tests focused on measurement of the wind tunnel noise, i.e. they assessed the wind tunnel degree of quietness.

2.1. Practical Mach range achievable

The result of the first wind tunnel qualification campaign is the Mach range achievable in practice. The tests of this campaign were run without test article in the test section. The absence of the shock was verified by the use of fifteen pressure taps drilled on the ends of the two ramps that constitute the divergent of the nozzle (ten taps on the upper ramp and five on the lower ramp). They measured the static pressure at the wall along an axial length of 36 *cm* from the location of the test article leading edge to the very end of the nozzle. The measurements were then compared with pressure and Mach number axial evolutions by a quasi-1D calculations of the supersonic shock-free expansion corresponding to the same total quantities as those of the run. The comparison between the calculations and the measurements is illustrated by Fig. 1 for the static pressure and by Fig. 2 for the Mach number.

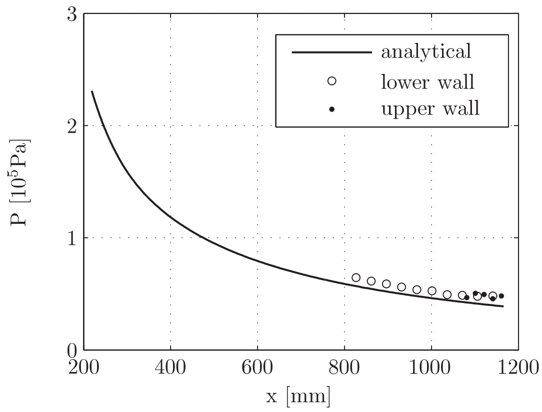

Figure 1: Typical static pressure axial evolution throughout the whole nozzle divergent (p_0=4.2 bar)

Figure 1 and 2 show how the measured pressure and Mach number evolution along the divergent matches very satisfactorily the theoretical evolution. This means that no shock wave is present in the divergent, that is the wind tunnel is correctly started by the total pressure value selected for the test. At this point Table 1 presents the Mach-number range achievable by the wind tunnel along with the corresponding unit Reynolds numbers, test times, and total pressures of the tests. Note that as test Mach number is considered the one reached by the flow in the divergent at the axial position of 80 *cm* from the throat.

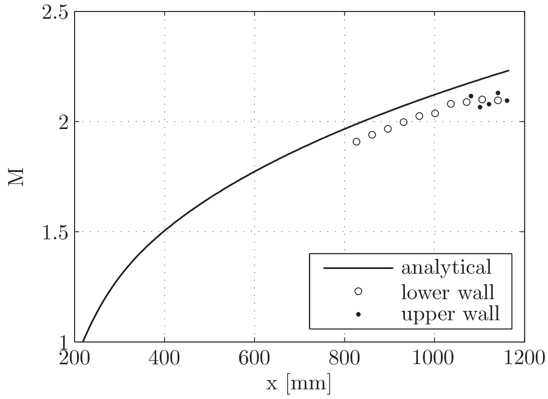

Figure 2: Typical Mach number axial evolution throughout the whole nozzle divergent (p_0=4.2 bar)

Table 1: Mach number range, unit Reynolds numbers and test times of the wind tunnel

Mach number	unit Re 10^7 m^{-1}	test time [ms]	p_0 [bar]
1.55	3	600	3
1.72	3	800	3
1.93	4	750	4.2
2.12	4.6	1100	5

2.2. Assessment of wind-tunnel noise

As stated in the preceding, a quiet wind-tunnel must generate very low disturbances and these are mainly due to the turbulent boundary layer along the wind tunnel walls. However, also free-stream fluctuations play a role at supersonic Mach numbers and they are generated in the most upstream parts of the facility. Here are presented the results of the experiments made to assess the boundary layer status on the wind tunnel walls and the intensity of free-stream turbulence for different Mach numbers.

2.2.1. Assessment of the boundary-layer state on the wind-tunnel walls

One of the major features of a quiet wind tunnel should be a laminar boundary layer along the test section wall. If this is not possible throughout the entire test section, at least it should go as far downstream as not to radiate turbulence noise directly onto the test article. As stated in the introduction, the bleeding slots at the throat have been designed for this purpose. Then we had to assess the effectiveness of this design by looking at the state of the boundary layer on the wind tunnel walls. This was done by measuring the shear stress on the tunnel walls using a novel technique, the thin oil film method [4].

The thin oil film method relies on the principle that the rate at which oil thins along a surface flown by a fluid is function of the wall shear stress due to the flow. This principle, in turn, relies on the thin-film theory which, thence, represents the mathematical foundation of the technique here tried.

Squire, one of the principal contributors to thin-film theory, demonstrated that oil flows in the direction of the boundary layer skin friction, except near separation. (In this latter case, in fact, it tends to indicate separation earlier than in the absence of oil.) His model of the motion of the thin film in two dimensions is

$$\frac{\partial h}{\partial t} + \frac{\partial h U_c}{\partial x} + \frac{\partial h W_c}{\partial z} = 0 \tag{1}$$

with h the oil film thickness, and U_c and W_c the oil velocities averaged along the x and z directions. Expression for U_c and W_c were derived from the momentum equations in the same way. Here this derivation is presented for U_c.

The convection (inertial) term in the momentum equation of the oil moving under the effect of the flow, and the velocity gradients in the directions other than the normal to the surface are neglected. The resulting simplified equation is integrated twice with the boundary conditions that oil velocities are equal to those in the boundary layer at the surface of the oil, that the viscous stresses in the oil and the air are equal at the oil/air surface, and that at the body surface the oil is stationary. The results is this expression for oil velocity

$$u = \frac{1}{\mu}\left(\frac{\partial P}{\partial x} - \rho g_x\right)\left(\frac{y^2}{2} - hy\right) + \frac{\tau_w}{\mu} y \tag{2}$$

The oil velocity then becomes function of: the pressure gradient and the volume forces in the direction of the oil motion; viscosity and the wall shear stress; and film thickness, h, along with the height above the surface $y \in [0 \div h]$. Now taking the average over y of the velocity one obtains an expression without dependency on y, i.e. for U_c

$$U_c = \frac{\tau_{w,x} h}{2\mu} - \frac{h^2}{3\mu}\left(\frac{\partial P}{\partial x} - \rho g_x\right) \tag{3}$$

Repeating the same analysis for the z-direction yields

$$W_c = \frac{\tau_{w,z} h}{2\mu} - \frac{h^2}{3\mu}\left(\frac{\partial P}{\partial x} - \rho g_z\right) \tag{4}$$

Introducing both Eqs. 3 and 4 in Eq. 1 one obtains the equation

$$\frac{\partial h}{\partial t} + \frac{\partial}{\partial x}\left[\frac{\tau_{w,x} h^2}{2\mu} - \frac{h^3}{3\mu}\left(\frac{\partial P}{\partial x} - \rho g_x\right)\right] + \frac{\partial}{\partial z}\left[\frac{\tau_{w,z} h^2}{2\mu} - \frac{h^3}{3\mu}\left(\frac{\partial P}{\partial x} - \rho g_z\right)\right] = 0 \tag{5}$$

which, considering that the effects of pressure gradient and volume forces are often negligible, finally reads

$$\frac{\partial h}{\partial t} + \frac{\partial}{\partial x}\left[\frac{\tau_{w,x} h^2}{2\mu}\right] + \frac{\partial}{\partial z}\left[\frac{\tau_{w,z} h^2}{2\mu}\right] = 0 \tag{6}$$

Tanner, afterwards, completed the theory and made it more usable by assuming that the oil film profile depends only on the shear stress variation in x [4, and refs. therein] as

$$h = \frac{\mu}{t\sqrt{\tau_w}} \int_0^x \frac{dx}{\sqrt{\tau_w}} \tag{7}$$

here h is the height of the oil film at x and time t. This equation then becomes trivial if the shear stress at the wall can be considered constant in x varying from 0 to L:

$$h = \frac{\mu L}{t \tau_w} \tag{8}$$

It is thus possible to deduce τ_w from the slope of the oil surface because Eq. 8 will hold near the leading edge of the moving film for any shear stress distribution. Finally, small distributed oil droplets, instead of a uniform film over the entire surface, allow to consider the wall shear stress constant so to comply with the assumption at the basis of Eq. 8.

Since the measurements are done on one part of the nozzle divergent, the boundary layer flow is subject to a non-negligible favorable pressure gradient, thus a check of the above derived equations validity with this new term accounted for was in need. An order-of-magnitude analysis of Eq. 5 confirmed that, despite the pressure gradient term increased its relative weight, it was still one order of magnitude lower than the wall shear-stress term. This means that the equation of the thin film theory is still valid and can be applied also for the wall shear stress measurement on the current case.

In practice, every test consisted in putting dots on the surface of the lower ramp constituting a part of the divergent of the nozzle, and recording their deformation by means of a high-speed camera viewing from one side into the facility (Fig. 3). In every test a variable number of dots arranged on one or two rows was layered.

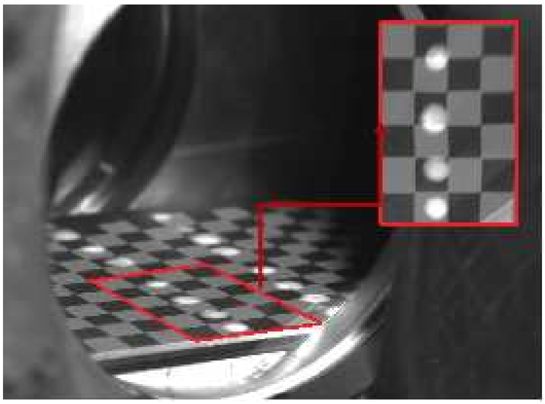

Figure 3: Oil dots on a checkered area for the reference image

In order to accurately analyze the recorded temporal evolution of the dots, an algorithm was developed in Matlab®. It reads the high-speed-camera video frame by frame, implements a correction to the images distorted by the non-orthogonal view, selects a specific dot on the initial frame, and computes the deformation of that dot throughout all the frames, i.e. in time, up to the test end. In this way Eq. 8 can be applied to extract the wall shear stress value.

To obtain the area and the longitudinal deformation of the dot in S.I. units a reference image with a chessboard over the surface is used (Fig. 3). It also served for the image correction mentioned above.

A total of six tests was performed and the main results are presented in Fig. 4

Here, one sees the experimental results for each dot on a row (+) and their average over the row (o) compared with CFD laminar calculations of the flow in the divergent of the nozzle. ε is the difference between the average value and the CFD reference value for the same position along the nozzle. It is evident that the measurements lay always below the computed laminar values so to allow the conclusion that the boundary layer is not turbulent, i.e. it is laminar. This result was found also for M_∞ equal to 2 and 2.2. The oil-dot technique then proves itself a simple yet useful way to assess the boundary layer status, but not yet a technique for shear stress measurements because of the still high inaccuracy shown by Fig. 4. In the end one can conclude that this serious source of noise is avoided in the present supersonic facility, and it was

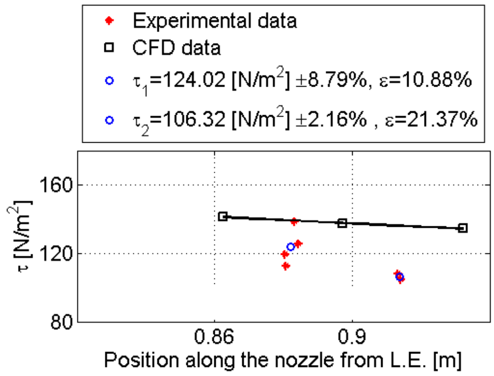

Figure 4: Measured shear/stress values at two different locations (M_∞ = 1.9)

only left to measure the other important one: the free-stream turbulence intensity. This is presented in the next subsection.

2.2.2. Hot-wire measurements of free-stream turbulence intensity

The free-stream turbulence measurements consisted in the measurements of the mass-flow fluctuations, and were made by a double hot-wire probe mounted on a boom on the axis of the test section (see Fig. 5). The hot-wires were of the constant-temperature type, Platinum-coated, 3-mm long, and had a diameter of 9 μm. Only the wire with the highest over-heating ratio ($R_w/R_a = 1.6$) was used for the measurements. The hot-wire electronics allowed a maximum frequency resolution of 20 kHz. A total of seven tests was performed.

Figure 5: The double hot-wire in the test section

The hot-wire calibration was made *in situ*, i.e. at the same time as the measurements. The mean flow quantities in each test were calculated from p_0, p and T_0 measurements, and time intervals in which they were mostly constant were singled out of the entire test duration. Then, the mean values of ρU were plotted against the corresponding hot-wire voltage outputs so to have a calibration curve of the type $E^2 = A + B(\rho U)^{0.5}$ for each test. From this calibration function, the inverse function $(\rho U) = f(E)$ was obtained and applied to the time-dependent hot-wire output to get the values of the mass-flow fluctuations $\rho U'$.

The upper limit of the fluctuations frequency range, as stated in the preceding, was set by the electronics used at 20 *kHz*, whilst for the lower limit some considerations had to be done. It has been soon evident that the entire facility vibrated during each test, and so did the boom hosting the hot-wire. These low-frequency mechanical vibrations were however recorded by the hot-wire as flow fluctuations and thus they had to be removed from the hot-wire measurements during the signal post-processing. An estimation of the range of these vibrations has been possible thanks to some previous tests made with a flat plate mounted as a cantilever in the test section and equipped with an accelerometer (Figs. 6 and 7). The frequency spectrum of the plate mechanical vibrations is reported in Fig. 8. Even if the mechanical system composed by the plate and its supporting beams differed from that comprised of the boom and its support (the attachment to the wind tunnel was the same, instead), we considered the accelerometer data still as a good estimation of the mechanical vibrations suffered by the hot-wire.

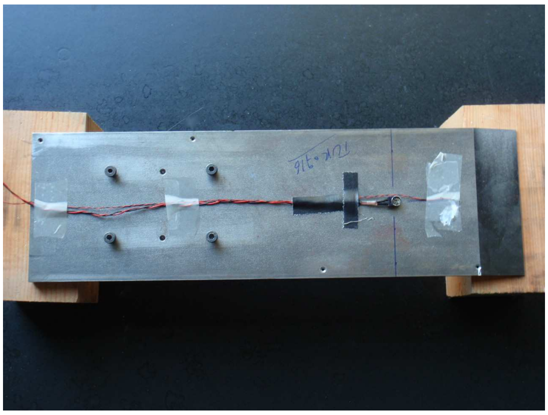

Figure 6: The accelerometer used for mechanical-vibrations measurements glued on the flat plate

One can see that the strongest vibrations occur for a frequency less than 700 *Hz*, thus this value has been used as the lower limit of the $\rho U'$ frequency range.

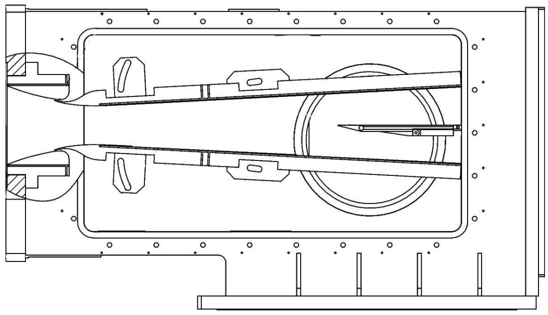

Figure 7: The flat plate with the accelerometer in the test section

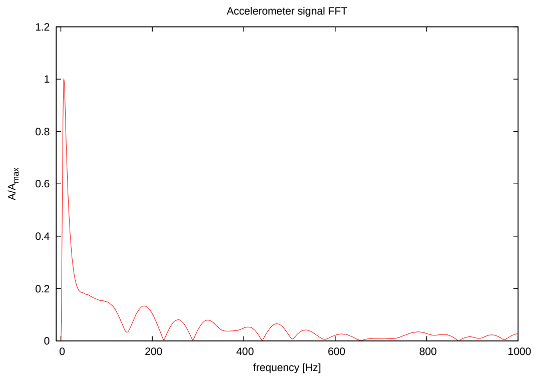

Figure 8: Frequency spectrum of mechanical vibrations of a flat plate in CT2

In conclusion, the free-stream mass-flow intensities measured in the frequency range [700÷20000] *Hz* are reported in Table 2 for two different Mach numbers. These values are reported in Fig. 9 where they can

Table 2: Free-stream mass-flow fluctuations

M_∞	unit Re	$\rho U'$
	10^7 m^{-1}	$\frac{RMS}{\rho U}$
1.72	3	0.63%
1.93	4	1.14%

be compared with data form other supersonic facilities. Here are shown (linked by lines) data measured in the 1960' in a JPL supersonic quiet wind tunnel as reported in [5], plus additional data about free-stream mass-flow disturbances in the Russian ITAM wind tunnels T313 and T325. The JPL wind-tunnel features a 1%-turbulence settling chamber with four screens and one air filter; the ITAM T325 features a settling chamber with honeycomb, ten screens, and a not-further-detailed noise–reduction system, whilst the T313 is reported as conventional.

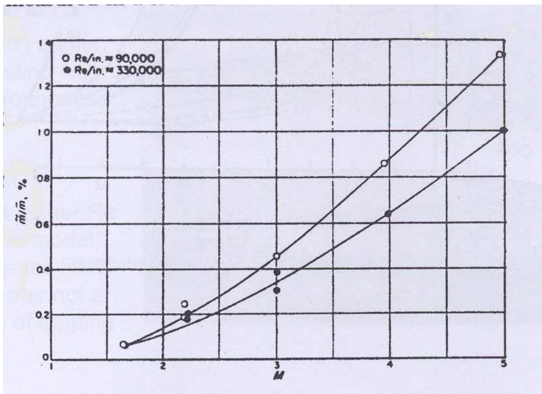

Figure 9: Variation of mass-flow fluctuations with free-stream Mach number, [5]

Regarding the JPL data, the curve of interest for the comparison is that for the unit Reynolds number equal to ($1.3 \cdot 10^7 m^{-1}$) that features an interpolated value of about 0.1% for the Mach numbers tested in the present work. This means that the values measured are six to ten times those of this quiet wind tunnel. These values are typical of non-quiet wind tunnels, like confirmed by the value from the ITAM T313, even if at a higher Mach number, and by the values of the T325 used at transonic conditions; in this latter case, the T325 resulted noisier than as operated at supersonic conditions. In effect such a result does not come as a surprise: in the present wind tunnel there are none of the low-turbulence-level characteristics of the JPL and ITAM facilities.

The modifications to the facility general layout needed to implement these characteristics, in fact, would affect the compression tube itself, its air inlet from the high-pressure supply system, and its outlet to the test section, so that the entire structure of the wind tunnel would be heavily changed. This change could then conflict with the actual primary purpose of the wind tunnel, which is turbo-machinery air-foil testing, and for this reason has not been implemented so far.

3. Pressure-Sensitive-Paint measurements: pressure field around a roughness in a supersonic boundary layer

The first test campaign to be performed in the qualified wind tunnel aimed at proving the capabilities of a rather interesting non-intrusive pressure-field measurement technique: the Pressure Sensitive Paint, [6]. This technique consists in laying on the surface, whose pressure is to map, a special paint that consists of luminescent molecules in an oxygen-permeable binder. During the measurement these molecules are excited by an external pulsing light source (e.g., lasers, LEDs, or a gas discharge lamp) and start emitting light at a wavelength larger than that of the excitation. The physical phenomenon that makes the pressure measurement possible is that the intensity and luminescent lifetime of the emitted light are sensitive to the ambient concentration of Oxygen, which is proportional to the Oxygen partial pressure, which in turn is proportional to the local static pressure of the flow. Therefore, one can recover the local static pressure on each point of the PSP-coated surface by detecting the emitted light (by photomultiplier tubes or digital cameras) and by using the following Sterner-Volmer equation to relate its intensity or lifetime to static pressure and values taken at a reference condition

$$\frac{I_{ref}}{I} = \frac{\tau_{ref}}{\tau} = A(T) + B(T)\frac{p}{p_{ref}} \qquad (9)$$

In Eq.9 I is the light intensity, τ the lifetime, and p the static pressure. A and B are the Sterner-Volmer coefficients and must be obtained by the calibration of the paint. They both depend on the paint temperature because of the *"Oxygen quenching"* that alters the paint response as the temperature increases. This effect consists in the luminophore molecule returning to the un-excited state by colliding with an Oxygen molecule instead of by emitting light. The intensity of this quenching is directly proportional to the concentration of Oxygen in the paint binder, which in turn is directly proportional to the binder permeability to Oxygen. This finally is directly proportional to paint temperature according to an Arrhenius relationship [6, and reference therein].

The intensity method is the most straightforward. A continuous illumination excites the paint, and a camera records the intensity of the paint emission. The camera has a filter to avoid the mixing of the light emitted and the light just reflected by the paint. This technique requires a normalization of each image with a "wind-o" reference in order to compensate variations in the local paint properties, e.g. thickness or luminophore concentration.

The lifetime technique is more complex and only recently has became attractive because of the improvements in camera sensitivity and dynamic range. In practice, lifetime measurements are (often) carried out using a pulsed illumination and a gated CCD camera that acquires at least two subsequent images, some (one) during and some (one) after the excitation. Each image is an integration of the paint emission intensity over the camera gate time. The intensity ratio computed from the image taken after the excitation and that taken during is proportional to the emission lifetime, thus to the static pressure as from Eq. 9.

During the present investigation both the intensity and lifetime techniques were investigated, so the binary PtTFPP/FIB PSP paint, by Innovative Scientific Solutions Inc. (ISSE), was calibrated for both of them.

3.1. PSP calibrations for the lifetime and the intensity methods

The calibration setup consisted of five pulsed high-power LEDs as light source; two long-pass optically-filtered LaVision Imager Intense CCD cameras as a detector (during the first calibrations);and the sample model painted with the PSP . The latter was equipped with electric heaters and a thermocouple to calibrate in the temperature range $T \in [0 \div 60]\ ^0$C. This range was selected by accounting for the maximum recovery temperature of the flow during the supersonic tests of the paint, i.e. the maximum temperature experienced by the paint during the short-duration tests. The sample was placed in a vacuum chamber instrumented with a pressure tap and with an inlet from an air pump to set the pressure values for the calibration (Fig. 10).

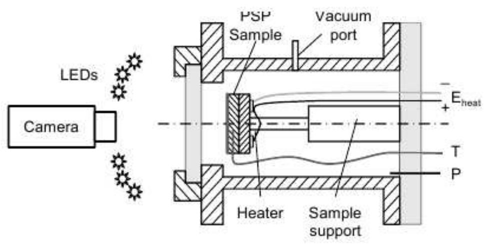

Figure 10: Sketch of the calibration setup

Two samples with twelve and fifteen layers of paint were used to assess paint thickness effect. Pressures ranging from about 10^4 *Pa* to ambient pressure were tested. Twenty pairs of images were taken for each calibration point.

In case of the lifetime calibration and in order to nd the optimum timing for the cameras a large number of gate combinations and durations were tested. The best results were obtained for a rst exposure of 400 μs that was started 100 μs after the beginning of the LED light pulse. The illumination was switched o after 500 μs. At this moment the exposure of the second camera began. In order to integrate over the complete exponential decay, the length of exposure two was set to 200 μs.Selected data sets and the mean calibration curve obtained with the life-time technique are shown in Fig. 11

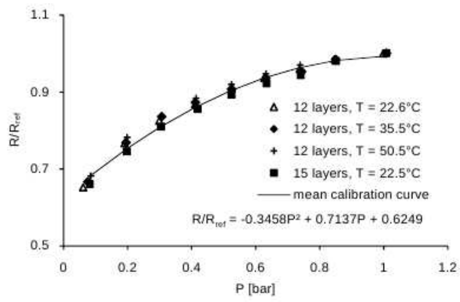

Figure 11: Calibration of binary PSP for dierent sample temperature and paint thickness(lifetime method)

The ratio R between the image taken before and that taken after the paint excitation was normalized with the ratio at 1 *bar*, R_{ref}. Figure 11 shows that neither a variation of the sample temperature nor a change of the paint thickness lead to a meaningful discrepancy between the mean calibration curve and the data points.

In case of the intensity calibration the results are summarized by Fig. 12. Now the two sets of data points illustrate the good reproducibility of the calibration. The higher intensities of these images lead to a better signal-to-noise ratio, hence to a fair agreement with the mean calibration curve. A quadratic least square fit was applied resulting in a regression coefficient, $R2$, of 0.9985.

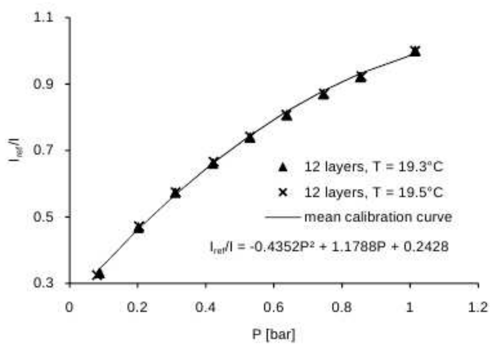

Figure 12: Calibration of binary PSP for dierent sample temperature and paint thickness(intensity method)

3.2. PSP test results

The tests consisted in mapping the pressure field generated by a single roughness element ($h \times w \times l = 5 \times 4 \times 4\ mm^3$) glued onto the lower nozzle-wall and invested by a $M_\infty = 1.8$ flow (Fig. 13). The pressure sensitive paint was applied around and downstream of the roughness by the use of an airbrush. Thin layers of paint were alternately applied in left-right and up-down passes until a uniform layer was achieved. The pressure taps were not covered in order to maintain a smooth surface. Since very thin layers of paint were applied, the inlets of the static pressure taps were only very slightly aected and could still serve efficiently for obtaining the static pressure evolution along the nozzle. One pressure tap was equipped with fast reference pressure transducers to allow assessing the paint temporal response to the pressure drop at the beginning of the test.

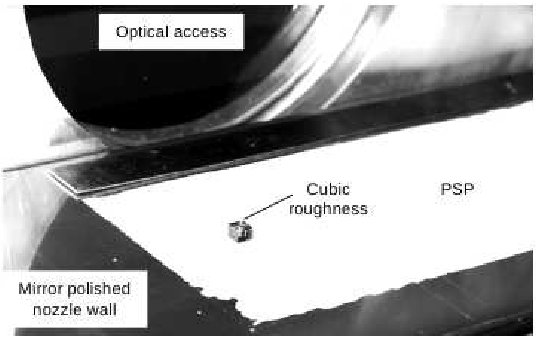

Figure 13: The PSP applied around a cubic roughness

Figure 14 shows the pressure map by the intensity method and Fig. 15 that by the lifetime method.

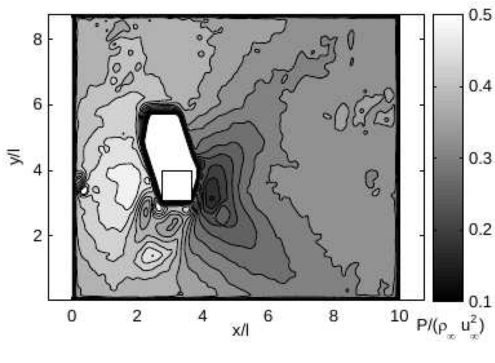

Figure 14: PSP map of the static pressure field around a single roughness element in a $M_\infty = 1.8$ flow, $l = 4\ mm$ (intensity method)

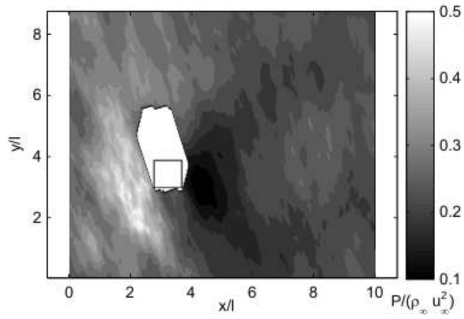

Figure 15: PSP map of the static pressure field around a single roughness element in a $M_\infty = 1.8$ flow, $l = 4\ mm$ (lifetime method)

In both pictures the static pressure values are expressed relatively to the dynamic pressure. The image of the roughness looks very elongated because of the geometrical correction needed by the non-orthogonal angle of view of the cameras; the square drawn at the basis of this white zone signals the right position of the roughness respect to the pressure field.

In Fig. 14 the pressures range from approximately 250 *mbar* in the wake of the roughness to about 1000 *mbar* in the stagnation region upstream of the cuboid. The high pressure region has a semi-circular shape most likely due to the detached bow shock in front of the roughness. The triangular low pressure branches emanating at an angle of approximately 45 deg from the rear corners of the cuboid are likely related to an expansion into the wake. That is, the flow is displaced by the roughness and its wake, because as the streamlines go around the cuboid they acquire a convex curvature that leads to an expansion. Further downstream they turn to a concave curvature tending to the centreline and turning in the stream-wise direction of the mean flow-field. This in turn leads to a compression of the flow. Throughout this compression the pressure increases gradually and adapts to the mean static pressure downstream of the roughness. The low pressure regions get narrower with span-wise distance from the centreline because the displacement effect of the roughness, and hence the curvature of the streamlines, is weaker and weaker. Finally, the very low pressure at the back of the roughness indicates the typical recirculation zone to be expected in that position.

The same qualitative pattern as in Fig. 14 is observed in the pressure map shown in Fig. 15. Although the spatial resolution can be considered still good, camera sensitivity had to be sacrificed. This led to a reduced signal-to-noise ratio that caused less distinctive pressure contours and an underestimation of the overall pressure levels if compared to the intensity measurements. However, in the end the stagnation region upstream and the low pressure footprint downstream of the rectangular roughness, i.e. the major features of the flow, can still be identified.

The difference in the results from the two methods is because the experiments were performed with the same hardware. For the intensity based method, long, i.e. hardware-wise less-demanding, camera exposures, were required and the hardware was capable of a good signal to noise ratio. For the lifetime method, instead, shorter exposures were needed and the hardware performed with a lower signal to noise ratio.

The intensity method allows a longer time during which the camera can integrate the paint luminescence and, in the end, yield a higher signal levels, thus a better pressure resolution. The lifetime method, instead, requires (kept the hardware, i.e. the camera, the same) a stronger conditioning of the data in the post-processing of the images. This consisted in a more important *"binning of the pixels"*, that is, the combination of the signal from some adjacent pixels into one single signal. For the intensity method combining four pixels was enough, while for the lifetime method thirty two had to be combined. This explains then the coarser aspect of the pressure map by the lifetime method.

4. Conclusions & future work

The supersonic wind tunnel has been qualified and its performance, state of the boundary layer, and free-stream turbulence levels assessed. In this process and in the first test campaign it demonstrated the possibility of multiple Mach numbers in the range of unit Reynolds number $[3 \div 4.6] \cdot 10^7\ m^{-1}$. The boundary layer on the ramps constituting the lower and upper part of the nozzle divergent was found laminar, which indicates that noise will not radiate from them. Conversely, the free-stream mass-flow fluctuations were found high for the strict quiet-wind-tunnel standards, but in the same range as a normal, non-quiet one.

The good optical access onto the wind tunnel has made possible Pressure Sensitive Paint measurements, which gave noticeable results just limited by the hardware at disposal in case of the lifetime technique.

Future work will still focus on supersonic testing of the single roughness effects on a supersonic boundary layer but using different measurement techniques. Thin-films will be used for heat-flux measurements and piezoelectric-electric sensors (PCBs) for unsteady-pressure measurements. Both of these measurements will be performed at different wall temperatures and for roughness of different height.

Acknowledgments

The work here presented would have been much harder and longer without Mr. Peter Schreivogel taking care of the PSP experimental campaign, Mr. Glauco Bonfanti taking care of the development of the oil-dots experiments, Dr. T. Yasa setting up the hot-wire experiments, and, finally, Mr. Pierre Londers taking care of the wind-tunnel mounting and operations.

This work was performed within the Long-Term Advanced Propulsion Concepts and Technologies II project investigating high-speed transport, LAPCAT II, coordinated by ESA-ESTEC, and supported by the EU within the 7th Framework Program, Theme 7 TRANSPORT, Contract no.: ACP7-GA-2008-21 1485.

References

[1] S. V. Murthy, F. W. Steinle, On boundary layer transition in high subsonic and transonic flow under the influence of acoustic disturbances and free-stream turbulence, in: AIAA 85-0082, 1985.

[2] S. R. Pate, Effects of wind tunnel disturbances on boundary-layer transition with emphasis on radiated noise: A review, in: 11th Aerodynamic Testing Conference, Colorado Springs, Colorado/March 18-20, 1980.

[3] W. Harvey, Influence of free-stream disturbances on boundary-layer transition, Tech. rep., NASA (1978).

[4] G. Bonfanti, Development of oil-dot visualization technique for wall shear stress measurements, Research Master project 2011-07, von Karman Institute for Fluid Dynamics (2011).

[5] S. Schenider, Survey of boundary-layer transition for hypersonic applications, 2011.

[6] P. Schreivogel, G. Paniagua, H. Bottini, Pressure sensitive paint techniques for surface pressure measurements in supersonic flows, Experimental Thermal and Fluid Science in publication (in publication) in publication.

Modeling and Analysis of the Laminar to Turbulent Transition in a Low-pressure Turbine

Jayson Babajee

Turbomachinery and Propulsion Department, von Karman Institute for Fluid Dynamics, Belgium, jayson.babajee@vki.ac.be

Supervisor: Tony Arts

Professor, Head, Turbomachinery and Propulsion Department, von Karman Institute for Fluid Dynamics, Belgium, arts@vki.ac.be

University Supervisor: Francis Leboeuf

Professor, LMFA (Laboratoire de Mécanique des Fluides et d'Acoustique), France, Francis.Leboeuf@ec-lyon.fr

Abstract

The present study focuses on the assessment and the validation of the Langtry-Menter γ-$\widetilde{Re}_{\theta t}$ correlation-based transition model, recently implemented in the RANS code elsA from ONERA. The test cases are two Low-Pressure Turbine (LPT) rotor blades, with the same compressible Zweifel loading coefficient but different load distributions. The corresponding experimental results are provided by the von Karman Institute. The outlet isentropic Reynolds number, based on blade chord and outlet isentropic velocity, ranges from 60000 to 250000 in order to investigate the complex separation-induced transition phenomenon occurring at low Reynolds number cruise condition. The turbulence intensity is the natural freestream turbulence of the facility (0.9%). The numerical test campaign provides good predictions, particularly when accurately tailoring the trailing edge and wake regions of the mesh. The numerical mass-averaged kinetic losses are in good agreement with the experimental ones. Moreover, the flow topology parameters (the transition onset, the transition end and the separation) show good agreement in comparison to the experimental results and correlations from the open literature. One is even able to detect separation-induced transition with reattachment before the trailing edge at the lowest Reynolds number. However, the authors stress the turbulence Reynolds number effect on the prediction of separation-induced transition for strong diffusion LPT blades and particularly when the flow is subjected to a long bubble or even an open separation.

Keywords: Low-Pressure Turbine, Separation-Induced Transition, Reynolds number, Turbulence, Correlation

Nomenclature

Acronyms

AGS	Abu-Ghannam and Shaw transition criterion
HL	High-Lift
H&W	Hatman and Wang
LPT	Low-Pressure Turbine
RANS	Reynolds-Averaged Navier-Stokes
TD	Extrapolated "S1" decay of turbulence

Symbols

c	Chord
E	Destruction term of transport equation
g	Pitch
H	Shape factor
k	Turbulent kinetic energy
k_l	Laminar kinetic energy
l.e. / *LE*	Leading edge
M	Mach number
P	Production term of transport equation
P_0	Total Pressure
R	Radius
Re	Reynolds number
Re_t	Turbulence Reynolds number
Re_θ	Momentum thickness Reynolds number
$Re_{\theta c}$	Critical momentum thickness Reynolds number

$\widetilde{Re}_{\theta t}$	Local transition onset momentum thickness Reynolds number (transported variable)
Re_v	Vorticity Reynolds number
s	Curvilinear abscissa
s_0	Suction side TE curvilinear abscissa
t	Time
T	Period
$t.e.$ / TE	Trailing edge
Tu	Turbulence intensity [in %]
U / V	Velocity
x	Axial coordinate
y	Wall distance

Greek symbols

β	Flow angle (referred to axial direction)
γ	Intermittency
ζ	Mass-averaged kinetic losses [in %]
θ	Momentum thickness
λ_θ	Pressure gradient parameter
μ	Molecular viscosity
μ_t	Turbulent eddy viscosity
ρ	Density
σ_f	γ-transport equation diffusion coefficient
$\sigma_{\theta t}$	$\widetilde{Re}_{\theta t}$-transport equation diffusion coefficient
τ_{wall}	Wall shear stress
Ψ	Compressible Zweifel loading coefficient
ω	Specific turbulence dissipation rate
Ω	Rotational speed
ΔH	Total enthalpy variation across the rotor blade
ΔV_θ	Tangential velocity variation across the rotor blade

Subscripts

ax	Axial
eff	Effective
end	End of transition
is	Isentropic
$onset$	Onset of transition
sep	Separation
γ	Intermittency
θt	Momentum thickness at transition onset
1	Inlet condition
2	Outlet condition

1. Introduction

The main topic of this study is to analyze the laminar to turbulent transition mechanisms that occur in a LPT. For this purpose, one can evaluate the work done on the rotor in a pure axial machine with the turning of the flow from the Euler's momentum equation:

$$\Delta H = \Omega \cdot R \cdot \Delta V_\theta \tag{1}$$

A standard LPT is usually made of several stages (4 stages in the case of the CFM56-7B). LPTs commonly operate at an outlet Mach number in the range from 0.6 to 0.9 and weight 20% to 30% of the overall mass of the engine [1]. Thus, the aim is not to manufacture more powerful and heavier aero-engines such as an industrial gas turbine but to get the most efficient one in terms of power with respect to weight and losses mainly. At a first sight, one solution is inevitably to reduce the weight of the LPT by reducing the number of blades. This implies an increase of the pitch-to-chord ratio (g/c). This entails a more important loading per blade in order to compensate for the lower number of working blades for a given stage loading. As a consequence, the velocity suction peak will be higher as well as the diffusion over the rear part of the suction side. Nevertheless, one has to be aware, for this study, of the separation and transition phenomena. This conveys the importance of the Reynolds number (Re) since the current LPT operating Reynolds number is below 100000 at cruise conditions and more than 400000 at take-off. This shows the wide operating conditions of a LPT and above all the changing flow conditions as highlighted by Hourmouziadis [2]. This is why the study of the transition mechanisms is of interest because in the case of open separation, the flow topology is not as the one predicted by standard ideal model.

Therefore, the main aim of this work will be to assess the γ-$\widetilde{Re}_{\theta t}$ transition model of Langtry and Menter [3] on two HL-LPT rotor blades (where "HL" stands for "High-Lift" and is mainly characterized by the tendency to decrease the number of blades per row and consequently to increase the loading per blade).

2. Transition and Separation Phenomena in LPT

Transition occurs due to the amplification of instabilities in the boundary layer. The main factors to consider are the Reynolds number, the turbulence intensity, the turbulence scales and the pressure gradient.

2.1. Steady Transition

Even though a LPT environment is rather unsteady, one still needs to define the fundamental physics behind steady transition since most of cascade investigations in wind tunnels are carried out under steady conditions. There are four kinds of transition (the natural transition, the by-pass transition, the separation-induced transition and the reverse transition (relaminarization)).

In LPT cases, the last three cases are of interest since natural transition only occurs at very low turbulence levels (below 0.1%). In the by-pass transition, transition occurs due to disturbances that lead directly to the formation of turbulent spots by by-passing the growth of Tollmien-Schlichting waves. Basically, those disturbances are characterized by a high turbulence level. In the separation-induced transition, the flow is subjected to a separation bubble which is mainly caused by an adverse pressure gradient and depends on the Reynolds number as well. Then, at low Reynolds numbers and with a strong diffusion (which is the case of HL-LPT), the laminar boundary layer separates and the transition process occurs in the free shear layer. However, depending on the Reynolds number and on the turbulence intensity and scales, the reattachment process may not happen, leading to an open separation which is the worst case in terms of losses. There are three separated flow modes according to the work of Hatman and Wang [4]. Those are the transitional separation mode, the laminar separation/short bubble mode and the laminar separation/long bubble mode. At last, the reverse transition is typically a way back from a turbulent flow to a laminar one which occurs in region of very strong acceleration such as the rear part of the blade pressure side.

2.2. Multimode Transition

This type of transition is an unsteady phenomenon. It is a realistic illustration of the turbomachinery environment where the wakes from a blade row impinge on the following blade row while triggering the transition or inhibiting separation. Actually, the growth of turbulent spots, after the impingement of a wake on the suction side of a blade, implies the occurrence of calmed regions which are less sensible to disturbances. They present the advantages of the laminar and turbulent regions without their respective drawbacks [5]. The effectiveness of these calmed regions was illustrated in [6; 7]. This region follows the turbulent region at a lower velocity as shown in the work of Schubauer and Klebanoff [8]. They highlighted that the flow starts to be very stable and no breakdown seems to occur from the spot tail. Moreover, the interest of this calmed region is seen in the distance-time diagram (Fig. 1). The difference between the leading and trailing edge velocities of this region insures the development of a laminar look-alike region.

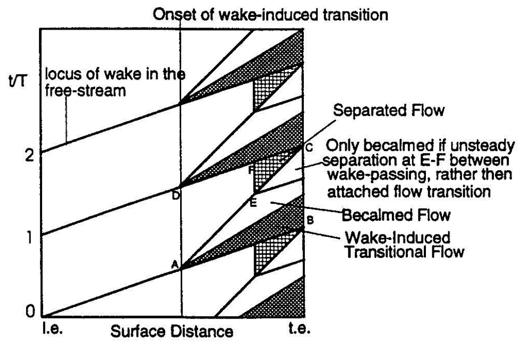

Figure 1: Time-space diagram of the turbulent spots (Schulte and Hodson [9])

2.3. Parameters Affecting Transition and Separation

At this point of the review, the most important factors affecting transition are the Reynolds number, the turbulence scales, the pressure gradient and the unsteady features of the incoming wakes. However, Mayle [10] depicted the existence of other factors which are less significant in terms of turbulent spot production rate than the pressure gradient such as the surface roughness. Moreover, other designs [11; 12; 13; 14] might be of interest such as transversal roughness elements, jets and plasma actuators.

3. Numerical Approach

To understand the phenomenon of separated-flow transition, one should get a large database in order to assess the findings on each configuration in the aim of making a universal model. However, it could demand a lot of effort since each configuration may be one of a kind and consequently will not infer the principle of universality. That is why data-driven correlations are still useful in predictive models based on trends. The cornerstone of those correlations is the momentum thickness Reynolds number (Re_θ). It is based on the momentum thickness (θ) which quantifies the portion of momentum flux loss due to the presence of the wall. It means that the momentum thickness will behave differently according to the nature of the flow in the boundary layer. That might be an explanation for the perpetual use of this parameter in the correlations. However, one drawback is its complicated assessment in a cascade configuration. Then, one sees the interest of the numerical approach to get more information about this critical parameter.

3.1. Transition Modeling

Most of the transition criteria are based upon empirical correlations [10; 15]. Those criteria are made non-local as they take into account the history of the boundary layer with the freestream information (turbulence intensity and pressure gradient). When the transition criterion is met, the so-called "intermittency weighting function" is switched on from 0 to 1 (like a step) and consequently triggers the production of the turbulent kinetic energy. However, despite its numerical definition, it still keeps the same qualitative meaning of the intermittency coefficient which is the fraction of time during transition for which the flow is turbulent. Besides, this kind of methodology implies the need for the boundary layer thickness calculation from the integration of the velocity profiles. Instead of triggering transition by a switch (via the intermittency weighting function), the transition process should be handled locally with a gradually evolving intermittency weighting function. That is why new methods for the computation of transition founded on transport equations (using local quantities) are of interest such as the γ-$\widetilde{Re}_{\theta t}$ model of Langtry and Menter [3]. Another transport equation transition model based on the laminar kinetic energy approach [16; 17] seems promising.

3.1.1. Correlation-Based Transport Equation Model

The γ-$\widetilde{Re}_{\theta t}$ model central idea is the van Driest and Blumer's vorticity Reynolds number concept [18]. It allows to link the transition onset momentum thickness Reynolds number to the local boundary layer quantities. The concept is depicted in Eqns. 2 and 3.

$$Re_v = \frac{\rho \cdot y^2}{\mu} \cdot \left|\frac{\partial u}{\partial y}\right| = \frac{\rho \cdot y^2}{\mu} \cdot S \tag{2}$$

$$Re_\theta = \frac{\max\left(Re_v\right)}{2.193} \tag{3}$$

In fact, this model gets rid of the integration of the boundary layer velocity profile along "computation lines" based on the wall mesh lines. Those velocity profiles were used to determine the onset of transition according to non-local transition criteria (such as the Abu-Ghannam and Shaw correlation [15]) in the sense that they are based on the turbulence intensity and the pressure gradient parameter estimated at the edge of the boundary layer.

The transport equation for the numerical intermittency (γ) is:

$$\begin{aligned}\frac{\partial(\rho\gamma)}{\partial t} + \frac{\partial\left(\rho U_j \gamma\right)}{\partial x_j} &= \\ P_\gamma - E_\gamma &+ \frac{\partial}{\partial x_j}\left[\left(\mu + \frac{\mu_t}{\sigma_f}\right)\frac{\partial \gamma}{\partial x_j}\right]\end{aligned} \tag{4}$$

In their first publication, Menter et al. [19] did not disclose all their functions and particularly the F_{length} and the $Re_{\theta c}$ functions. At this time, it was known they were function of the transition onset momentum thickness Reynolds number ($\widetilde{Re}_{\theta t}$). That is why several groups throughout the world focused on the determination of these functions [20; 21; 22; 23]. At last, the originators of this transition model published their own version of these missing functions [3]. However, in this study, the CFD code elsA relies on the calibrations of those functions performed by Content and Houdeville [23].

The transport equation for the transition onset momentum thickness Reynolds number ($\widetilde{Re}_{\theta t}$) is:

$$\begin{aligned}\frac{\partial\left(\rho \widetilde{Re}_{\theta t}\right)}{\partial t} + \frac{\partial\left(\rho U_j \widetilde{Re}_{\theta t}\right)}{\partial x_j} &= \\ P_{\theta t} &+ \frac{\partial}{\partial x_j}\left[\sigma_{\theta t}\left(\mu + \mu_t\right)\frac{\partial \widetilde{Re}_{\theta t}}{\partial x_j}\right]\end{aligned} \tag{5}$$

The purpose of this equation is to transform the non-local empirical correlation into a local quantity in order to compute the transition length function (F_{length}) and the critical momentum thickness Reynolds number ($Re_{\theta c}$), necessary for the numerical intermittency equation (Eqn. 4).

Then, when Re_θ (cf. Eqn. 3) exceeds locally $Re_{\theta c}$ (which is a function of $\widetilde{Re}_{\theta t}$), γ equals one due to the activation of P_γ in Eqn. 4. After, a function defines the effective intermittency γ_{eff} by the maximum value between γ and γ_{sep}. This latter separation intermittency coefficient (γ_{sep}) is part of a separation-induced transition correction that allows the local intermittency to exceed one. At last, γ_{eff} imposes the laminar regions locally and triggers the transition mechanism by turning on the production term of the turbulent kinetic energy transport equation because this transition model is coupled to the SST k-ω turbulence model. Besides, γ_{eff} affects the destruction term of the turbulent kinetic energy transport equation. The mentioned separation-induced transition correction is to let k to grow more rapidly once the boundary layer separates. This is the reason why it exceeds one.

3.1.2. Phenomenological Transport Equation Model

This laminar kinetic energy (k_l) model is based on the laminar fluctuation energy in the pre-transition region of the boundary layer as first introduced by Mayle and Schulz [24]. Their starting point was the fact that the laminar fluctuations preceding transition are primarily caused by the work of the imposed fluctuating free-stream pressure forces on the flow in the boundary layer. This framework has led several research groups to focus on this concept [16; 17]. Lardeau et al. [17] highlighted that the pre-transitional fluctuations leading to bypass transition are due to the presence of low-frequency/low amplitude streamwise vortices in the boundary layer. It turned out that the kinetic energy of the laminar fluctuations (k_l) can be described by a transport equation similar to the transport equation for the turbulent kinetic energy (k). The objective is to model the pre-transitional fluctuations with the k_l equation. Once a parameter including the kinetic energy is greater than some threshold level, the energy from the streamwise fluctuations k_l is transferred to the turbulent fluctuations [25]. Besides, the transition process is defined by a transfer of energy from k_l to k via the pressure-strain mechanism [16]. It is called "energy redistribution".

4. Results

In this section, the investigations of two HL-LPT rotor blades (T108 and T106C) are presented in terms of numerical methodology, comparison with experimental results and assessment of the γ-$\widetilde{Re}_{\theta t}$ model. A linear cascade configuration as well as the high speed, low Reynolds number VKI S1 wind tunnel facility are documented in Michálek et al. [26]. The main characteristics of the blades are provided in Tab. 1.

Table 1: Blades Characteristics

Blade	T108	T106C
c (mm)	98.42	93.01
c_{ax} (mm)	81.23	79.97
Pitch-to-chord ratio, g/c	0.90	0.95
β_1 (deg)	33.2	33.2
$\Psi=2\cdot\frac{g}{c_{ax}}\cdot\frac{\lvert\rho V_\theta V_x\rvert_2-\lvert\rho V_\theta V_x\rvert_1}{\rho_2 V_2^2}$	1.22	1.24
Configuration	Front-loaded	Aft-loaded
Diffusion Rate, D_R $D_R=\frac{\frac{V_{peak}-V_{2,is}}{V_{2,is}}}{\left\lvert\frac{s_{peak}-s_0}{s_0}\right\rvert}$	0.41	0.58
Velocity Ratio, $\frac{V_{peak}}{V_{2,is}}$	1.31	1.30
$M_{2,is}$	{0.5 ; 0.6}	0.65
$Re_{2,is}$ ($\times 10^3$)	[60 ; 160]	[80 ; 250]
$Tu_{l.e.}$(%)	0.9	0.9
$Re_t=\frac{\rho k}{\mu\omega}$	[4.8 ; 12.7]	[6.7 ; 22.2]

4.1. Computational Methodology

In this paper, three-dimensional CFD simulations are carried out with the in-house ONERA code elsA (ensemble logiciel de simulation en Aérodynamique). The elsA software package is based on a cell-centered finite volume method for solving the Navier-Stokes equations. The space discretization relies on multi-block structured meshes. It allows the simulation of steady or unsteady flows, inviscid or viscous fluids, in fixed or moving frames. However, in this study, only RANS simulations with the Menter k-ω SST turbulence model are considered, coupled with the γ-$\widetilde{Re}_{\theta t}$ transition model. The use of the particular single-step case of the Runge-Kutta method for time integration, known as the "Backward Euler" time integration scheme is used. This scheme is coupled with a LU implicit phase technique. The space discretization scheme is a second order Roe scheme. The mesh topology is a periodic standard O4H with High Staggered corrections since the geometries are defined by high values of deviation (Fig. 2). The central O-mesh is around the blade and has at least 41 points in the perpendicular direction away from the blade surface. In the streamwise direction around the blade, the number of nodes is above 225 in order to get a good discretization of the suction side of the blade. The extension of the mesh in the spanwise direction is restricted to 5 layers and consequently symmetry

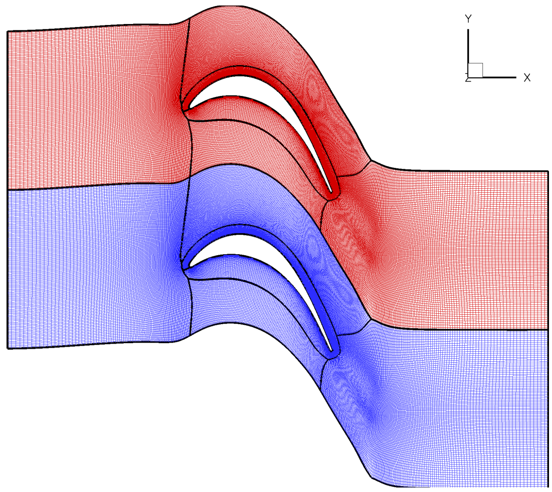

Figure 2: Mesh topology of T106C (Ψ = 1.24)

boundary conditions are used to define the pseudo-hub and -shroud. This saves a lot of computation time by focusing on the middle of the blade in order to apply convergence acceleration methodologies. As the study focuses on LPT blades which have high aspect-ratios, it is possible to avoid the calculation of the endwall regions. This is to mimic the experimental configuration where the measurements were taken at midspan. This methodology is referred as "2.5D". Thus, the aforementioned steady RANS "2.5D" γ-$\widetilde{Re}_{\theta t}$ model methodology is meant to be a prediction tool which could be used with an industrial prospect for blade design.

Before starting these test campaigns, a study of the mesh (not presented here for a lack of space) was carried out in order to assess the influence of the wake treatment. It turned out that the wake prediction could be too wide and not deep enough with respect to the experimental wakes (and consequently the mass-averaged kinetic losses). In fact, the cells downstream of the trailing edge of the blade should follow the flow direction. From this mesh strategy, the number of nodes for both configurations is 46605 in one streamwise layer. Moreover, y^+ values are below 1 through the Reynolds number ranges.

Concerning the computational inlet conditions for distant boundaries, one needs to provide turbulence and transition variables. About the transition ones, γ is set to 1.0 and $\widetilde{Re}_{\theta t}$ is determined by a correlation [3]. The turbulence variables (turbulent kinetic energy k and specific turbulence dissipation rate ω), at those inlet conditions, are incompletely known according to Spalart and Rumsey [27]. However, the decay of turbulence, ahead of the cascade, is available from the test campaign carried out at the von Karman Institute [26] where it was assessed behind a turbulence grid in the S1 facility. This "S1" decay law was compared to a decay law from Chassaing [28]. He described two phases of the decay of turbulence. The initial phase is defined as the prevalence of the eddies in the decay of turbulence (in the region downstream the turbulence grid). The final phase is defined as the prevalence of the dissipation in the decay of turbulence (far downstream the turbulence grid). In Fig. 3, one can see the good agreement between the two sets of decay of turbulence (the "S1" one and the initial phase one from Chassaing [28]). Then, since the turbulence intensity measured without any grid of turbulence (0.9%) is in between the initial and final phases but closer to the initial phase, an extrapolation of the "S1" decay law was done in order to get the input values (and particularly the dissipation rate) for the inlet boundary conditions. Thus, from this extrapolated "S1" decay law,

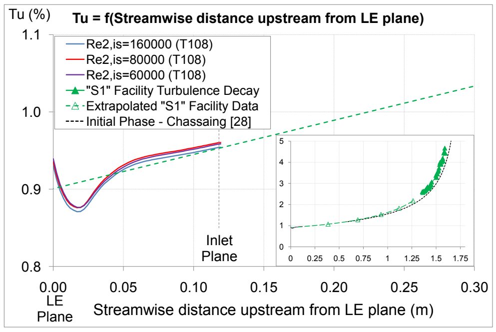

Figure 3: "S1" Decay of turbulence ahead of the cascade

it is possible to set the inlet boundary conditions according to the desired values at the leading edge plane. When assessing the CFD predictions of the turbulence evolution ahead of the cascade at several outlet isentropic Reynolds number ($Re_{2,is}$), one can see that the inlet boundary condition inputs enable the CFD predictions to match the experimental trends (Fig. 3). Then, this methodology for imposing the dissipation rate at the inlet boundary condition is adopted for this study. To give an order of magnitude, the Kolmogorov length scale for the T106C blade at $Re_{2,is}$ = 120000, $M_{2,is}$ = 0.65 and $Tu_{l.e.}$ = 0.9% is 4.10^{-4} m for the CFD calculation whereas Michalek et al. [2010], who carried out the experimental investigation of this configuration, had 5.10^{-4} m.

Finally, a comparison between the well-used non-local transition criterion of Abu-Ghannam and Shaw (AGS) [15] and the newly implemented transition transport equation model γ-$\widetilde{Re}_{\theta t}$ [3] was carried out in order to show the superiority of this transport equation model since both approaches are correlation-based but differ from the way the information is treated (non-locally or locally). Figure 4 shows this superiority with the isentropic Mach number (M_{is}) distribution along the suction side of the T108 blade. Besides, it has to be reminded that the correlation of Abu-Ghannam and Shaw [15], which is part of the framework behind the correlation used in Langtry and Menter transition model [3], is based upon experimental data which pressure gradient parameter (λ_θ) is between ± 0.1. In the current study, the two HL-LPT rotor blades have a λ_θ that can be lower than -0.1.

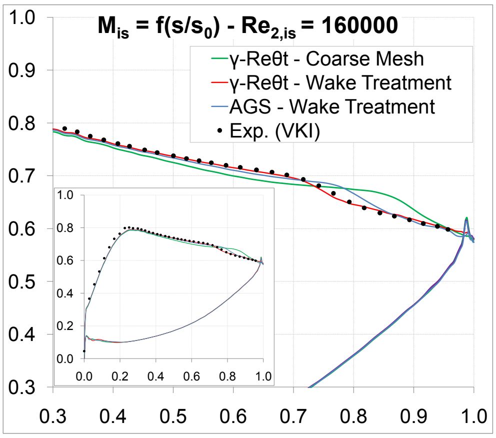

Figure 4: T108 comparison of γ-$\widetilde{Re}_{\theta t}$ model and AGS criterion at $Re_{2,is}$ = 160000, $M_{2,is}$ = 0.6 and Tu_1 = 0.9% (abscissa: s/s_0, ordinate: M_{is})

4.2. T108 Cascade

After setting up the methodologies of the study, one can focus on the T108 blade and the comparison with other research groups using different transition models and/or different methodologies. Corral and Gisbert [29] worked on this geometry with the γ-$\widetilde{Re}_{\theta t}$ model coupled with the RANS solver Mu^2s^2T. Their model features a $\widetilde{Re}_{\theta t}$-transport equation diffusion coefficient ($\sigma_{\theta t}$) equals to 10 and a s_1 function (which controls the reattachment location [30]) depending upon $\widetilde{Re}_{\theta t}$ and the distance to the wall. They performed 2D computations with a very fine unstructured mesh of 70000 points. Pacciani et al. [31] used the laminar kinetic energy concept coupled with the Wilcox k-ω turbulence model. They performed 2D computations with a non-periodic single-block O-type mesh of 57521 nodes. Benyahia et al. [32] used the RANS code elsA developed by ONERA. They worked on the implementation of the γ-$\widetilde{Re}_{\theta t}$ transition model and used it coupled with the Menter k-ω SST turbulence model. They performed 3D computations with a O4H structured mesh of 14545 points in one spanwise layer. The difference between Benyahia et al. [32] γ-$\widetilde{Re}_{\theta t}$ model and the one used in the present work is the value of the diffusion coefficient ($\sigma_{\theta t}$=10 in Benyahia et al. [32] and $\sigma_{\theta t}$=2 in the present work, value recommended by Langtry and Menter [3]). At last, the VKI experimental results [33] are provided.

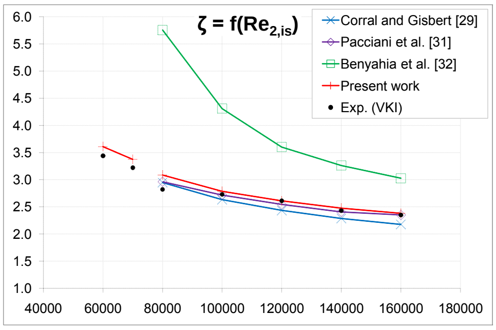

Figure 5: T108 mass-averaged kinetic losses (abscissa: $Re_{2,is}$, ordinate: ζ)

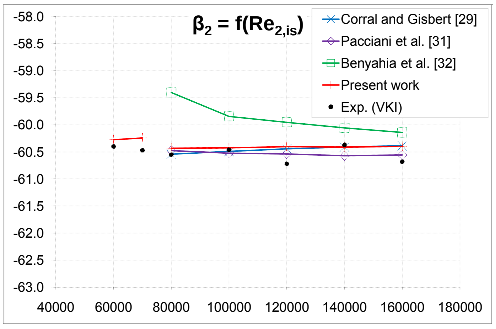

Figure 6: T108 mass-averaged outlet flow angle (abscissa: $Re_{2,is}$, ordinate: β_2)

The comparisons, in terms of mass-averaged kinetic losses (ζ) and outlet flow angle (β_2), are depicted in Figs. 5 and 6. From these figures, one can see that the present study predictions are in good agreement with the experimental measurements over the full $Re_{2,is}$ range. As a remark, the break in the $Re_{2,is}$ range is intentional since the two lowest $Re_{2,is}$ were performed in the facility at a lower outlet isentropic Mach number ($M_{2,is}$=0.5 instead of 0.6). From those trends, the similarity between the correlation-based transition model (Corral and Gisbert [29] and the present study) is remarkable even though the calibration parameters are not the same (such as $\sigma_{\theta t}$ and s_1). This could be a reason why an offset in the trends is noticeable. However, this might be due to the different values of the turbulence Reynolds number ($Re_t = \mu_t/\mu = (\rho k)/(\mu\omega)$) used between the two groups to compute the dissipation rate at the inlet boundary condition. The quality of the mesh in both studies does not seem to imply any mesh dependency. This last point leads to the comparison between the present study predictions with the ones of Benyahia et al. [32]. Their predictions overestimate the experimental results, even though they got good predictions of the M_{is} distribution over the blade suction side. The reason is a question of mesh dependency since they used the coarsest mesh among all the presented studies and there is no apparent wake treatment or refinement in the wake vicinity. At last, the comparison with Pacciani et al. [31] predictions leads to a good matching. Since their laminar kinetic energy approach is intented to be based on more physical models, one can conclude on the reliability of the correlation-based transition model, used in this study, for this HL-LPT blade configuration. Moreover, the M_{is} distribution

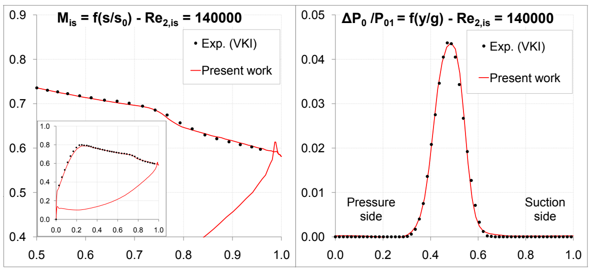

Figure 7: T108 isentropic Mach number distribution and wake profile at $Re_{2,is}$ = 140000 (left abscissa: s/s_0, left ordinate: M_{is}, right abscissa: y/g, right ordinate: $\Delta P_0/P_{01}$)

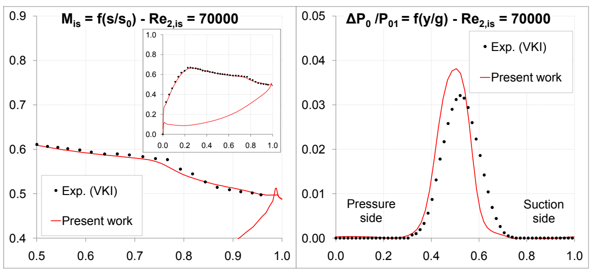

Figure 8: T108 isentropic Mach number distribution and wake profile at $Re_{2,is}$ = 70000 (left abscissa: s/s_0, left ordinate: M_{is}, right abscissa: y/g, right ordinate: $\Delta P_{01}/P_{01}$)

over the suction side of the blade as well as the wake profile, extracted at $0.5 \cdot c_{ax}$ downstream the trailing edge, of two $Re_{2,is}$ (140000 and 70000) are provided (Figs. 7 and 8). From these plots, one can assess the fairly good wake predictions in terms of width and depth. The M_{is} distributions are pretty good as well in terms of pressure plateau, reattachment and Mach number level.

4.3. T106C Cascade

After the results of a front-loaded blade (T108) with a mild diffusion rate (Tab. 1), the study of an aft-loaded blade (T106C) with a strong diffusion is presented below. Like the former section, the same research groups worked on the T106C blade with the same methodology and numerical approach, except Benyahia et al [32] who used for the T106C a finer mesh with a wake treatment. Once again, the comparisons in terms of ζ and β_2 are illustrated (Figs. 9 and 10). This time, the ζ are well predicted up to

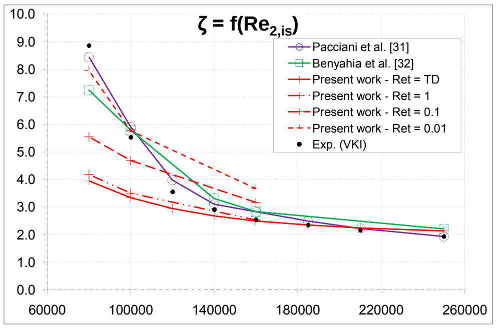

Figure 9: T106C mass-averaged kinetic losses (abscissa: $Re_{2,is}$, ordinate: ζ)

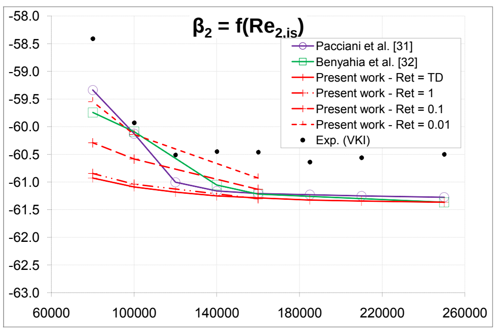

Figure 10: T106C mass-averaged outlet flow angle (abscissa: $Re_{2,is}$, ordinate: β_2)

$Re_{2,is}$ = 140000. For lower values, one can observe the underprediction of the "TD" trend which corresponds to the value extracted from the extrapolated "S1" decay law. Apparently, the values of Re_t used by the other research groups are lower than the one used in the 'TD' trend (Tab. 1). In fact, Pacciani et al. [31] used a ratio of turbulence length scale over the axial chord of 2.5×10^{-3} which represents a value of Re_t of approximately 0.93. Benyahia et al. [32] used a value of 0.1. Since the predictions seem to be Re_t-dependent, a study of this Re_t was carried out. From Figs. 9 and 10, one can see the improvements of the predictions (particularly at low $Re_{2,is}$) by lowering Re_t (up to 0.01). Concerning the other research groups, they are able to catch the bursting of the bubble (i.e. when the topology of the bubble changes from a short one to a long one and when the pressure distribution is clearly affected [34]) and even an open separation.

Let's have an insight at the level of turbulence across the cascade in the "freestream" region (between two blades) for $Re_{2,is} = 80000$. From Fig. 11, one can see that for $Re_t = 0.01$, the level of turbulence is really low (around 0.1%). This behavior is close to a pseudo-laminar case or an external flow configuration. Moreover, it does not follow the extrapolated "S1" decay law. This conclusion is applicable to $Re_t = 0.1$ as well whereas $Re_t = 1$ seems close to the extrapolated "S1" decay law. In fact, when checking the M_{is} distribution, one can notice the proximity of the $Re_t = 1$- and $Re_t = TD$-cases (Fig. 12). In addition, from the experimental data, one would expect an open separation. This is predicted by the two lowest Re_t (0.1 and 0.01) where the M_{is} distributions are affected by this open separation phenomenon as illustrated by a lower peak Mach number as well as a more upstream position of it [34]. Morever, it is followed by a longer pressure plateau. In addition, the wake profile (Fig. 12), extracted at $0.5 \cdot c_{ax}$ downstream the trailing edge, illustrates the correct prediction done by the lowest Re_t. The wake profile is wider and deeper (which confirms the influence of the open separation on the size of the boundary layer and consequently the velocity deficit). The investigation of a higher inlet turbulence level (1.7%) illustrates the preponderance of the dissipation at low Re_t on the turbulent kinetic energy level (Fig. 11).

4.4. Validation of the γ-$\widetilde{Re}_{\theta t}$ Transition Model Implemented in elsA: Assessment of the Flow Topology Parameters

In this last section, a focus on the flow topology parameters is illustrated. These parameters are the transition onset, the transition end and the separation locations. One can extract them from both the numerical and experimental data. However, Re_θ is only accessible via the numerical predictions. Then, one can compare those information with correlations of the open literature.

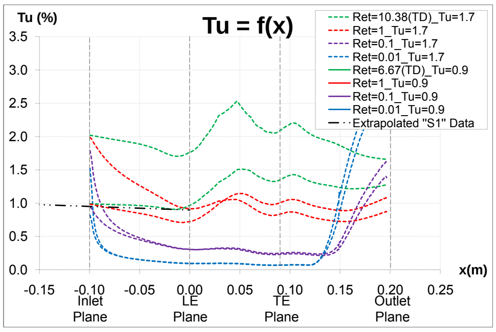

Figure 11: Turbulence across T106C cascade at $Re_{2,is} = 80000$ with the influence of the Re_t

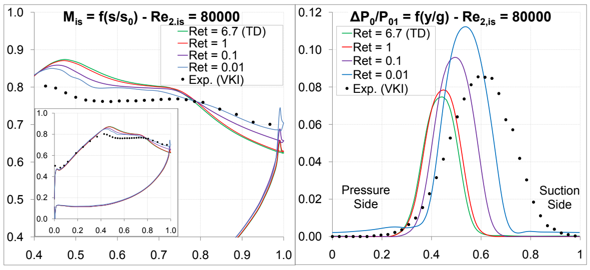

Figure 12: T106C isentropic Mach number distribution and wake profile with Re_t effect at $Re_{2,is} = 80000$ (left abscissa: s/s_0, left ordinate: M_{is}, right abscissa: y/g, right ordinate: $\Delta P_{01}/P_{01}$)

To get those flow topology parameters, one can rely on the effective intermittency (γ_{eff}), the turbulent/laminar viscosity ratio (μ_t/μ), the shape factor (H) and the wall shear stress (τ_{wall}). γ_{eff} is the output of the correlation behind the transition model. While scanning the boundary layer from the wall to the edge, one can use this parameter when it suddenly increases to 1 and then decreases. The sudden increase might be defined as the transition onset. This position is considered as the moment where the intermittency first starts to grow [30]. Besides, there is a correlation between $Re_{\theta c}$ and $\widetilde{Re}_{\theta t}$ which defines the lag between the first rise of intermittency and the moment where the skin friction starts to increase [30]. For μ_t/μ, one can assess the transition onset when it exceeds 1. This criterion is defined by the ratio of the eddy viscosity and the molecular viscosity. Thus, when this ratio exceeds 1, it means the turbulence patterns are preponderant. For H, one can assess the transition onset when it is maximum before any sudden decrease. Indeed, it is well-known that the shape factor of a laminar incompressible boundary layer ($H \approx 2.6$) is higher than a turbulent one ($H \approx 1.3$) in a flat plate configuration. Moreover, the shape factor is influenced by the adverse pressure gradient in those HL-LPT configurations. Thus, it allows to assess the position of a possible separation point when H exceeds 3.5. For τ_{wall}, one will notice a sudden increase of it close to its minimum value. When τ_{wall} starts to stabilize at a constant value and even to decrease in order to follow the trend of the fully turbulent case, then this position is defined as the transition end. When τ_{wall} is negative, this indicates a separation. When τ_{wall} exceeds zero after being negative, one can define a reattachment. About the experimental information, one can assess the flow topology parameters with the combination of the M_{is} distribution over the blade [5] and the pseudo-wall shear stress [26].

From Fig. 13, one can see the evolution of the transition onset location with $Re_{2,is}$. For the T108 case, the movement of the transition onset towards the trailing edge as $Re_{2,is}$ decreases is well captured by the flow topology parameters, except γ_{eff} which predicts earlier transition onsets. In fact, this was expected since γ_{eff} defines the moment when $Re_{\theta c}$ is reached and where γ first starts to grow [30]. One can draw the same conclusion about the T106C blade except that at low $Re_{2,is}$, the flow is prone to long bubble and open separation bubble topologies which affect the positions of separation and transition onset significantly [5]. From both the T106C experimental data and numerical predictions, the trend of the transition onset to travel downstream as $Re_{2,is}$ decreases is respected. However, when decreasing more $Re_{2,is}$, the Re_t effect is clearly visible. Thus, the expected upstream movement of the transition onset is not predicted in the extrapolated "S1" decay law Re_t-case whereas it is predicted when Re_t is extremely low (0.01, depicted by the plain symbols in Fig. 13). Concerning the separation point (Fig. 15), its upstream movement as $Re_{2,is}$ decreases is respected from both the experimental and numerical data. Once again, the Re_t effect is noticeable in the T106C case. About the transition end position (Fig. 14), its downstream movement as $Re_{2,is}$ decreases is predicted by the numerical approach while it seems pretty constant for the experimental predictions through the $Re_{2,is}$ range. The reason, which is also applicable to the experimental transition onsets, is the low spatial resolution of the pseudo-wall shear stress measurements. There are 15 hot-film gauges, spread over the suction side. They are regularly spaced in the deceleration part (~5 mm in the curvilinear axis). At last, Fig. 16 illustrates the relationship between the momentum thickness Reynolds number at separation ($Re_{\theta,sep}$) and $Re_{2,is}$ for both blades. In addition to the numerical predictions, the criteria proposed by Hatman and Wang [4] are depicted. As expected, the higher $Re_{2,is}$ are situated in the "Laminar Separation - Short Bubble" region of the plot. Then, the bursting $Re_{2,is}$ for the T108 blade is considered to be around 115000 (even though no clear bursting is visible from ζ and β_2 experimental trends in Figs. 5 and 6). Likewise, the T106C bursting $Re_{2,is}$ is assessed with Fig. 16 and is considered to be around 160000, which is overestimated according to ζ as well as β_2 experimental trends (Figs. 9 and 10).

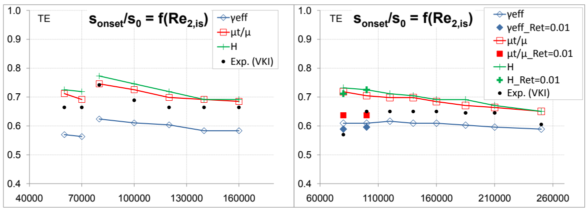

Figure 13: Transition onset through the $Re_{2,is}$ range for T108 (left) and T106C (right) (abscissa: $Re_{2,is}$, ordinate: s_{onset}/s_0)

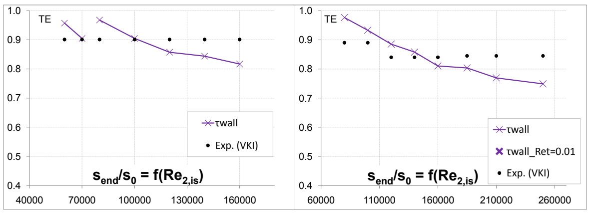

Figure 14: Transition end through the $Re_{2,is}$ range for T108 (left) and T106C (right) (abscissa: $Re_{2,is}$, ordinate: s_{end}/s_0)

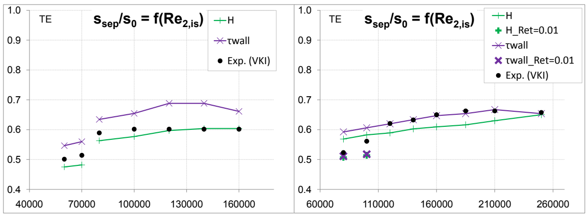

Figure 15: Separation through the $Re_{2,is}$ range for T108 (left) and T106C (right) (abscissa: $Re_{2,is}$, ordinate: s_{sep}/s_0)

5. Conclusions

A new and promising transport equation transition model [3], recently implemented in elsA [23] (one equation for γ and other one for $\widetilde{Re_{\theta t}}$), was assessed on two HL-LPT rotor blades (T108 and T106C). Since those blades are prone to separation-induced transition, they form a good sample group for the model validation as a prediction tool.

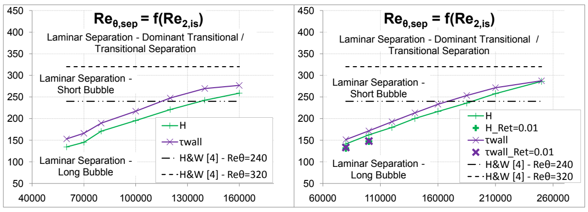

Figure 16: $Re_{\theta,sep}$ through the $Re_{2,is}$ range for T108 (left) and T106C (right) (abscissa: $Re_{2,is}$, ordinate: $Re_{\theta,sep}$)

In the present work, the authors focused on the importance of the turbulent variables boundary conditions which are commonly defined by Re_t. It was concluded, from the experimental decay law, that one can predict the state of the boundary layer, and consequently ζ for mild diffusion HL-LPT rotor blades (T108). For more harsh diffusion HL-LPT rotor blades (T106C), the boundary layer state predictions are satisfactory for mid-$Re_{2,is}$ but are underestimated in the low-$Re_{2,is}$ range where long bubble and open separation topologies are encountered. In fact, an investigation of Re_t has illustrated the influence of this parameter on the boundary layer state predictions. Thus, by lowering more and more this parameter, and as a consequence increasing the dissipation rate, it was possible to predict the expected flow topologies. However, this high dissipation rate does not fulfill the requirements of the experimental decay of turbulence as the flow in the cascade is defined by really low levels of turbulence (~0.1%). Therefore, this low-Re_t approach lacks predictive behavior as a tuning seems necessary. Nevertheless, an investigation of the diffusion of the turbulent variables into the boundary layer might be of interest in order to understand how it affects the position of separation. Indeed, it seems this position impacts the onset of transition according to the Re_t-investigation (the upstream movement of separation point induces an upstream movement of the transition onset at low $Re_{2,is}$ whereas it induces a downstream movement at mid $Re_{2,is}$). Besides, one has to remember the correlation for the onset of transition in the adverse pressure gradient region is basically meant for attached flows [15; 19] and ranges up to $\lambda_\theta = \pm 0.1$ (λ_θ can be lower than -0.1 for the HL-LPT blade cases of the present work).

Concerning those flow topology parameters, their assessment reveals to be in good agreement with the experimental results.

At last, this steady RANS approach using this new transition model exhibits its robustness in predicting separation-induced transition for mild diffusion HL-LPT rotor blades but needs to be carefully used if strong diffusion HL-LPT configurations are intended for investigation. In fact, more work on the calibration process is expected in order to extend the applicability of this promising model on strong diffusion HL-LPT blades.

6. Acknowledgments

The experimental results reported in this work were obtained within the European research project TATMo "Turbulence and Transition Modelling for Special Turbomachinery Applications" (AST5-CT-2006-030939).

The authors would like to thank SNECMA for the permission to publish this paper. They are also grateful to Jan Michálek (VKI) and Abdelkader Benyahia (ONERA) for the constructive discussions.

References

[1] H. P. Hodson, R. J. Howell, The Role of Transition in High Lift Low Pressure Turbines, von Karman Institute for Fluid Dynamics Lecture Series 2005-03.

[2] J. Hourmouziadis, Aerodynamic Design of Low Pressure Turbines, AGARD Lecture Series 167.

[3] R. B. Langtry, F. R. Menter, Correlation-Based Transition Modeling for Unstructured Parallelized Computational Fluid Dynamics Codes, AIAA Journal 47 (12) (2009) 2894–2906.

[4] A. Hatman, T. Wang, A Prediction Model for Separated-Flow Transition, ASME Journal of Turbomachinery 121 (3) (1999) 594–602.

[5] T. Coton, Unsteady Wake-Boundary Layer Interaction on Advanced High Lift Low Pressure Turbine Airfoils, Ph.D. thesis, Université Libre de Liège (December 2003).

[6] H. Pfeil, R. Herbst, Transition Procedure of Instationary Boundary Layers, in: ASME Gas Turbine Conference and Exhibit and Solar Energy Conference, no. 79-GT-128, San Diego, California, USA, 1979.

[7] H. Pfeil, R. Herbst, T. Schröder, Investigation of the Laminar-Turbulent Transition of Boundary Layers Disturbed by Wakes, ASME Journal of Engineering for Power 105 (1) (1983) 130–137.

[8] G. B. Schubauer, P. S. Klebanoff, Contributions on the Mechanics of Boundary-Layer Transition, Technical Note 3489, National Advisory Commitee for Aeronautics (September 1955).

[9] V. Schulte, H. P. Hodson, Prediction of the Becalmed Region for LP Turbine Profile Design, ASME Journal of Turbomachinery 120 (4) (1998) 839–846.

[10] R. E. Mayle, The Role of Laminar-Turbulent Transition in Gas Turbine Engines, ASME Journal of Turbomachinery 113 (4) (1991) 509–537.

[11] C. G. Himmel, H. P. Hodson, Modifying Ultra-High Lift Low Pressure Turbine Blades for Low Reynolds Number Applications, in: 12th International Symposium on Unsteady Aerodynamics, Aeroacoustics & Aeroelasticity of Turbomachines (ISUAAAT12), no. I12-S7-3, Imperial College London, UK, 2009.

[12] C. G. Himmel, H. P. Hodson, Passive Air Jets for Loss Reductions in High Lift Low Pressure Turbines, in: ISABE, no. 1295, 2009.

[13] R. J. Volino, O. Kartuzova, M. B. Ibrahim, Experimental and Computational Investigations of Low-Pressure Turbine Separation Control Using Vortex Generator Jets, in: ASME Turbo Expo 2009: Power for Land, Sea and Air, no. GT2009-59983, Orlando, Florida, USA, 2009.

[14] J. Huang, T. C. Corke, F. O. Thomas, Plasma Actuators for Separation Control of Low-Pressure Turbine Blades, AIAA Journal 44 (1) (2006) 51–57.

[15] B. J. Abu-Ghannam, R. Shaw, Natural Transition of Boundary Layers - The Effects of Turbulence, Pressure Gradient and Flow History, Journal Mechanical Engineering Science 22 (5) (1980) 213–228.

[16] D. K. Walters, D. Cokljat, A Three-Equation Eddy-Viscosity Model for Reynolds-Averaged Navier-Stokes Simulations of Transitional Flow, ASME Journal of Fluids Engineering 130 (12) (2008) 121401.1–121401.14.

[17] S. Lardeau, N. Li, M. A. Leschziner, Large Eddy Simulation of Transitional Boundary Layers at High Free-Stream Turbulence Intensity and Implications for RANS Modeling, ASME Journal of Turbomachinery 129 (2) (2007) 311–317.

[18] E. R. van Driest, C. B. Blumer, Boundary Layer Transition: Freestream Turbulence and Pressure Gradient Effects, AIAA Journal 1 (6) (1963) 1303–1306.

[19] F. R. Menter, R. B. Langtry, S. R. Likki, Y. B. Suzen, P. G. Huang, S. Völker, A Correlation-Based Transition Model Using Local Variables - Part I: Model Formulation, ASME Journal of Turbomachinery 128 (3) (2006) 413–422.

[20] W. Piotrowski, W. Elsner, S. Drobniak, Transition Prediction on Turbine Blade Profile with Intermittency Transport Equation, in: ASME Turbo Expo 2008: Power for Land, Sea and Air, no. GT2008-50796, Berlin, Germany, 2008.

[21] P. Malan, K. Suluksna, E. Juntasaro, Calibrating the γ-Re$_\theta$ Transition Model, in: ERCOFTAC Bulletin 80, 2009, pp. 53–57.

[22] W. Elsner, W. Piotrowski, P. Warzecha, Transition Modelling with Intermittency Transport Equations, in: ERCOFTAC Bulletin 80, 2009, pp. 49–52.

[23] C. Content, R. Houdeville, Application of the γ-R$_\theta$ laminar-turbulent transition model in Navier-Stokes computations, in: AIAA 40th Fluid Dynamics Conference and Exhibit, no. AIAA 2010-4445, Chicago, Illinois, USA, 2010.

[24] R. E. Mayle, A. Schulz, The Path to Predicting Bypass Transition, ASME Journal of Turbomachinery 119 (3) (1997) 405–411.

[25] E. Dick, Eddy Viscosity Models for Turbulence and Transition, von Karman Institute for Fluid Dynamics Lecture Series 2009-08.

[26] J. Michálek, M. Monaldi, T. Arts, Aerodynamic Performance of a Very High Lift Low Pressure Turbine Airfoil (T106C) at Low Reynolds and High Mach Number with Effect of Free Stream Turbulence Intensity, in: ASME Turbo Expo 2010: Power for Land, Sea and Air, no. GT2010-22884, Glasgow, UK, 2010.

[27] P. R. Spalart, C. L. Rumsey, Effective Inflow Conditions for Turbulence Models in Aerodynamic Calculations, AIAA Journal 45 (10) (2007) 2544–2553.

[28] P. Chassaing, Turbulence en mécanique des fluides - Analyse du phénomène en vue de sa modélisation à l'usage de l'ingénieur, 1st Edition, Cépaduès-Editions, 2000.

[29] R. Corral, F. Gisbert, Prediction of Separated-Induced Transition Using a Correlation-Based Transition Model, in: ASME Turbo Expo 2010: Power for Land, Sea and Air, no. GT2010-23239, Glasgow, UK, 2010.

[30] R. B. Langtry, A Correlation-Based Transition Model using Local Variables for Unstructured Parallelized CFD codes, Ph.D. thesis, Universität Stuttgart (May 31 2006).

[31] R. Pacciani, M. Marconcini, A. Arnone, F. Bertini, A CFD Study of Low Reynolds Number Flow in High Lift Cascades, in: ASME Turbo Expo 2010: Power for Land, Sea and Air, no. GT2010-23300, Glasgow, UK, 2010.

[32] A. Benyahia, L. Castillon, R. Houdeville, Prediction of Separation-Induced Transition on High Lift Low Pressure Turbine Blade, in: ASME Turbo Expo 2011: Power for Land, Sea and Air, no. GT2011-45566, Vancouver, British Columbia, Canada, 2011.

[33] J. Michálek, A. Ilikan, T. Arts, A Comparison of High and Low Speed Aerodynamic Performance of a Very High Lift Low-Pressure Turbine Airfoil (T108) at Low Reynolds Numbers: Experimental Analysis and Numerical Prediction, in: 9th European Conference on Turbomachinery Fluid Dynamics and Thermodynamics, Istanbul, Turkey, 2011.

[34] W. B. Roberts, A Study of the Effect of Reynolds number and Laminar Separation Bubbles on the Flow through Axial Compressor Cascades, Ph.D. thesis, Université Libre de Bruxelles (May 1973).

Natural and Induced Transition on a 7deg Half-Cone at Mach 6

Davide Masutti

Aeronautics and Aerospace Department, von Karman Institute for Fluid Dynamics, Belgium, masutti@vki.ac.be

Supervisor: Olivier Chazot

Associate Professor, Aeronautics and Aerospace Department, von Karman Institute for Fluid Dynamics, Belgium, chazot@vki.ac.be

University Supervisor: Fulvio Scarano

Professor, Department of Aerospace Engineering, TU Delft, The Netherlands, F.Scarano@TUDelft.nl

Abstract

Pressure fluctuations caused by instabilities in the boundary layer are among the causes which lead to transition on a space vehicle during atmospheric re-entry. The knowledge of these unsteady fluctuations could help to identify the mechanisms which take part into the transition process and better predict them. With this target and in support of the EXPERT PL4/PL5 post-flight analysis, surface pressure measurements have been performed in the VKI H3 Hypersonic Wind Tunnel. A 7deg half-angle cone with exchangeable nosetip was equipped with a streamwise array of high frequency pressure transducers (PCB 132A31). Instabilities in the boundary layer have been investigated on a smooth surface and behind an isolated roughness element. The results provided on a simplified ground test model, show the growth of second mode waves under a laminar boundary layer and their break down to turbulence as a function of Reynolds number and streamwise location. Moreover the effect of an isolated roughness element on the boundary layer has been characterized in terms of generated instabilities.

Keywords: hypersonic, turbulence, boundary-layer transition, roughness, pressure measurements, infrared thermography

Nomenclature

δ^*	Displacement thickness of the nozzle walls
ρ_∞	Free-stream density
c_p	Heat capacity at constant pressure
$C_{F_{II}}$	Turbulent mean boundary layer parameter
k	Roughness height
Q_w	Heat flux
T_0	Total temperature
T_w	Wall temperature
u_∞	Free-stream velocity

1. Introduction

Laminar-to-turbulent transition during atmospheric re-entry is a major issue for vehicle design. The process of boundary layer transition is accompanied by an increase in surface heat transfer and skin friction on the vehicle. ESA EXPERT project addresses the testing of critical re-entry technologies, leading in particular, to a more accurate design and effective development of thermal protection and boundary layer transition control systems. In this frame, VKI is contributing to the project with a payload for induced transition studies. Pressure fluctuations in the boundary layer are among the causes which lead to instabilities and after to the turbulent breakdown in the boundary layer, the determination of these unsteady fluctuations is helping to identify the mechanism which takes part in the transition process. With this target, surface pressure measurements have been performed in the VKI H3 Hypersonic Wind Tunnel. A 7deg half-angle cone with exchangeable nose was equipped with a stream-wise array of high frequency pressure transducers (PCB 132A31). The use of these peculiar ultra high frequency sensors demand a dynamic calibration which has to be addressed in a shock tube. Instabilities in the boundary layer are also investigated, with respect to the tunnel noise influence and the induced laminar-to-turbulent transition mechanism. The results provided on standard ground test model, representative of the conical EXPERT's wall, are helping to enhance the understanding of the boundary layer transition characteristics for the forthcoming post-flight analysis on the EXPERT vehicle.

2. Experimental Setup

2.1. VKI H3 Mach 6 Hypersonic Wind Tunnel

All experiments have been performed in the H3 Hypersonic Wind Tunnel of the von Karman Institute for Fluid Dynamics. The VKI H3 test facility is a conventional noisy blow-down to vacuum type wind tunnel. It can provide a uniform axisymmetric jet with a diameter of 12 cm at Mach 6. Dried air is supplied from a 40 bar reservoir, which can deliver stable stagnation pressures ranging from 6 to 30 bar. Air is heated up in pebble-bed heater to a total temperature of 500K to avoid condensation in the test section. The unit Reynolds number of the flow can be varied between 6E6 1/m and 28E6 1/m. The wind tunnel is provided with a model injection mechanism to avoid blockage of the wind tunnel and also to avoid excessive heating of the model itself during the start-up. The test chamber is vacuumed prior to the test using a supersonic ejector. The model is injected into the hypersonic free-jet with a model injection arm, once the Mach 6 flow is fully established in the test chamber. The noise level (normalized Pitot pressure fluctuations) of the facility is approximately 1.6% and a turbulence level of 0.8% (more information can be found in Masutti and Spinosa [1].

2.2. Models

The wind tunnel model used for the pressure measurements is a stainless-steel/Plexiglas 7deg half-cone, 265mm long. Sharp (0.55mm radius) and blunt (2.5mm radius) nose tips were used in this test campaign. The model is composed by half cone made in steel and half cone made in Plexiglas; the singularity of this assembly allows simultaneous measurements with the high frequency pressure transducers and the infrared thermo camera. A sketch of the stainless-steel side of the cone and the location of the sensors are given in Fig. 1.

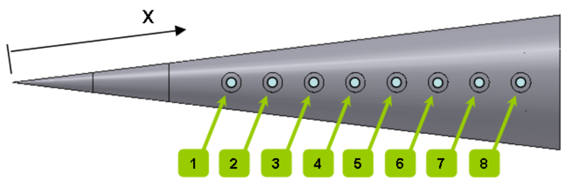

Figure 1: 7deg half-cone (side view)

Number	x [mm]	Sensor type
1	106	none
2	126	PCB132
3	146	none
4	166	PCB132
5	186	PCB132
6	206	Kulite XCE-093-50A
7	226	PCB132
8	246	PCB132

Table 1: PCB location on the 7deg half-cone

2.3. Instrumentation and data acquisition

Pressure fluctuations measurements and the instabilities investigation are performed on the cone model using PCB132A sensors. These sensors already prove their successful capabilities identifying and characterizing boundary layer instabilities [2; 3; 4; 5]. The PCB132A is a time-of-arrival sensor with a piezoelectric design. Because of its ability to detect very high frequency pressure fluctuations, the sensor is designed to have a bandwidth between 11 KHz and 1 MHz, therefore the mean pressure value information is not available. The PCB132A sensor, thanks to its very high resonant frequency (above 1MHz) is suitable to study boundary layer instabilities and their breakdown to turbulence. The sensor itself is a cylinder of 3.18 mm diameter and 7 mm length, although the real sensitive area (on top of the cylinder) is reduced to 1.6 mm^2. The diagonal of a 1.6 mm^2 square is equal approximately to 1.8 mm, this length can be considered as the spatial resolution of the sensor itself. Since the sensor was meant to be used to detect shock/pressure waves it has not yet been accurately calibrated for the purpose of investigating boundary layer instabilities. Different ways of calibrating the PCB sensors are in use or under investigation (see Beresh et al.[6] and

Berridge [5]). In this framework a new type of calibration has been investigated but since the results are still in the preliminary phase, the factory calibration is used to post-process the results analyzed from here on.

All the PCB132 sensors are powered by a PCB 482C05 signal conditioner (unity gain) which provides a constant-current excitation of 4mA to the piezoelectric sensing element. The signal conditioners are connected to a VKI custom made 40dB low-noise amplifier with a build-in 900 KHz Butterworth six-poles low-pass filter. The amplified signals are then digitally sampled at 2 MHz/channel by a 14-bit National Instruments PXI-6133. The power spectral densities of the PCBs' signal were calculated using the 'Power Welch Method' on 0.25 sec of samples. The evaluation of the power spectra was done with a 500 points Blackman window with 50% overlap and a frequency resolution of 4 kHz. The sensors location for the 7deg half-cone is defined in Table 1.

Infrared Thermography is used to provide a quantitative measure of heat transfer and is useful for quantifying increased surface heating due to laminar-to-turbulent transition. The radiation emitted by an object is a function of its surface temperature. Taking into account the emissivity of the surface, the reflected ambient radiation and the absorption in air or through optical elements [7], the Infrared Thermography can accurately measure the temperature of a body. For the latter reason, the IR technique is very suitable to study high-speed aerothermodynamics and atmospheric entry problems [8]. To capture the wall temperature evolution on the model, a FLIR ThermaCAM SC-3000 Infrared Camera has been used. The camera records a 320 x 240 pixels image at a max sampling frequency of 50Hz. The detector of the camera is cooled internally to 70K by a Stirling cycle. To assure a high IR transmissivity between the model surface and the IR camera, a germanium optical window is used. Despite the high transmissivity of germanium some residual reflections are present; this effect is then mitigated during the data reduction with a background subtraction procedure. The calibration is performed on a black body to relate the measured IR intensity to the model surface temperature.

$$St_{mod} = \frac{Q_w}{\rho_\infty u_\infty c_p \left(T_0 - T_w\right)} \tag{1}$$

The modified Stanton number (Santarelli and Charbonnier [9]) multiplied by the cubic root of the Reynolds number (Eq. 1) is used to display the status of the boundary layer on the cone.

3. Results

3.1. Natural Transition

The power spectral density (PSD) of five different PCB132A sensors mounted on the 7deg half-cone is computed to investigate the behavior of the instabilities taking part in the transition process. To represent the PSD of the pressure fluctuations measured by the PCB132A and compare the fluctuation amplitudes between them at different freestream conditions, the pressure fluctuations are normalized by the wall pressure [4] at the corresponding sensor location. Since the PCB132A sensor does not provide the mean value of the pressure, but only its fluctuations, the wall pressure for the 7deg half-cone has been computed using the freestream measured condition with the Taylor-Maccoll equation for supersonic/hypersonic cones at zero angle of attack [10]. The results are reported in Fig. 2, where the PSD of normalized pressure fluctuations on a smooth 7deg half-cone are investigated at different Reynolds number ranging from 6.75E6 1/m to 27.1E6 1/m. Instabilities at very high frequency can be seen in the PSD of the pressure fluctuations (Fig. 2). Those instabilities in the boundary layer were already identified by Tollmien and Schlichting in the '30s, then this early stability theory was revised and completed by Mack [11] in 1984. Mack demonstrated that the most dominant instabilities on a cone at zero angle of attack under hypersonic edge Mach numbers are second modes waves (called also Mack waves in his name). These instabilities are acoustic-like waves contained and reflected within the boundary layer, their frequency scales with the inverse of the boundary layer thickness itself as seen by Stetson and Kimmel [12] and Chokani [13]. Initially these second mode waves grow linearly before the location of transition and then they become nonlinear prior to the breakdown to turbulence.

Fig. 2(a) shows the initial amplitude of second mode waves growing with increasing downstream location, while their frequencies (represented by the peak frequency in the PSD) are decreasing downstream. The first PCB132A sensor, located at x = 126 mm from the nosetip, shows that the measured frequency for second mode waves is around 550 kHz. The second PCB132 at a location x=166mm is measuring the most unstable second mode waves at a peak frequency near 500 kHz. For the other locations at x = 186 mm, x = 226 mm and x = 246 mm, the second modes are measured around 450 kHz, 400 kHz and 370 kHz respectively. The fifth PCB132 at x = 246 mm also shows a weak harmonic of the second mode wave at a frequency around 750 kHz. Comparing the evolution of the second mode waves from Fig. 2(a) to Fig. 2(c) no wave breakdown and therefore no natural transition were detectable at a freestream Reynolds number below 14.1E6 1/m on the 7deg half-cone.

In the case of a freestream Reynolds number of 18E6 1/m (Fig. 2(d)), the first three PCB sensors are measuring second mode waves at a frequency respectively of 620 kHz, 520 kHz and 490 kHz, while the fourth PCB at x = 226mmm location shows a appreciable non-linear amplitude growth respect to the upstream sensors. The fifth sensor, x = 246 mm, is affected by a fully turbulent develop boundary layer although some instabilities are left over with a very

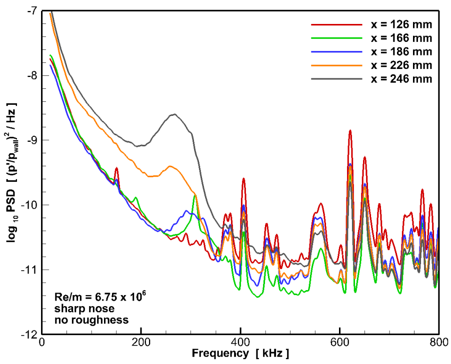

(a) PCB132 power spectral density for 7deg half-cone, Re/m = 6.75E6, no roughness

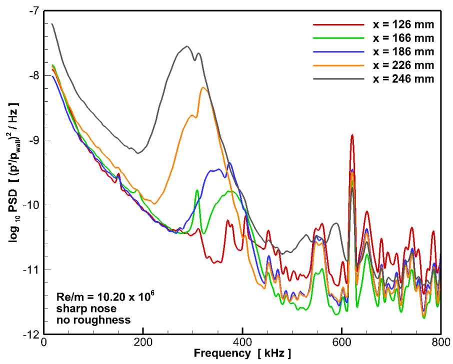

(b) PCB132 power spectral density for 7deg half-cone, Re/m = 10.2E6, no roughness

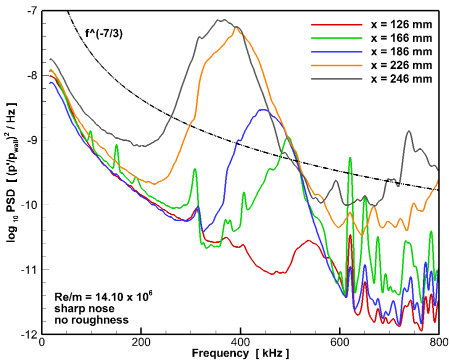

(c) PCB132 power spectral density for 7deg half-cone, Re/m = 14.1E6, no roughness

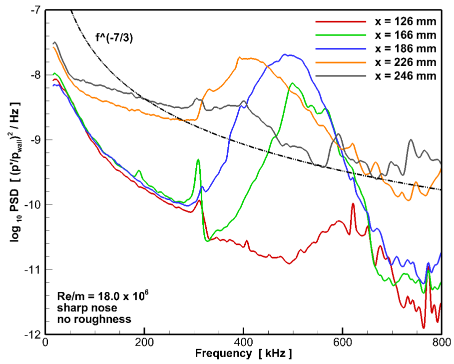

(d) PCB132 power spectral density for 7deg half-cone, Re/m = 18.0E6, no roughness

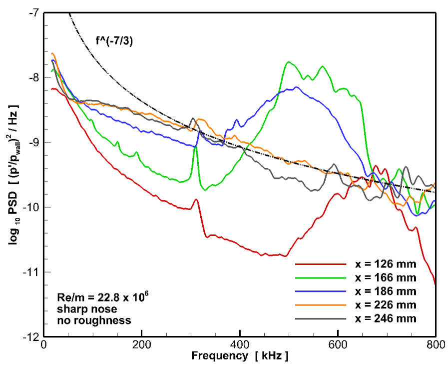

(e) PCB132 power spectral density for 7deg half-cone, Re/m = 22.8E6, no roughness

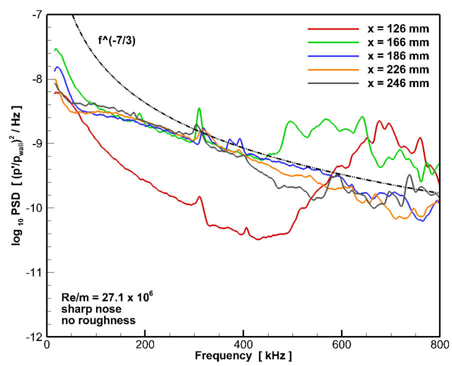

(f) PCB132 power spectral density for 7deg half-cone, Re/m = 27.1E6, no roughness

Figure 2: Second mode instabilities on a 7deg half-cone

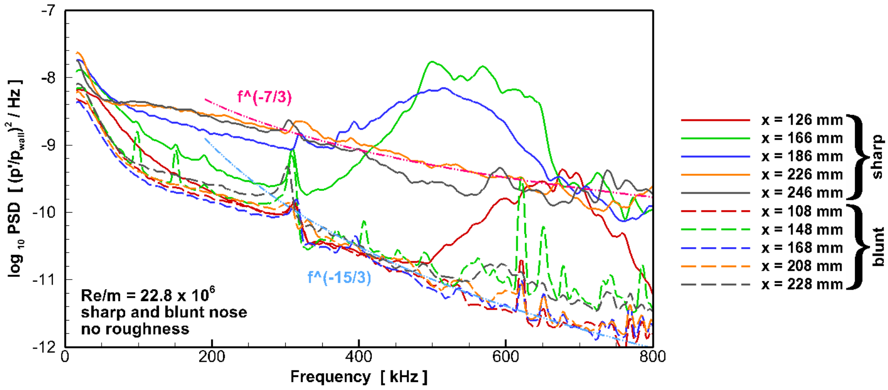

Figure 3: Nose bluntness effect on second modes

small amplitude. One can consider that the location of transition is somewhere between x = 226 mm and x = 246 mm for this Reynolds number. Increasing further the freestream Reynolds number, the natural transition front is moving upstream and more sensors are drowned in a turbulent boundary layer. In Fig. 2(e) the first two sensors are able to measure instabilities near frequencies of 670 kHz and 550 kHz, while the third one at x = 186 mm shows already a non-linear amplitude growth. The last two sensors, x = 226 mm and x = 246 mm, are measuring a fully developed boundary layer turbulent decay which is collapsing on a $f^{-7/3}$ curve. The $f^{-7/3}$ is the scale for turbulent decay of pressure for high wavenumbers [14], it differs from the classical Kolmogorov law of $f^{-5/3}$ because there is no directly dissipation of pressure with respect to velocity.

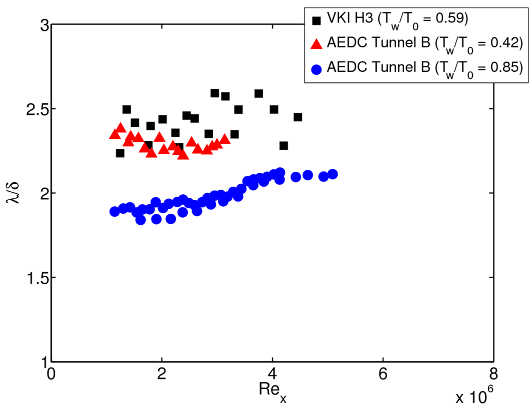

Figure 4: Approximate wavelength of second modes (replotted from Stetson and Kimmel [12])

Using a cross-correlation function on the signals from two adjacent sensors is possible to identify the velocity of the wave packets traveling downstream. The information on the velocity is then useful to compare with the boundary layer thickness and to compute the approximate wavelength of second modes. In Fig. 4, the wavelength of the second modes computed on a 7deg half-cone in VKI H3 conditions (T_w/T_0=0.59) are compared with results from Stetson and Kimmel [12] on a similar cooled and un-cooled 7deg half-cone in the AEDC Tunnel B at Mach 8 (T_w/T_0=0.42 and T_w/T_0=0.85). Fig. 4 shows that the ratio between the wavelength of the second mode waves and the boundary layer thickness on the cone is around 2.5, in good agreement with experimental measurements by Stetson and Kimmel. The nosetip bluntness effect on instabilities has also been investigated. In Fig. 3 are given the power spectral densities of pressure fluctuations on both a sharp (solid lines) and a blunt 2.5 mm cone (dashed lines). Measurements for the same Reynolds number of 22.8E6 1/m show how the second mode waves and the non-linear growth effects are suppressed by using a blunt nose on the cone. The origin of this phenomenon, extensively treated in the literature by Stetson [15; 16] and Singh et al. [17], is due to a layer of high specific entropy and strong entropy gradients in the inviscid flow.

This layer, simply known as entropy layer, is a region of high temperature and low density gas created by the large entropy due to the strong bow shock at the blunt nosetip [18]. The characteristics of the entropy layer, its thickness and its persistence in affecting the downstream boundary layer are a function of the bluntness of the vehicle and the freestream conditions [17]. The entropy layer, before being swallowed by the boundary layer, promotes changes of the flow

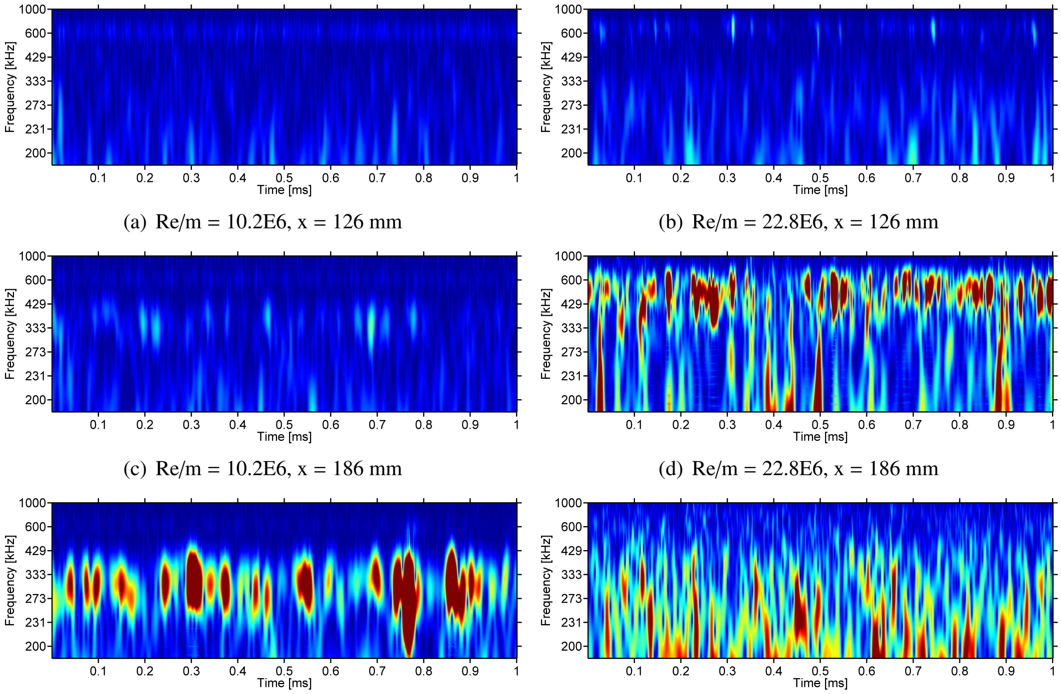

(a) Re/m = 10.2E6, x = 126 mm

(b) Re/m = 22.8E6, x = 126 mm

(c) Re/m = 10.2E6, x = 186 mm

(d) Re/m = 22.8E6, x = 186 mm

(e) Re/m = 10.2E6, x = 246 mm

(f) Re/m = 22.8E6, x = 246 mm

Figure 5: Wavelet analysis for different Reynolds number and sensors location

properties in the boundary layer itself. More precisely it induces a growth of the viscous layer, it changes the Mach number at the edge of the boundary layer and it also change the local Reynolds number. Because of these induced effects, the entropy layer helps to stabilize the boundary layer and moves backward the point in which transition occurs [19; 20]. From Fig. 3 can be observed how the PSDs of the pressure fluctuations on a blunt 7deg half-cone at VKI H3 conditions lie on a $f^{-15/3}$ curve, which is typical for a laminar boundary layer. One has to remember that in relation to the blunt body paradox, analyzed by Reshotko [21], a great increase of nose bluntness would generate a reversal in the transition front, bringing suddenly the natural transition front close to the nose. This latter behavior is also known in the literature as the 'transition-reversal phenomenon' (Rosenboom [20]) and its characterization is still an open issue.

3.1.1. Wavelet Analysis

A wavelet analysis has been applied to the signal of the PCB sensors for different Reynolds number and different locations. The analysis has been performed using a complex Morlet mother wavelet over a millisecond portion of the signal with 500 ns time resolution. Fig. 5 includes the analysis for two different Reynolds number 10.2E6 1/m and 22.8E6 1/m, at three different locations of 126 mm, 186 mm and 246 mm. Comparing the results given in Fig. 5(a), 5(c) and 5(e) for the same Reynolds number and increasing downstream distance, the second mode waves are increasing amplitude and decreasing frequency.

Second mode waves can be identified as wave packets traveling in the boundary layer at a random repetition rate. Through the wavelet analysis these wave packets can be cross-correlated and the computed velocity shows similar results as in Fig. 4. Considering a higher Reynolds number (Fig. 5(b), Fig. 5(d) and Fig. 5(f)), second mode instabilities appear at a higher frequency around 650 kHz at the location x = 126mm, in agreement with the PSD estimation shown in Fig. 2(e). Increasing the downstream location at x =186mm, the second mode waves are visible with a frequency around 500kHz. In this location the boundary layer in still not fully turbulent as from the PSD in Fig. 2(e) and is affected by an early stage of the breakdown to turbulence. This early breakdown process is visible in Fig. 5(d), where second mode wave packets are coexisting with turbulence traces (represented as red vertical lines in the wavelet analysis). At the end of the cone x = 246mm the boundary layer is fully turbulent, in Fig. 5(f) the second modes are completely disappeared and the wavelet analysis shows a chaotic trace.

3.1.2. Natural Transition Correlation

To characterize and compare natural transition onset location on a 7deg half-cone in VKI H3 conditions, the pressure fluctuations rms normalized by the computed Taylor-Maccoll mean wall pressure and the modified Stanton number (Eq. 1) from the infrared measurements are presented in Fig. 6. The modified Stanton number in Fig. 6 has been normalized by the cubic root of the Reynolds number. Experimental results as a function of the Reynolds number are compared with the Eckert theory for laminar and fully turbulent boundary layer. The results from the experiments show a visible boundary layer transition for unit Reynolds number of 27.1E6 1/m, 22.8E6 1/m and 18E6 1/m with the onset of natural transition respectively at 133mm, 150mm and 184mm. In the cases with Reynolds number of 14.1E6 1/m and 10.2E6 1/m no transition is visible because of the short length of the cone.

Moreover it is possible to compare the transition location on a 7deg half-cone in VKI H3 conditions with the Pate's transition correlation [22]. During the 70's, Pate conducted extensive research into transition in different conventional hypersonic wind tunnel. Pate firstly discover how freestream noise dominates the transition process on cones and flat plates, his work is still considered as a masterpiece. The correlation developed by Pate predicts the natural transition location on cones and flat plates at zero angle of attack. The correlation itself is based on tunnel noise parameters like the tunnel turbulent mean boundary layer parameter $C_{F_{II}}$ [23], the displacement thickness of the nozzle walls δ^* and the test section circumference. All the parameters and the correlation are described in detail in Pate's original manuscript [22].

In this analysis the transition locations obtained with the transition correlation at different unit Reynolds number of 27.1E6 1/m, 22.8E6 1/m 18E6 1/m and 14.1E6 1/m are respectively 152mm, 170mm 198mm and 233mm (values shown in Fig. 6 as vertical dashed line). Again Fig. 6 shows also the normalized pressure fluctuations for different sensor locations as a function of the freestream unit Reynolds number. A threshold of the normalize pressure fluctuations around a value of 0.02-0.025 represents the freestream noise level (see Masutti and Spinosa [1]) below which the boundary layer on the cone can be considered laminar. Streamwise pressure fluctuations during a laminar-to-turbulent transition process are characterized by the presence of a peak that occurs near the end of the transition process [22]. This peak can be observed in Fig. 6 for Reynolds number cases of 27.1E6 1/m, 22.8E6 1/m and 18.0E6 1/m. The last two PCB pressure sensors (226mm and 246mm) at unit Reynolds number of 14.1E6 1/m and 10.2E6 1/m, are affected by an anomalous recirculation phe-

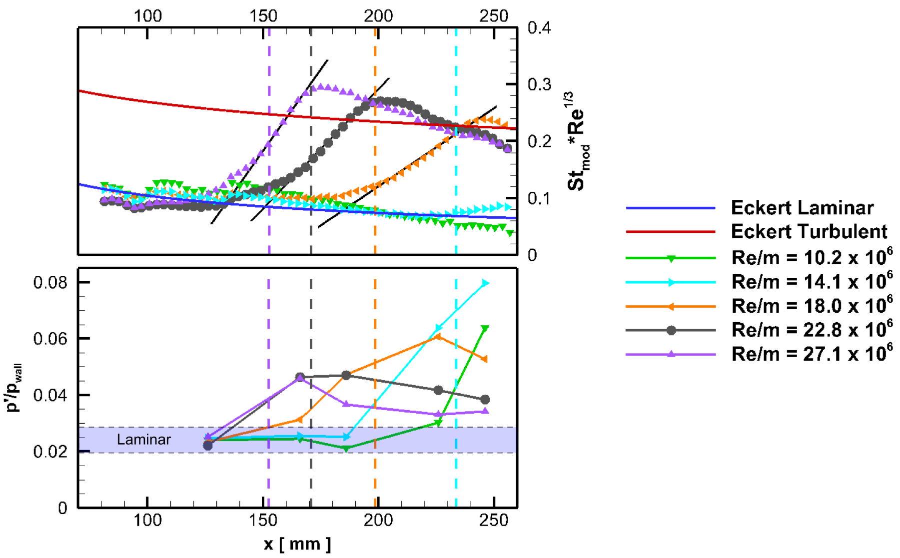

Figure 6: Natural transition and Pate correlation

nomena, so the peak in the normalized pressure fluctuations is not considered to be related to any transition in the boundary layer. The same anomalous recirculation has been observed also using the Infrared Thermography technique, but its effect was small if compared with the heat flux measured at the wall in a turbulent boundary layer.

Comparing in Fig. 6 the experimental results obtained and the Pate's transition correlation for cones, there is a fairly good agreement in the natural transition location. In particular, the location of transition inferred by the Infrared technique is always upstream of about 7-14% if compared with both the Pate correlation and the pressure fluctuation measurements. If pressure fluctuation and Pate correlation are analyzed, the peak of pressure fluctuations is generally downstream of the predicted transition location. The uncertainty of the transition location inferred by the PCB sensors is large because of the poor spatial resolution.

3.2. Roughness Induced Transition

To investigate the isolated roughness induced transition on a 7deg half-cone, a combination of measurements techniques has been used. The results obtained from fast pressure transducers, infrared thermography and oil visualization bring a set of complementary information. The use of infrared thermography alone is not enough to determine the status and the topology of the boundary layer. An infrared image at the model's wall could hide the vortex structures and moreover bring to an incorrect interpretation of the results. Fast pressure transducers at the wall, could add the unsteady information missing from the infrared technique and the oil flow can highlight the small vortex structure at the wall. Looking at Fig. 7 it is possible to see the effect on boundary layer transition of an isolated roughness element (ramp k=0.3mm placed at x=70mm). The group of images shows the effect of Reynolds number and nose bluntness on induced transition. Comparing Fig. 7(a) and Fig. 7(b) the effect of the Reynolds number can be observed on a sharp cone. The apex of the turbulent wedge [24], recognized as the transition location, is moving upstream closer to the isolated element as the Reynolds number increase. Moreover with a unit Reynolds number of 18E6/m natural transition is also present on the cone (Fig. 7(b), so induced and natural transition are coexisting.

On the other hand, with the blunt nose the effectiveness of the roughness element is decreasing. Comparing Fig. 7(a) and Fig. 7(c) the stabilizing effect of the entropy layer on the induced transition becomes clear. On a sharp cone, at a relatively low Reynolds number 7E6 1/m, the wake of the ramp is visible and characterized by a possible turbulent wedge at the end of the cone (Fig. 7(a)), while with a blunt nose the boundary layer on the cone is unperturbed and no wake is visible (Fig. 7(c)). Analyzing the effect of the nose at a higher Reynolds number around 18E6 1/m (Fig. 7(c) and 7(d)) the nose bluntness is stabilizing the natural transition (as discussed previously on Fig. 3) without any apparent interference on the induced turbulent wedge. Carefully observing the turbulent wedge in

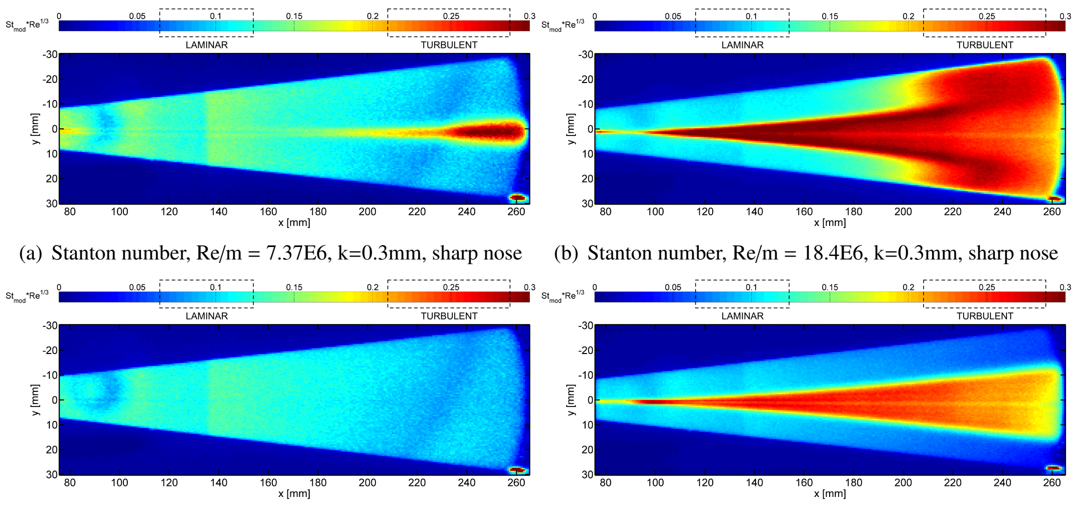

(a) Stanton number, Re/m = 7.37E6, k=0.3mm, sharp nose
(b) Stanton number, Re/m = 18.4E6, k=0.3mm, sharp nose
(c) Stanton number, Re/m = 7.04E6, k=0.3mm, blunt nose
(d) Stanton number, Re/m = 18.8E6, k=0.3mm, blunt nose

Figure 7: Infrared images on a 7deg half-cone

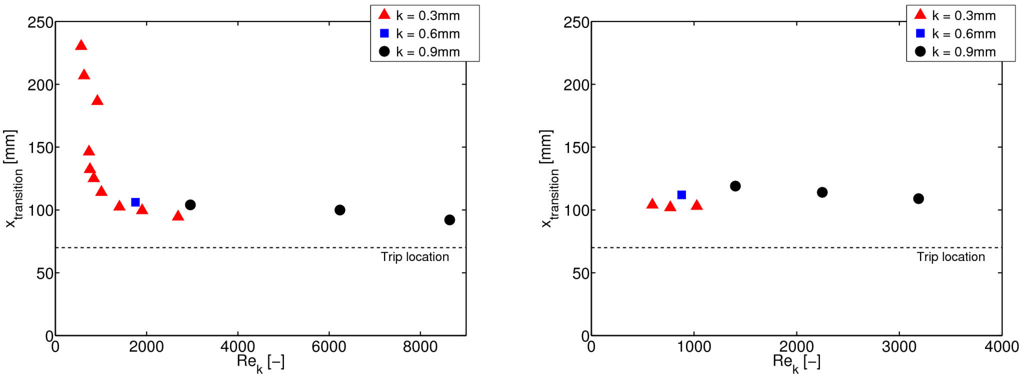

(a) Sharp cone (b) Blunt cone

Figure 8: Roughness transition location vs Reynolds number

Fig. 7(d), it is possible to distinguish some vortical structure in the boundary layer. A big colder line is present along the cone in the middle of the turbulent wedge, this line represent the accumulation line of the two big primary vortices created at the tip of the ramp element and flowing downstream attached to the wall. In addition to the two big vortices, are visible also four secondary colder line (two by side in a symmetric pattern), representing some secondary structures induced by the primary vortices. More details on these specific structures are provided on a flat plate in Tirtey [25].

The plots in Fig. 8 show the roughness induced transition location on a sharp and blunt 7deg half-cone as a function of the Re_{kk} parameter. As can be observed for the sharp nose in Fig. 8(a), the transition location moving closer to the location of the roughness element as soon as the Re_{kk} parameter is increasing. The transition location is approaching rapidly to the roughness element reaching an asymptote determined by the minimum incubation length for the development of the laminar-to-turbulent process in the boundary layer. Similar results are validated by observations of van Driest and McCauley [26] and Schneider [27] in both noisy and quiet wind tunnels. Fig. 8(b) represents similar results on a blunt 2.5mm nose, where only the asymptote of the minimum incubation length is obtained. Unfortunately with the test performed the downstream shift of the transition location was not observed therefore no comparison can be done.

3.2.1. Oil flow visualization

The oil visualization technique has been used to highlight some of the structure hiding in the boundary layer. These structures are mainly primary and secondary vortices created in the wake of an isolated roughness element. Fig. 9 shows the experimental results obtained with the oil flow technique on a 0.9 mm height ramp at a Reynolds number of 18E6/m for different nose bluntness. A detailed sketch of the vortex topology is given in Fig. 10. A primary set of vortices is created from the sides of the roughness element because of the pressure gradient resulting from the shape of the ramp itself. This pressure gradient is thus generating a pair of contra-rotating vortices which are flowing downstream attached to the wall. Right at the back of the ramp there is a so called 'dead-air region' characterized by a recirculation zone downstream the backward facing step of the ramp. Following the 'dead-air region' from Fig. 10 an accumulation line is observed, where the residual oil on the surface is pushed by the contra-rotating vortices. To maintain the momentum balance in the flow, every primary vortex is coupled with another contra-rotating vortex on the side (see the bird tail footprint of the primary couple of vortices in Fig. 10). Following downstream the wake of the roughness, a pair of new vortices (secondary couple of vortices) are induced by the momentum of the primary ones. These secondary vortices are visible in the sketch of Fig. 10 and in the experimental results in Fig. 9. Can be observed that these new secondary vortices are separated from the primary ones by an accumulation line of oil.

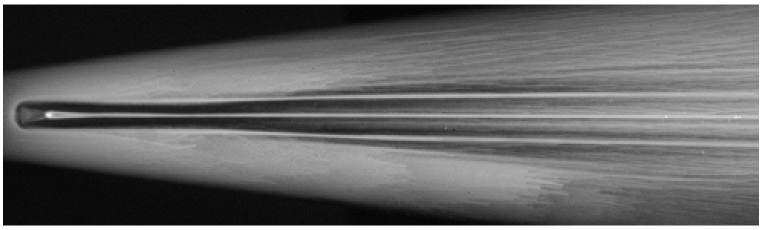

(a) Oil visualization on a sharp cone, ramp k=0.9mm, Re=18E6/m

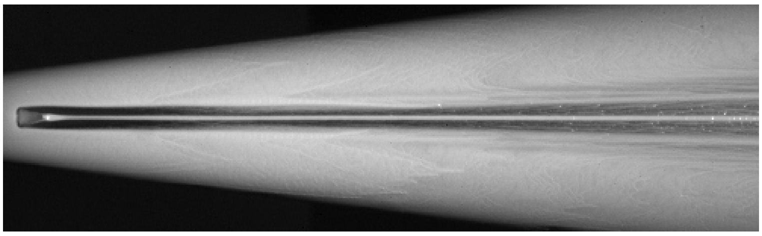

(b) Oil visualization on a blunt 2.5mm cone, ramp k=0.9mm, Re=18E6/m

Figure 9: Oil visualization

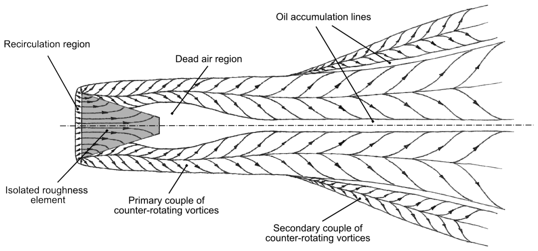

Figure 10: Vortex topology

Generally all these vortices tend to diverge because of the conical nature of the flow around the model. Comparing Fig. 9(a) and 9(b) can be observed the effect of the nose bluntness. In particular, the two pictures 9(a) and 9(b) differ from each other not only by the footprint of the induced wake but also by a visibly different background on the cone surface. This background in Fig. 9(a) is typical of a reduced oil thickness due to the increased skin friction in a turbulent boundary layer, while the same background in Fig. 9(b) in clearly not affected by any transition and the oil surface is smooth all along the cone. The main conclusion is that the nose bluntness is apparently changing the topology of the vortex, the same pair of primary contra-rotating vortices are present in both cases. Carefully observing Fig. 9(b) also the secondary vortices are present, but their appearance is delayed downstream with respect to the sharp nose case. This phenomenon is probably linked to the entropy layer developing from the blunt nose of the cone.

4. Conclusions

Second mode waves have been measured in the VKI H3 Hypersonic Wind Tunnel. Initial growth of second mode modes has been confirmed on a smooth 7deg sharp half-cone. Frequency of second modes is decreasing with increasing downstream measurement location. Moreover, frequency of second modes are also increasing with the increasing Reynolds number and the thinning of the boundary layer since instabilities frequencies are scaling with the inverse of boundary layer thickness. Second mode breakdown has been observed starting from a Reynolds number of 18E6 1/m on the rear part of the 7deg half-cone. With the increasing Reynolds number, several sensor locations were affected by breakdown to turbulence validating the upstream movement of the onset of natural transition. The effect of nose bluntness has been also characterized, showing that a strong entropy layer created by the bow shock is able to change the boundary layer characteristics, like Mach number at the edge, stabilizing the boundary layer itself and damping all the instabilities. From these typical results, on standard models, it appears that the transition phenomenon is strongly linked to the characteristic of the boundary layer. Considering this last statement further investigations are necessary for a more accurate flight extrapolation in the perspective of the EXPERT post-flight analysis.

References

[1] D. Masutti, E. Spinosa, Disturbance Level Characterization of a Hypersonic Blow-Down Facility, in: 41th AIAA Fluid Dynamics Conference, Honolulu, June 2011, AIAA-2011-3887.

[2] K. Fujii, Experiment of the Two-Dimensional Roughness Effect on Hypersonic Boundary-Layer Transition, Journal of Spacecraft and Rockets 43 (4) (2006) 731–738.

[3] M. Estorf, R. Radespiel, S. P. Schneider, Surface-Pressure Measurements of Second-Mode Instability in Quiet Hypersonic Flow, in: 46th AIAA Aerospace Sciences Meeting and Exhibit, Reno, January 2008, AIAA-2008-1153.

[4] K. M. Casper, Hypersonic Wind-Tunnel Measurements of Boundary-Layer Pressure Fluctuations, in: 39th AIAA Fluid Dynamics Conference, San Antonio, June 2009, AIAA-2009-4054.

[5] D. C. Berridge, Measurements of Second-Mode Instability Waves in Hypersonic Boundary Layers With A High-Frequency Pressure Transducer, Master's thesis, Purdue University (2010).

[6] S. J. Beresh, J. F. Henfling, R. W. Spillers, , B. O. M. Pruett, Measurement of Fluctuating Wall Pressures Beneath a Supersonic Turbulent Boundary Layer, 48th AIAA Aerospace Sciences Meeting.

[7] T. Arts, H.-L. Boerrigter, J.-M. Buchlin, M. Carbonaro, G. Degrez, Introduction to Measurement Techniques in Fluid Dynamics, von Karman Institute for Fluid Dynamics, 2001.

[8] C. O. Asma, J. Thoemel, S. Paris, O. Chazot, Utilization of infrared thermography to investigate atmospheric entry aerothermodynamics of space vehicles at von Karman Institute, in: QIRT 2008, 9th International Conference on Quantitative Infrared Thermography, Krakow, July 2008.

[9] P. Santarelli, J. Charbonnier, Heat Transfer Data Reduction User Guide for the VKI-H3 Wind Tunnel, Tech. rep., von Karman Institute (February 1999).

[10] J. D. Anderson, Modern Compressible Flow, McGraw-Hill Science, 2002.

[11] L. H. Mack, Boundary-Layer Linear Stability Theory, Tech. rep., Jet Propulsion Laboratory (1984).

[12] K. F. Stetson, R. L. Kimmel, On Hypersonic Boundary-Layer Stability, in: 30th Aerospace Sciences Meeting & Exhibit, Reno, January 1992, AIAA 92-0737.

[13] N. Chokani, Nonlinear evolution of Mack modes in a hypersonic boundary layer, Physics of Fluids 17-1 (January 2005) doi:10.1063/1.1825471. `doi:10.1063/1.1825471`.

[14] W. K. George, P. D. Beuther, R. E. A. Arndt, Pressure spectra in turbulent free shear flows, Journal of Fluid Mechanics 148 (1984) 155–191, doi:10.1017/S0022112084002299. `doi:10.1017/S0022112084002299`.

[15] K. F. Stetson, Nosetip bluntness effects on cone frustrum boundary layer transition in hypersonic flow, in: 16th AIAA Fluid and Plasma Dynamics Conference, Danvers, July 1983, AIAA-83-1763.

[16] K. F. Stetson, Comments on Hypersonic Boundary-Layer Transition, Tech. rep., Wright Research & Development Center (September 1990, WRDC-TR-90-305 7).

[17] D. J. Singh, A. Kumar, S. N. Tiwari, Effect of Nose Bluntness on Flow Field Over Slender Bodies in Hypersonic Flows, in: 27th AIAA Aerospace Sciences Meeting, Reno, Janaury 1989, AIAA-89-0270.

[18] J. D. Anderson, Hypersonic and High Temperature Gas Dynamics, American Institute of Aeronautics & Astronautics, August 2000.

[19] K. F. Stetson, E. Thompson, J. Donaldson, L. Siler, Laminar Boundary Layer Stability Experiments on a Cone at Mach 8, Part 2: Blunt Cone, in: 22nd AIAA Aerospace Science Meeting, Reno, January 1984, AIAA-84-0006.

[20] I. Rosenboom, S. Hein, U. Dallmann, Influence of Nose Bluntness on Boundary-Layer Instabilities in Hypersonic Cone Flows, in: 30th AIAA Fluid Dynamics Conference, Norfolk, June 1999, AIAA-99-3591.

[21] E. Reshotko, Roughness-Induced Transition Transient Growth in 3-D Supersonic Flow, Tech. rep., RTO/NATO (2008, RTO-EN-AVT-151-12).

[22] S. R. Pate, Dominance of Radiated Aerodynamic Noise on Boundary Layer Transition in Supersonic-Hypersonic Wind Tunnels, Tech. rep., Arnold Engineer Development Center (March 1978, AEDC-TR-77-107).

[23] E. van Driest, The Problem of Aerodynamic Heating, Aeronautical Engineer Review (1956) 26–41.

[24] A. Fiala, R. Hillier, Aerothermodynamic of Turbulent Spots and Wedges at Hypersonic Speed, in: 5th European Symposium on Aerothermodynamics for Space Vehicles, November 2004.
URL `http://articles.adsabs.harvard.edu//full/2005ESASP.563..615F/0000615.000.html`

[25] S. Tirtey, Characterization of a Transitional Hypersonic Boundary Layer in WindTunnel and Flight Conditions, Ph.D. thesis, ULB (2009).

[26] E. R. van Driest, W. D. McCauley, The effect of controlled three-dimensional roughness on boundary layer transition at supersonic speeds, Tech. rep., North American Aviation, Inc. (November 1958).

[27] S. P. Schneider, Effects of Roughness on Hypersonic Boundary-Layer Transition, School of Aeronautics and Astronautics, Purdue University.

A Free-stream and Boundary Layer Characterization of the Longshot Contoured Hypersonic Nozzle

Guillaume Grossir

Aeronautics and Aerospace Department, von Karman Institute for Fluid Dynamics, Belgium, grossir@vki.ac.be

Supervisor: Patrick Rambaud

Assistant Professor, Aeronautics and Aerospace Department, von Karman Institute for Fluid Dynamics, Belgium, rambaud@vki.ac.be.

University Supervisor: Herman Deconinck

Professor, Université Libre de Bruxelles, Belgium, deconinck@ulb.ac.be.

Abstract

A flow characterization of the VKI Longshot contoured hypersonic nozzle is performed using a static pressure probe and a boundary layer pitot rake. Static pressures larger than expected are recorded denoting a possible non-isentropic flow expansion. Turbulent boundary layers are measured at three different locations from the nozzle exit up to half the nozzle length. Turbulence intensities are determined at the nozzle exit and show levels expected for a conventional noisy wind tunnel. Direct flow visualization is used for further characterization of the flow into the test section. It reveals an unexpected excited test gas during the flow establishment followed by a bright flash around the hypersonic jet during testing time. This deeper characterization of the flow will allow for future boundary layer transition experiments to be performed in a better known environment.

Keywords: Hypersonic, Mach number, Reynolds number, Longshot, wind-tunnel, boundary layers, laminar, turbulent, transition, nozzle, non-isentropic, free-stream, noise levels, turbulence intensities.

Nomenclature

Symbols

C_p	pressure coefficient, -
d	distance to the nozzle wall, mm
D	static pressure probe diameter, mm
f	frequency, Hz
M	Mach number, -
p	flow pressure, Pa
r	radial distance from nozzle center line, mm
Re	Reynolds number, -
t	time, ms
T	flow temperature, K
x	distance from nozzle exit, mm
γ	specific heat ratio, -
ρ	flow density, kg/m^3
τ	response time, ms
$\varnothing$	diameter, mm

Subscripts/Superscripts

0	stagnation conditions in nozzle reservoir
e	at boundary layer edge
$exit$	based on nozzle exit diameter
in	based on probe inlet diameter
lam	laminar
unit	based on a 1 m reference length
res	resonance
$static$	static quantity
t_2	total conditions after a normal shock wave
∞	free-stream value
$'$	perturbation

Abbreviations

B.L.	boundary layer
fps	frames per second

1. Introduction

Transition to turbulence phenomenon in hypersonic flows is known to be very sensitive to the quality of the upstream environment among numerous other parameters. The free-stream noise levels are of particular interest as reported in [1; 2; 3] and the largest levels promote earlier transition on models located within the test section as clearly shown in Fig. 1.

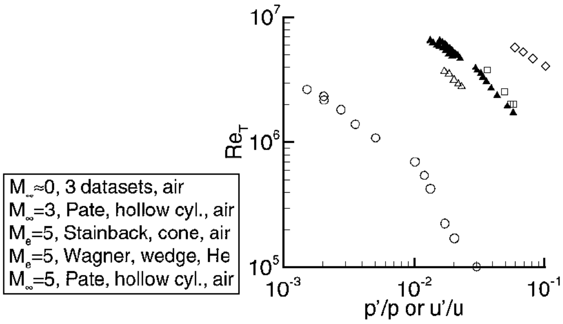

Figure 1: Transition Reynolds number data plotted as a function of the measured disturbance levels ([4])

The origin of disturbances in the free-stream can be divided into three contributions: vorticity fluctuations (turbulence), entropy variations (temperature spottiness) and sound waves (pressure fluctuations) ([5; 6]), each of them issuing from various sources shown in Fig. 2. Ideally, a complete characterization of each type of the disturbances in an hypersonic facility is required. However, for Mach numbers larger than 2.5, pressure fluctuations may be the dominant source as shown by [5]. These are pressure radiations from the turbulent boundary layers developing along the nozzle walls and these noise levels are proportional to the amount of nozzle wall covered by a turbulent boundary layer ([7]). Moreover, these pressure fluctuations are proportional to the fourth power of the free-stream Mach number [1; 3] thus increasing significantly for high Mach numbers facilities.

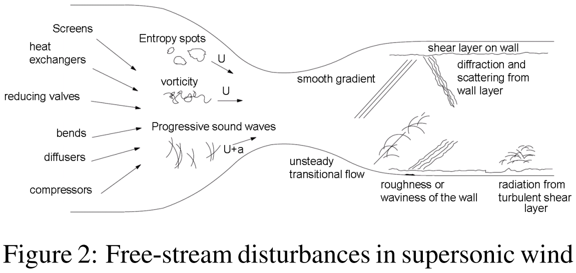

Figure 2: Free-stream disturbances in supersonic wind tunnels ([3])

Therefore, in agreement with the recommendations stated in [8] for any turbulence studies in hypersonic flows, it is first required to determine with accuracy the surrounding environment before attempting any transition characterization on given geometries. The purpose of the experimental campaign reported herein was to characterize the flow of the VKI Longshot hypersonic facility which will be used for future boundary layer transition studies.

This paper focuses on the characterization of nozzle wall boundary layers and on the determination of the free-stream noise levels. Free-stream static pressure measurements are also conducted along the nozzle in order to determine with a better accuracy the free-stream Mach numbers. Finally, flow characterization is supported by flow visualization.

2. Experimental setup

2.1. Probes and instrumentation

2.1.1. Free-stream static pressure probe

A recently manufactured free-stream static pressure probe (shown in Fig. 3) was designed to better characterize the free-stream and to reconstruct with a better accuracy the different flow quantities such as free-stream Mach or Reynolds numbers. A Kulite XCQ-093 with a range of 14000 Pa is used for the static pressure measurements. The first results reported in [9] showed a poor reliability of the probe whose measurement was repeatedly lost after few ms into each experiment. Nevertheless, a first analysis of the recorded pieces of data showed Mach numbers surprisingly lower than expected in the free-stream. These results were to be improved and confirmed by more accurate measurements which will now be reported in section 3.

2.1.2. Boundary layer stagnation pressure rake

A newly designed boundary layer stagnation pressure rake has been used to characterize the boundary layers developing along the nozzle walls and to determine the free-stream noise levels. In order to perform measurements of free-stream disturbances, the frequency-response of the probe must be sufficiently high. The best solution is to use pressure sensors directly exposed to the flow so that no cavities can introduce either fluctuation damping or response delays. However, the VKI Longshot facility is known to be seeded by particles issuing from upstream diaphragms and other elements. Direct exposition of the sensors

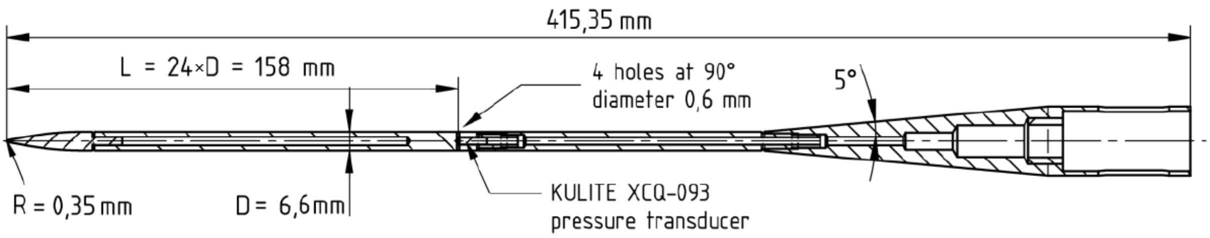

Figure 3: Static pressure probe following the design of Nagamatsu ([9])

to the flow presents large risks of destroying them and therefore sensors must be protected.

The mounting of each pressure sensor together with its protective elements is shown in Fig. 4. The pressure sensor is mounted at the end of a thin tube and a thick screen (drilled with four holes with $\varnothing = 0.5$ mm) is located in front of it, held by a cap. The inlet diameter of the cap is $\varnothing_{in} = 1.5$ mm. The chicane introduced should reduce the risks of direct particle impact on the membrane of the sensor. The volume of the cavities and tubes introduced is 8.5 mm^3 which influences the frequency response of the sensors. From shock tube calibration, the response time is $\tau \approx 14\mu s$, and the resonance frequency of the system is $f_{res} \approx 20$ kHz.

A total of 7 fast-response Kulite XCE-093 with a range of 100000 Pa sensors are installed in a rake support shown in Fig. 5.

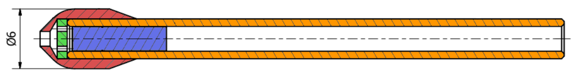

(a) Design (cap, screen, tube and sensor)

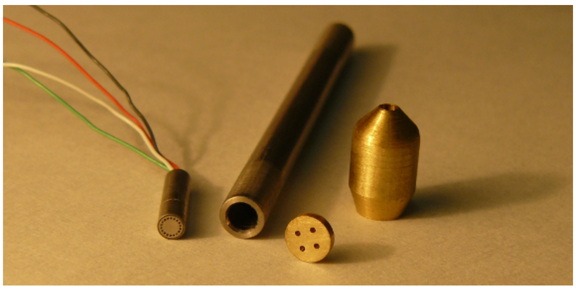

(b) Exploded view

Figure 4: Pitot tube

2.2. Facility

The VKI Longshot hypersonic facility is used with a 3 m long contoured nozzle having an exit diameter of $\varnothing_{exit} = 426$ mm. It is designed to attain Mach

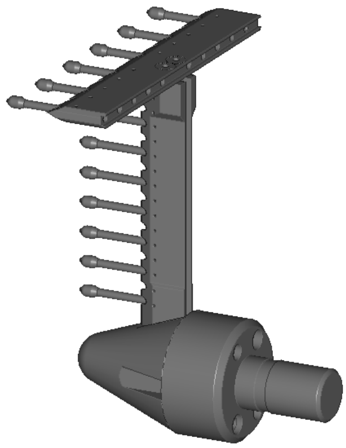

(a) Pressure rake design

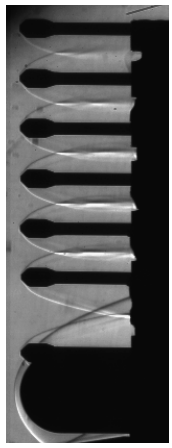

(b) Schlieren of the rake (additional probes in the view)

Figure 5: Pressure rake for boundary layer characterization

14. Test gas is N_2. The test section is located into a closed tank of 15 m^3 initially vacuumed to $p \approx 0.1$ Pa. The structure of the jet changes from under-expanded at the beginning of an experiment to over-expanded at the end of the experiment due to the decreasing stagnation conditions with time and rising pressure into the test section.

2.3. Test matrix

The experiments reported here are all using a ”Low” Reynolds number condition (varying with time between $9.5 \times 10^6 \gtrsim \mathrm{Re}_{\mathrm{unit}} \gtrsim 5.5 \times 10^6$/m, 2500 K $\gtrsim T_0 \gtrsim$ 1000 K, 1200 bar $\gtrsim p_0 \gtrsim$ 200 bar). This is the lowest Reynolds number conditions achievable by the facility and it was chosen in order to delay boundary layer transition along the nozzle walls and thus decrease free-stream noise levels.

Test times are of the order of $t \approx 20$ ms at the nozzle exit and $t = 0$ is chosen as the time where the measured reservoir pressure reaches half of its peak amplitude.

Boundary layer characterization using the pressure rake has been performed at three locations along the nozzle axis: at the nozzle exit ($x = 0$ mm) and inside the nozzle ($x = -750$ and -1500 mm) as shown in Fig. 6 where the background colors are representing the total pressure after a shock wave p_{t_2}. Measurements have been performed from the nozzle center line up to 9.5 mm to the wall.

Static pressure measurements were performed only at $x = 0$ and -750 mm, both at $d \approx 130$ mm and within the uniform Mach 14 core according to available laminar CFD computations.

2.4. Data acquisition

Data were acquired at 500 kS/s using a 16-bit PXI-6123 module for the static pressure probe (signal was amplified by 500 using a Fylde amplifier (FE-351-UA)), and at 2.5 MS/s for the boundary layer rake using a 14-bit PXI-6133 module. Both modules were mounted on a National Instruments PXI-1045 chassis.

3. Longshot free-stream measurements

3.1. Modifications to the static pressure probe

The cause of initially poor signal quality (see [9]) has been identified as being due to a sensitivity of the static pressure sensor to mechanical vibrations induced by the flow. The probe has been stiffened and mounted directly onto a sting instead of using lateral supports.

Also, the previous design of the probe was using 4 tapered holes connected to one single chamber for the static pressure measurement. Their inlet diameter was 0.8 mm but the influence of the tapered shape on the measurements was questionable ([H. Olivier, priv. comm.]). Thus, the probe has been modified by fitting precision tubes inside the existing holes, reducing the inlet diameter to 0.6 mm but allowing to fill with a compound the tapered inlet. The surface has then been polished until it matched the surrounding shape. This is shown in Fig. 7. According to the results presented in [10], the reduced inlet diameter may increase slightly the viscous effects in the tubes and lead to measured pressures about 2-3% larger than previously.

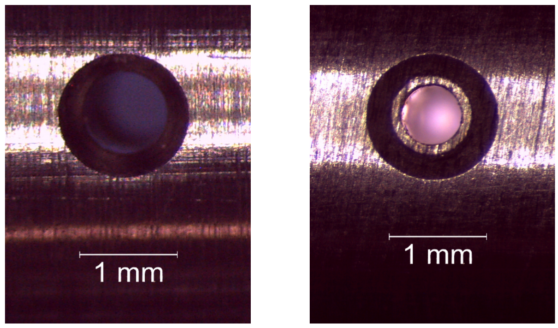

(a) Old design with tapered holes, $\varnothing_{in} = 0.8\ mm$

(b) New design with straight holes, $\varnothing_{in} = 0.6\ mm$

Figure 7: Inlet holes of the static pressure probe

The influence of viscous effects increasing the static pressure along the probe cannot be checked with the present design and one had to rely on CFD results to determine the static pressure measurement location. A second probe is being manufactured with several sensors at different locations from the nosetip in order to evaluate the influence of these viscous effects along the probe and to confirm the present results.

3.2. Results

The free-stream static pressure measured at the nozzle exit and at $x = -750$ mm inside the nozzle and using tapered or straight holes is reported in Fig. 8. The decay measured follows the typical decay of the

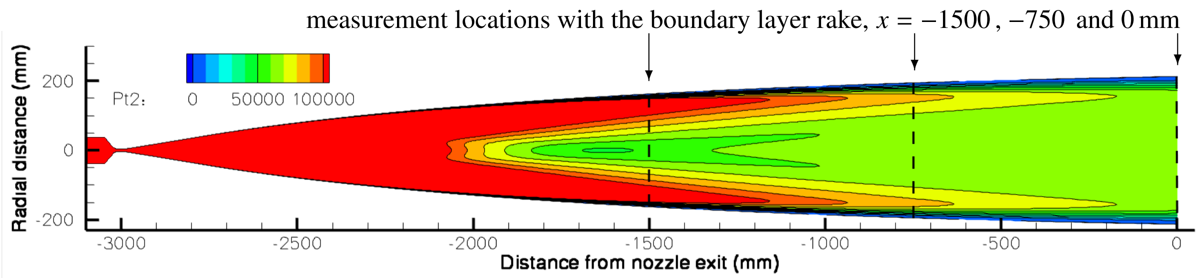

Figure 6: Measurement locations along the nozzle on top of CFD prediction of stagnation pressure p_{t_2} for t=0 ms

reservoir conditions of the wind-tunnel. The quality of the measurements has been improved with respect to previous tests by reducing the amplitude of the oscillations. Since the probe stiffening, measurements could be performed over the whole test duration for every single test.

The steady calibration of the probe lead to measurements uncertainties about 5.4%. Additionally, the sensor used has a combined linearity, hysteresis and repeatability uncertainty of ±15 Pa according to manufacturer specifications which shows the poor accuracy achievable when compared to the free-stream pressure range of few hundreds of Pa. The oscillations measured by the probe are within these uncertainty limits and may simply be related to the sensor capabilities. It is clear that the high-frequency free-stream static pressure fluctuations that could be used as an indicator of the free-stream noise levels cannot be retrieved with this probe due to design limitations.

The modification of the inlet holes shape does not seem to influence strongly the measurements performed at $x = -720$ mm inside the nozzle. The repeatability is excellent and the influence of the reduced diameter of the probing holes (inducing larger viscous effects) is within the uncertainty of the probe.

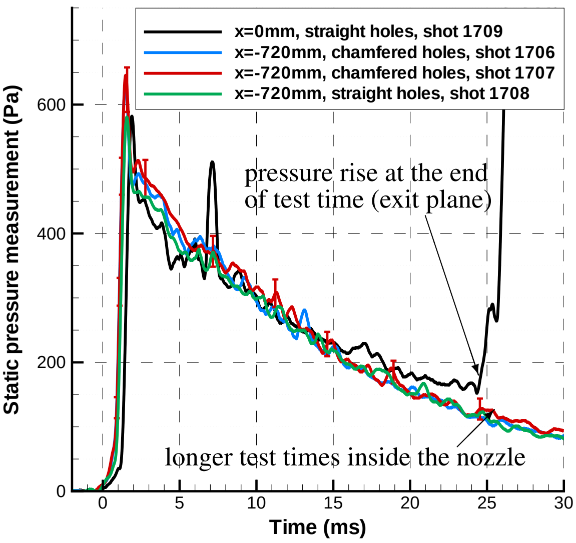

Figure 8: Measured static pressure

The trend of the decaying static pressure at the nozzle exit is different from measurements inside the nozzle and other measurements are being performed to confirm this trend. The pressure recorded in the nozzle is slightly larger than at the exit at the beginning of an experiment. The peak recorded at the nozzle exit at $t \approx 7$ ms is likely to be an external perturbation ans should be disregarded. The tendency is then inverted at $t \approx 12$ ms due to a difference in the decay trends of the measurements at these two locations. Larger static pressures at the exit of a nozzle than inside have already been reported in other hypersonic facilities and may be due to various non-isentropic flow phenomena in the nozzle.

For instance, vibrational freezing followed by relaxation of the heated test gas coming from the reservoir of the nozzle [11; 12] or flow condensation enhanced by impurities seeding the flow and acting as nucleation sources [13; 14; 15; 16] must be investigated. In both cases, heat would be progressively released into the free-stream, rising the free-stream static temperature and changing other related free-stream properties such as the Mach number. The static pressure is directly affected by such process and is an excellent way to detect non-isentropic flow expansions. Other phenomena such as the relaxation time of specific heats or the presence of shock waves inside the nozzle due to imperfections along the nozzle walls need to be examined.

3.3. Free-stream Mach number determination

The free-stream Mach number can be rebuild using various measurements. Ratios of test section stagnation pressure to reservoir stagnation pressure p_{t_2}/p_0 and static pressure to test section stagnation pressure p_{static}/p_{t_2} will be used here. The second method using p_{static}/p_{t_2} leads to free-stream Mach numbers much lower than the ones expected from the design of the nozzle and the ones rebuild using p_{t_2}/p_0 (Fig. 9). The uncertainties on the Mach numbers do not even overlay each other. This mismatch is mainly due to a measured static pressure being about twice larger than expected and is likely to be due to a non-isentropic flow phenomenon to be identify further. This could also be due to viscous effects along the probe much larger than predicted by CFD and fooling the measurements.

Static pressure measurements inside the nozzle lead to increasing free-stream Mach number during the experiments with a repeatable trend. This is not observed for the experiment at the nozzle exit although there is also a slope change at $t = 7$ ms. This trend is coming from the static pressure measurements reported in Fig. 8. Although the reason has not yet been identified precisely, it could be due to less severe vibrational mode relaxation with the decaying reservoir temperature. Flow condensation would be expected to increase during an experiment due to the decaying

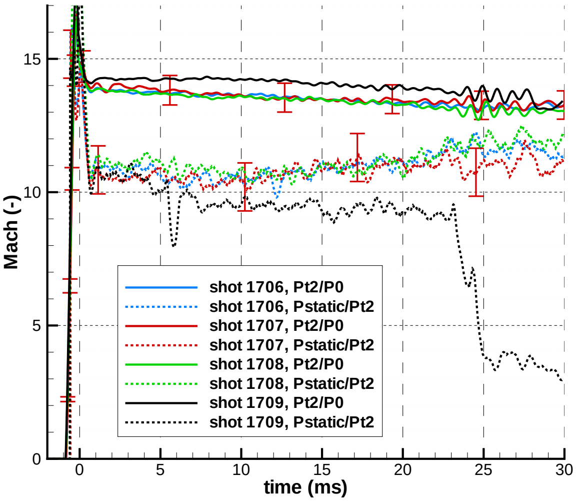

Figure 9: Free-stream Mach number determined from p_{t_2}/p_0 and p_{static}/p_{t_2}

flow static temperature. This should lower further the Mach number which is not observed here.

4. Boundary layers characterization

4.1. Purposes

Boundary layers along the 3 m long contoured nozzle have not yet been characterized despite two decades of regular tests. A turbulent nozzle wall boundary layer would strongly influence the free-stream environment by rising the noise levels. Regarding the length of the nozzle, it is believed that the boundary layers are turbulent in the exit plane. However, since the nozzle uses a contoured design, there is a cone of uniform flow inside the nozzle as shown in Fig. 10 and thus if transition is appearing far enough downstream the nozzle throat, it would be possible to have a small but useful "quiet" core. In this zone, the noise radiated by the nozzle wall boundary layers would remain relatively low and be closer to the conditions encountered in real flight. To assess this possibility, measurements inside the nozzle are required to characterize the boundary layers and to determine the free-stream noise levels. From CFD computations, the uniform part of the flow inside the contoured nozzle starts at $x \approx -1.5$ m. By following a characteristic line, the critical location for the boundary layer transition radiating noise into the free-stream is at $x \approx -1.8$ m .

4.2. Boundary layer profiles

4.2.1. Mean values

Successive measurements were performed with the few sensors available at the nozzle exit in order to obtain complete profiles of the stagnation pressure across the nozzle. This procedure was then repeated at several locations along the nozzle. The stagnation pressure (at various time instants during the test time) is plotted in Fig. 11 where the decay is again due to the decreasing reservoir conditions with time.

Nozzle wall boundary layers are clearly visible and are about 100 mm thick.

The large peak at the end of the test time is due to the closure of the hypersonic jet. This time mainly depends upon the location across and along the nozzle and only slightly with test conditions. The latter characterization will be developed in section 4.2.4.

The free-stream noise levels are slightly visible as fluctuating stagnation pressure and will be analyzed further in section 4.2.5.

4.2.2. Dimensionless profiles

Boundary layer profiles have been extracted at different time instants for the three measurements locations along the nozzle. In order to improve the comparison between different experiments and to compare

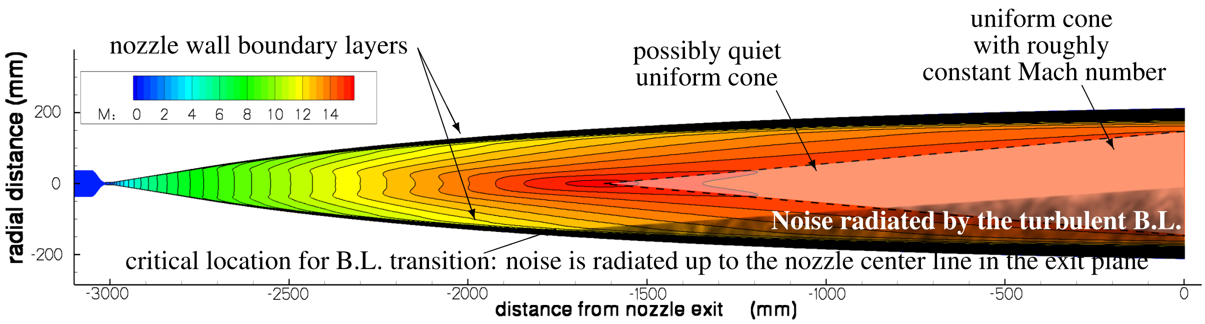

Figure 10: CFD prediction of Mach number in the nozzle and sound radiation by the boundary layers

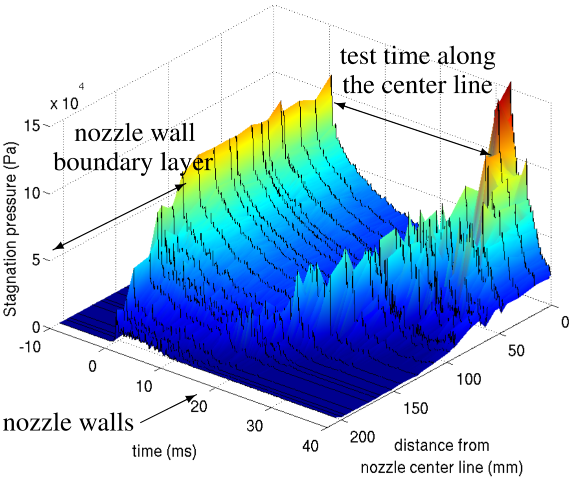

Figure 11: Stagnation pressure profile as a function of time at the nozzle exit for experiments at "Low" Reynolds (using N_2)

profiles considered at different time instants, the stagnation pressure p_{t_2} profiles have been normalized. A local reference stagnation pressure belonging to the boundary layer profile was preferred to the reservoir stagnation pressure located upstream. The location chosen along the profile is in such a way that all the experiments used had one sensor at that position. Precise locations are $r = 91$ mm, $r = 90$ mm and $r = 59$ mm, respectively for profiles at $x = 0$ mm, $x = -750$ mm and $x = -1500$ mm. The results are presented in Fig. 12 for the three locations along the nozzle. For each of these pictures, several boundary layer profiles (in color) are plotted at different time instants. The mean value of these profiles is plotted with a thicker plain black line. The time considered is limited to the beginning of the experiment up to 12 ms when the jet starts closing itself at the nozzle exit and pollutes measurements close to the wall.

The measurements at the nozzle exit show a thick boundary layer with some larger disturbances in the profiles at $r \approx 155$ mm and a lower pressure close to the nozzle center line. Larger pressures are recorded in the wall vicinity where the closest probing location was at $d = 9.5$ mm. Shock waves from Schlieren flow visualization (Fig. 5b) were still observed at that location hence the flow is still supersonic. However, the generated shock and the probe itself may locally disturb the boundary layer and change the flow topology. This is the reason for the larger stagnation pressure for the closest wall measurement.

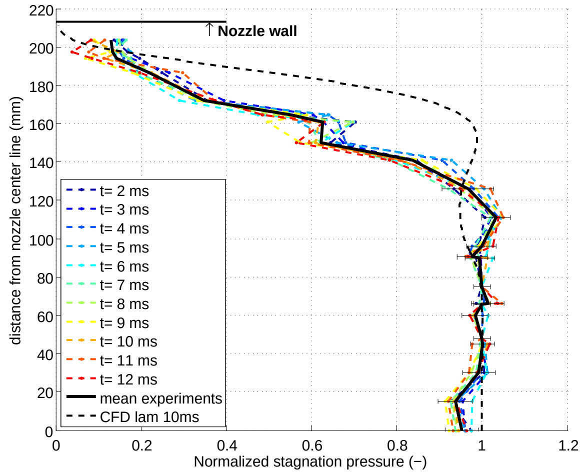

(a) at the nozzle exit

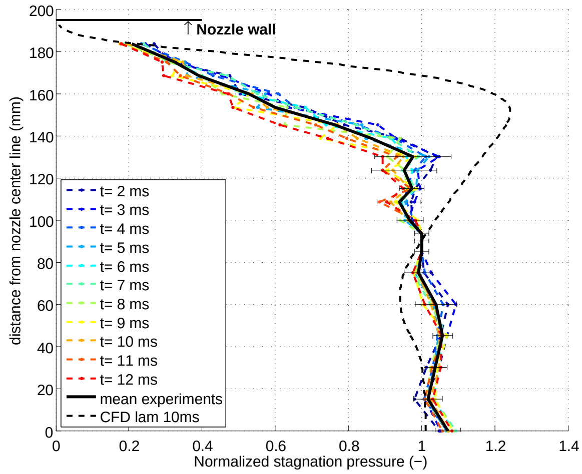

(b) at 750mm inside the nozzle

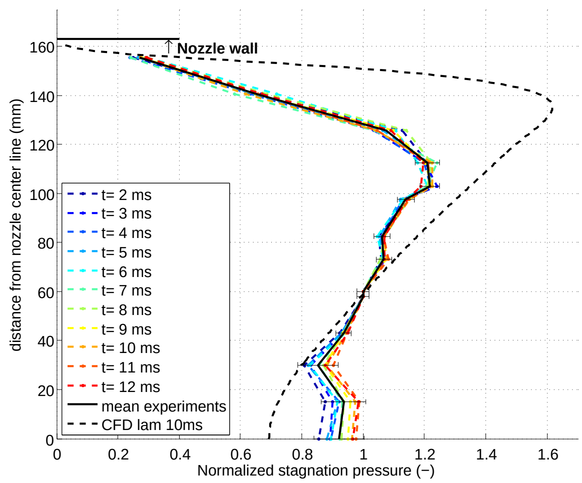

(c) at 1500mm inside the nozzle

Figure 12: Normalized stagnation pressure profiles across the boundary layer

The free-stream Reynolds number is decreasing during an experiment and the boundary layer thickness along the nozzle walls was thus expected to increase. This is not observed clearly in Fig. 12a where boundary layer profiles are well superimposed, showing a similar boundary layer state and a similar boundary layer thickness.

Inside the nozzle, at $x = 750\,\text{mm}$ (Fig. 12b), the recorded stagnation pressure profile is still relatively flat in the center part with relatively thick boundary layers.

Further inside the nozzle, at $x = 1500\,\text{mm}$ (Fig. 12c), the shape of the profile is seen to be very different from the previous ones with a larger peak at the edge of the boundary layer and decreasing towards the nozzle axis. These profiles are very well superimposed and suffer from much lower disturbances except along the nozzle center line. This might be due to a changing flow topology better illustrated by Fig. 13 where boundary layer profiles have been considered for a much longer time before the end of the test time at that location. A flattening of the profiles is clearly observed but its precise origin is not yet known.

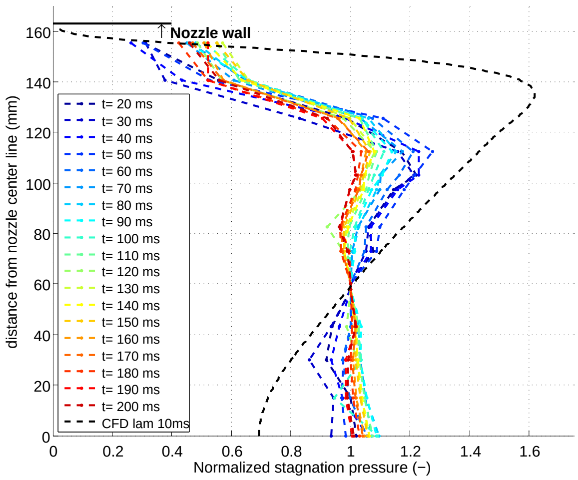

Figure 13: Unsteady normalized stagnation pressure profile at $x = -1500\,\text{mm}$

Mean profiles obtained after normalization have been converted back to a stagnation pressure using the reference stagnation pressure p_{t_2} measured at $t = 10\,\text{ms}$ and plotted in Fig. 14. The nozzle is composed of several sections assembled together with smoothed joints. If these were introducing disturbances into the flow, perturbations could be tracked from one location to another. Characteristic lines are represented here for Mach 12 following the uncertainties shown in section 3.3. The exit profile exhibits a strong disturbance close to the wall. Visual inspection of the nozzle has not revealed either steps or gaps at these locations. Disturbances occurring close to the center line can be followed by analyzing the profiles at successive locations. Disturbances along the center line at $x = -750\,\text{mm}$ may be followed up to the nozzle exit plane but intermediate measurements would be required for definitive conclusions.

4.2.3. Comparison with CFD results

A stagnation pressure profile issuing from CFD results is also given for comparison in each plot of Fig. 12. These laminar steady computations were performed with Longshot free-stream conditions corresponding to $t = 10\,\text{ms}$ ($p_0 = 5.84 \times 10^7\,\text{Pa}$, $T_0 = 1800\,\text{K}$) and using a perfect gas law to describe the gas behavior.

The stagnation pressure (determined from Eq. 1) is normalized using the local value at the same locations as used for experimental results (see section 4.2.2).

$$p_{t_2} = p_\infty \left[\frac{(\gamma+1)\,M_\infty^2}{2}\right]^{\frac{\gamma}{\gamma-1}} \left[\frac{\gamma+1}{2\gamma M_\infty^2 - (\gamma-1)}\right]^{\frac{1}{\gamma-1}} \quad (1)$$

At $x = 0$, $-750\,\text{mm}$ and $-1500\,\text{mm}$, the predicted stagnation pressures p_{t_2} are respectively 28315 Pa, 28440 Pa and 32203 Pa. The measurements at the same locations previously lead respectively to 35730 Pa (+ 21%), 39220 Pa (+ 27%) and 42150 Pa (+ 24%). Moreover, even normalized, the shape of the profile appears to be very different from the ones measured experimentally. The reason is a different boundary layer state which likely was turbulent in the experiments due to the long nozzle used. The apparent fuller profiles of laminar boundary layers have already been reported at lower Mach numbers in [17; 18] and may explain the present mismatch of stagnation pressure p_{t_2} profiles.

Additional computations performed with a more accurate equation of state and turbulent boundary layers will improve the comparison.

4.2.4. Available test time

The time of arrival of the test gas in the nozzle depends on the location considered. Along the center line, the test gas arrives at $t = 0.62\,\text{ms}$, $0.95\,\text{ms}$ and $1.3\,\text{ms}$, respectively for $x = -1500$, $x = -750$ and $x = 0\,\text{mm}$.

The larger stagnation pressure observed by the end of the test time in Fig. 11 is due to the closure of the

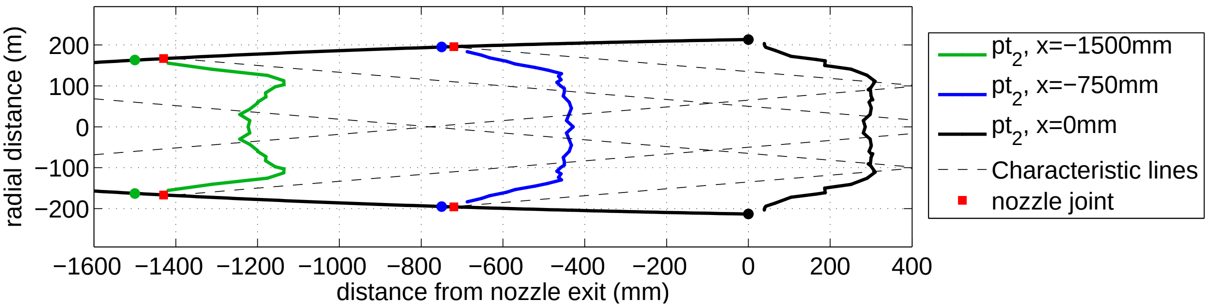

Figure 14: Boundary layer profiles through the nozzle with characteristic lines at Mach 12

hypersonic jet. The time at which it occurs is a function of both r and x. The values reported here are in agreement with other values measured previously at the exit and at $x = 250$ mm (dashed lines). The local closure time is plotted in Fig. 15. It appears clearly that the test times available are much longer inside the nozzle. Thus, for future transition measurements on models, it is suggested to use long geometries partially located inside the nozzle. This will allow to reach large local Reynolds numbers required for boundary layer transition and will avoid the short test time at the exit due to the early jet closure.

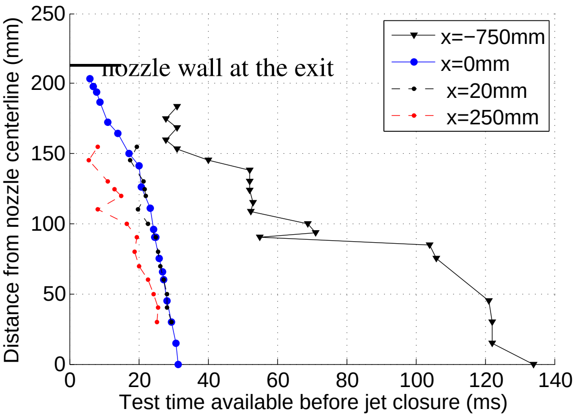

Figure 15: Jet closure time for various locations along the nozzle

4.2.5. *Free-stream noise levels*

The flow of most hypersonic facilities is seeded by high-velocity particles issuing from various upstream elements. This usually prevents the use of sensors directly exposed to the flow and reduces hopes for a complete description of the flow noise levels of hypersonic facilities. Nevertheless, a first approximation of the free-stream noise levels can be obtained by analyzing pitot pressure measurements and their fluctuations.

A pressure coefficient can be expressed at each measurement location according to the classical definition:

$$C_p = \frac{p - p_\infty}{\frac{1}{2}\rho_\infty u_\infty^2} \tag{2}$$

which in the hypersonic limit, using N_2, and for stagnation points reduces to $C_p = 1.839$.

Neglecting the low free-stream pressure when compared to the pitot pressure, Eq. 2 can be rewritten as $p_{t_2} = \frac{1.839}{2}\rho_\infty u_\infty^2$. Then, neglecting density fluctuations (although they may be important, no probe could differentiate them during the present measurements) and second order terms, the velocity fluctuations can be linked to the pressure fluctuations through Eq. 3.

$$u'_\infty = \frac{p'_{t_2}}{1.839\,\rho_\infty u_\infty} \tag{3}$$

The RMS of the pitot pressure signal was considered over 0.2 ms windows, with a 50% overlap. The local velocity fluctuations have then been non-dimensionalized with the mean free-stream velocity along the center line at that time instant. Results are shown in Fig. 16 in terms of u'/u_∞. As one expects, the largest levels of disturbances are recorded within the turbulent boundary layer (up to 20-25% in the outer part of the nozzle boundary layer). This turbulent motion of eddies into the boundary layer radiates noise into the free-stream and leads to noise levels measured about $3.8\% \pm 1.1\%$. The influence of the normal shock wave in front of the sensor is likely to increase the noise levels according to the numerical work of [19]. Despite this amplification, the noise levels in the free-stream would remain 2 to 3 orders of magnitude larger than what they are in real flight conditions. Therefore, the Longshot facility is a conventional ”noisy” hypersonic wind tunnel and transition experiments will strongly be influenced as shown in Fig. 1.

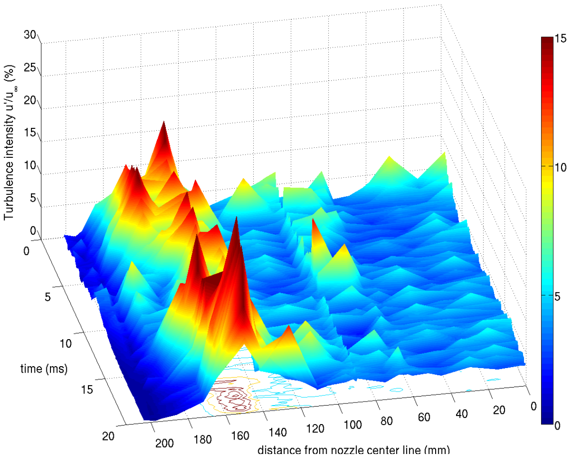

Figure 16: Turbulence intensities at the nozzle exit

4.2.6. Measurements further inside the nozzle

The boundary layer profiles measured are believed to be turbulent even at $x = -1500$ mm when compared to CFD predictions although pitot pressure fluctuations are much lower inside the nozzle (Fig. 12c). Measurements further inside the nozzle with the rake are not possible with the sensors currently used and rake support vibrations would become an issue. The instrumentation of the walls of the nozzle should be considered as an interesting workaround to detect the transition location closer to the throat of the nozzle. Temperature measurements are suggested since thermocouples sensors are more robust and not subject to nozzle vibrations as would be pressure sensors.

5. Flow visualization

In order to support the current flow investigation and identify possible sources of non-isentropic flow phenomena, a flow visualization has been conducted in the test section of the facility. It is known for decades that during an experiment, a brief bright light is observed in the test section although nothing is known about its source, nature nor even its duration and precise location. The first direct flow visualization is reported hereafter. A Phantom v.7 high-speed camera was used to record frames as the ones presented in Fig. 17 at 4796 fps with an exposure time of 195 μs in a complete darkness environment.

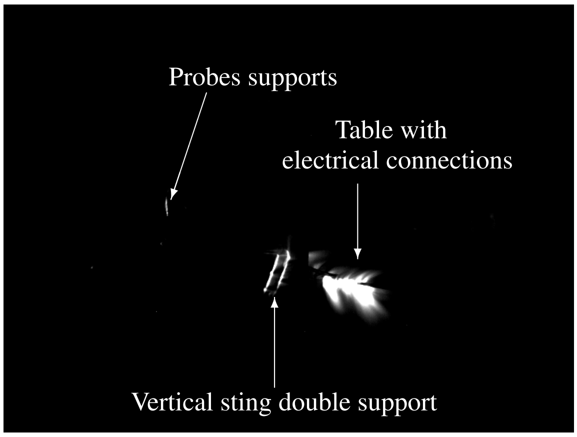

(a) Excited gas at stagnation point of probes and supports, $t = 0.5$ ms

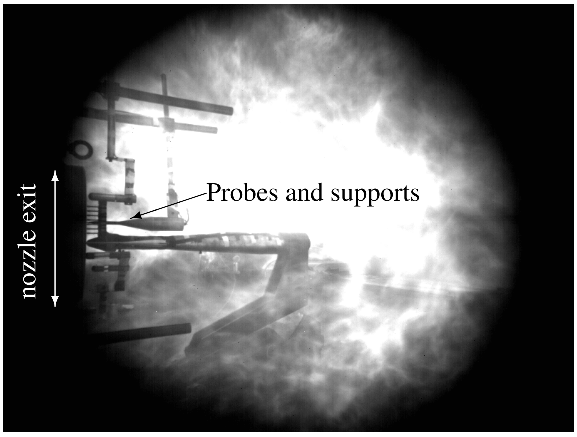

(b) Identical view angle, diffuse light around the hypersonic jet, $t = 27$ ms

Figure 17: Light emission from the Longshot facility captured by a high-speed camera using a wide-angle objective

Two clearly distinct phenomena are distinguished. At first, a bright flow is observed around the stagnation point of probes and supports following the shape of the shock waves around these bodies. These are identified as real gas effects with excitation of N_2. This lasts only for a brief period about 1 ms during which the high enthalpy test gas can be tracked successively from the stagnation probes at the nozzle exit towards the end of the dump tank where a bright light is observed as similarly mentioned in [20].

Secondly, a different and even brighter feature slowly appears before gradually fading away (Fig 17b). It appears about $t \approx 4$ ms while the initial test gas has reached the end of the test chamber and starts to recirculate around the hypersonic jet. This correlates well well with the rise of static pressure beside the jet at $t \approx 4$ ms. The diffuse light is observed all around the high velocity jet without having a clearly defined structure and lasts for 25 to 30 ms. The jet itself does not appear to be bright with an apparent shear layer on some frames. It has been recorded for many successive experiments using different points of view, and even shorter exposure times. Whether this light has an influence on the measurements remains to be evaluated. The possible excitation/deexcitation of the test gas by high velocity seeding particles should also be investigated.

Despite various spectroscopy measurements using an intensified camera and optical fibers pointing across the jet, on stagnation probes, at the back of the test section, along the jet boundaries and in the test section, no significant measurement could be obtained and no conclusion drawn regarding the frequency content of the emitted light. Thus, additional experiments are required to identify the precise nature of these features.

6. Conclusions

The static pressure probe has been significantly improved and the influence of the inlet tapered holes on the higher measured static pressure has been ruled out. The influence of the viscous effects on the probe remains unknown and will be the purpose of a coming test campaign. The different behavior of the decaying trend for the measured static pressure between early and end of an experiment also requires additional experiment to explain the rising trend observed for the free-stream Mach numbers. The lower Mach numbers deduced from these measurements could be explained by a non-isentropic flow expansion although it requires deeper analysis of the possible flow phenomena.

Nozzle boundary layers have been characterized at three locations along the nozzle. Comparison with laminar CFD shows a poor agreement, depicting a likely turbulent boundary layer even at $x = -1500$ mm into the nozzle. The precise location where transition to turbulence occurs in the nozzle has not yet been determined but, in the present configuration, the Longshot facility is unlikely providing a quiet core even for this "Low" Reynolds number condition. Turbulent CFD results should support the present conclusions.

Advantages of using long models fitted into the nozzle have been reported in order to benefit from larger local Reynolds numbers and avoid early jet closure.

The noise levels measured at the nozzle exit are about 3.8% in the uniform part of the hypersonic jet which confirms the Longshot facility is effectively a conventional "noisy" facility not directly representative of flight conditions. The source of these large levels is due to the turbulent boundary layers along the nozzle walls where much larger fluctuations have been recorded.

The emission of light into the test section has been observed for the entire test duration and is partially issuing from an initial excited test gas visible at the stagnation point of all probes. It is then followed by a much longer diffuse but still bright light source which might be due to test gas excitation by seeding particles.

The present results are providing a better knowledge of the flow in the hypersonic contoured nozzle of the Longshot facility which can already be used for boundary layer transition experiments. From the analysis of the present results, new unknowns are also rising such as possible non-isentropic flow phenomena, unsteady boundary layers inside the nozzle or the origin of the light emission in the test section. These all require to be the object of subsequent investigations within the facility.

Acknowledgments

I gratefully acknowledge FRIA (Fonds pour la formation à la Recherche dans l'Industrie et dans l'Agriculture) for the financial support of this project. I am also thankful to K. Bensassi and D. Le Quang for their respective help in providing CFD results and support for the application of spectroscopy techniques.

References

[1] J. Laufer, Sound radiation from a turbulent boundary layer, Technical Report TR-32-119, Jet Propulsion Laboratory, California Institute of Technology, Pasadena, California (November 1961).

[2] J. Laufer, Some statistical properties of the pressure field radiated by a turbulent boundary, Physics of Fluids 7 (8) (1964) 1191–1197.

[3] S. P. Schneider, Development of hypersonic quiet tunnels, Journal of Spacecraft and Rockets 45 (4) (2008) 641–664.

[4] S. P. Schneider, Effects of high-speed tunnel noise on laminar-turbulent transition, Journal of Spacecraft and Rockets 38 (3) (2001) 323–333.

[5] S. R. Pate, C. J. Schueler, Radiated aerodynamic noise effects on boundary layer transition in supersonic and hypersonic wind tunnels, AIAA Journal 7 (3) (1969) 450–457.

[6] S. R. Pate, Effects of wind-tunnel disturbances on boundary-layer transition with emphasis on radiated noise: a review, in: AIAA (Ed.), 11th Aerodynamic testing conference, no. 80-0431, 1980.

[7] J. M. Kendall Jr., Supersonic boundary-layer transition studies, in: JPL Space Programs Summary, Vol. 3, Jet Propulsion Laboratory, 1970, pp. 43–47.

[8] E. Reshotko, Boundary layer stability and transition, Annual Review of Fluid Mechanics 8 (1976) 311–349.

[9] B. Van Hove, Free stream measurements and related data reduction methods for the Longshot hypersonic wind tunnel, Project report 2011-31, von Karman Institute (June 2011).

[10] H. Olivier, H. Kindl, Development of a static pressure probe (progress report), Tech. Rep. HT-PR-E34-711-RWTH, Shock Wave Laboratory RWTH Aachen (December 1995).

[11] A. H. Boudreau, Characterization of hypersonic wind tunnel flow fields for improved data accuracy, in: AGARD-CP-429, AGARD, 1987.

[12] A. H. Boudreau, Methodology of hypersonic testing, in: von Karman Institute (Ed.), Lecture Series, no. LS 1993-03, 1993.

[13] P. D. Arthur, Effects of impurities on the supersaturation of nitrogen in a hypersonic wind tunnel, Ph. d. thesis, Calif. Inst. of Technol., Pasadena, California (1952).

[14] P. P. Wegener, L. M. Mack, Condensation in supersonic and hypersonic wind tunnels, in: H. L. Dryden, T. von Kármán (Eds.), Advances in applied mechanics, Vol. 5, Academic Press Inc., 1958, Ch. 7, Condensation in supersonic and hypersonic wind tunnels, pp. 307–447.

[15] H. G. Stever, Condensation phenomena in high speed flows, in: Fundamental of Gas Dynamics, Princeton University Press, 1958, Ch. F, pp. 526–573.

[16] M. Lederer, W. Yanta, W. Ragsdale, S. Hudson, W. Griffith, Condensation in hypersonic nitrogen wind tunnels, in: AIAA 16th aerodynamic ground testing conference, no. 1990-1392, Seattle, WA, 1990.

[17] P. C. Stainback, J. B. Anders, W. D. Harvey, A. M. Cary, J. Harris, An investigation of boundary layer transition on the wall of a Mach 5 nozzle, in: AIAA 12th Aerospace and Sciences meeting, no. 1974-136, 1974.

[18] W. D. Harvey, P. C. Stainback, J. B. Anders, A. M. Cary, Nozzle wall boundary layer transition and free-stream disturbances at Mach 5, AIAA Journal 13 (3) (1975) 307–314.

[19] H. S. Ribner, Spectra of noise and amplified turbulence emanating from shock-turbulence interaction, AIAA Journal 25 (3) (1987) 436–442.

[20] T. J. McIntyre, H. Kleine, A. F. P. Houwing, Optical imaging techniques for hypersonic impulse facilities, The Aeronautical Journal 111 (2007) 1–16.

Trajectory and Atmospheric Reconstruction for Entry Vehicles

Bart Van Hove

Royal Observatory of Belgium, Reference Systems and Geodynamics, Belgium, bartvh@observatoire.be

Supervisor: Chazot Olivier

Associate Professor, Aeronautics and Aerospace department, von Karman Institute for Fluid Dynamics, Belgium, chazot@vki.ac.be

University Supervisor: Lacor Chris

Full Professor, Department of Mechanical Engineering, Vrije Universiteit Brussel, Belgium, Chris.Lacor@vub.ac.be

University Co-Supervisor: Özgür Karatekin

Royal Observatory of Belgium, Reference Systems and Geodynamics, Belgium, ozgur.karatekin@oma.be

Abstract

Reconstruction of the hypersonic entry of planetary capsules has mainly focused on engineering trajectories (position/velocity). However, development of sophisticated on-board experiments and demand for in-situ atmospheric profiles by the climate modeling community, require accurate atmospheric conditions.

Keywords: trajectory, atmosphere, reconstruction, FADS, flow characterization, uncertainty quantification.

1. Introduction

Reconstruction of the hypersonic entry of planetary capsules has mainly focused on the engineering trajectory (position, velocity). The interpretation of accurate on-board experiments (e.g. EXPERT) and a demand for in-situ atmospheric profiles by the planetary climate modeling community, require accurate reconstruction of also the atmospheric conditions. Currently, this is typically limited to +/-15% [ref 1]. Atmospheric profiles from hypersonic entry are especially interesting on planets where in-situ measurements are scarce, such as Mars [ref 2].

Figure 1 is a simplified representation of the reconstruction process. The set of available measurements almost always includes accelerometers; sometimes also gyroscopes, nose surface pressures (for use in a Flush Air Data System) and Doppler shifts in the radio link signal are included. Additional information going into the reconstruction can include an aerodynamic database built from CFD simulations or wind tunnel experiments, a planetary gravity model and even uncertainty estimates of the above (including the measurements). This additional information

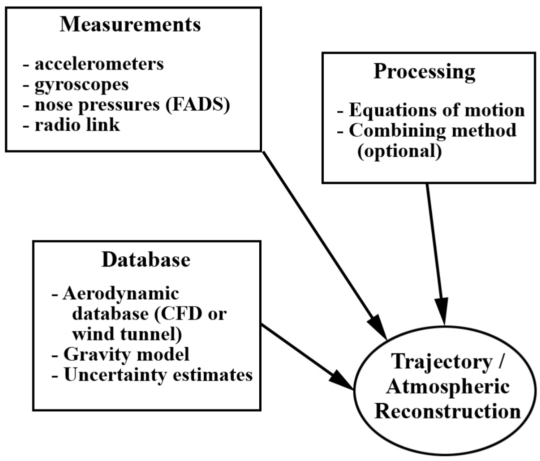

Figure 1: Simplified reconstruction process

is listed under the catch-all term 'database' indicating prior knowledge. A sophisticated, accurate database is preferable to a very simple set of assumptions. Finally, the processing consists of the integration of equations of motion and optionally some method to combine multiple measurements. These range from simple comparative calculations to stochastical Kalman filters that produce weighted averages based on uncertainty estimates in the database. Such a filter also produces uncertainty estimates on the results.

2. Approach

We will investigate several of the above elements to determine which are crucial to the atmospheric reconstruction effort. Resulting atmospheric profiles can be compared to each other and climate models. Available datasets include ARD on Earth, Phoenix, Pathfinder, MER on Mars and Huygens on Titan. NASA's Mars Science Laboratory (MSL) will land in August 2012. MSL is the best equipped Mars entry vehicle to date, including nose pressures for FADS and heat flux measurements.

Currently, we use the Phoenix dataset as a test case for estimating atmospheric reconstruction accuracy and sensitivity to measurements and database elements. The result will be a versatile reconstruction code including simple uncertainty quantification (UQ) analysis. We can incorporate existing work such as the VKI 6-DOF trajectory code, the Royal Observatory's radio Doppler code and a publically available Inertial Measurement Unit reconstruction code [1].

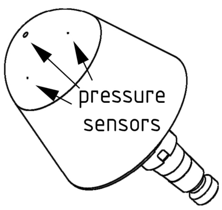

Figure 2: FADS sensors on wind tunnel probe

MSL will be the first opportunity to use a FADS system on Mars for separating aerodynamic and atmospheric uncertainties. Reconstruction code using the pressure measurements has been developed at NASA Langley [2]. At VKI we are currently building the basic FADS expertise, as well as investigating the incorporation of state-of-the-art UQ methods and heat flux measurements to improve FADS accuracy. In broad strokes, this consists of CFD simulations with associated UQ, carried out by the team of T. Magin, and wind tunnel testing (Figure 2) with associated flow characterization by the team of O. Chazot, including the PhD candidate. Specifically, we are developing a static pressure probe (Figure 3) to more accurately determine the Longshot flow conditions.

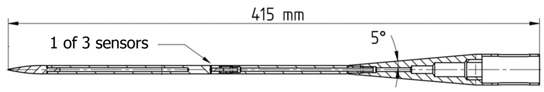

Figure 3: Nagamatsu hypersonic static pressure probe

We will use the Phoenix dataset and the reconstruction tool to produce synthetic datasets for a hypothetical FADS system, and similarly for the MSL dataset when it becomes available in August 2012. The objective is to identify design and processing features that constrain or benefit the accurate calculation of atmospheric profiles such as the free stream density. Inverse problem UQ and wind tunnel results should quantify the state-of-the-art accuracy and point out methodologies for improvement.

3. Conclusion

Reconstruction of atmospheric conditions (i.e. static pressure and density) during hypersonic entry has received little attention compared to reconstruction of the basic trajectory. More accurate atmospheric conditions have direct applications to lifting-entry vehicle control, interpretation of in-flight experiments and climate modeling (especially on non-Earth planets such as Mars). Our aim is to improve that accuracy with a comprehensive approach including CFD, wind tunnel testing, UQ tools and various processing techniques depending on the available sensor information.

Acknowledgments

Candidate supported by Royal Observatory of Belgium (ROB), collaboration with VKI who are involved in projects to improve the accuracy of Flush Air Data Systems.

References

[1] P. Withers, M. C. Towner, B. Hathi and J. C. Zarnecki, Analysis of entry accelerometer data: A case study of Mars Pathfinder, Journal of Planetary and Space Science 51 (1) (2003) 541–561.

[2] S. Dutta and R. D. Braun, Mars Entry, Descent and Landing Trajectory and Atmosphere Reconstruction, Ph.D. thesis, Guggenheim School of Aerospace Engineering, Georgia Institute of Technology (2010).

Development of Advanced Hypersonics Models for Transition to Turbulence: Uncertainty Quantification for Transition Prediction

Gennaro Serino

Aeronautics and Aerospace Department, von Karman Institute for Fluid Dynamics, Belgium, gennaro.serino@vki.ac.be

Supervisors: Thierry Magin♣ & Patrick Rambaud♠

♣*Assistant Professor* & ♠*Associate Professor, Aeronautics and Aerospace Department, von Karman Institute for Fluid Dynamics, Belgium, magin@vki.ac.be., rambaud@vki.ac.be*

University Supervisor: Vincent E. Terrapon

Professor, Aerospace and Mechanical Engineering Department, Université de Liège, Belgium, vincent.terrapon@ulg.ac.be.

Abstract

Transition has a crucial role in hypersonic applications. During an atmospheric reentry, transition increases the aerodynamic heating of the space vehicle thus compromising the integrity of the heat shield.
A new method for transition prediction is proposed by using Uncertainty Quantification (UQ) in numerical simulations. UQ aims at simulating a system by taking into account all the uncertainties due to its physical variability and to the hypothesis used in the mathematical models.
Preliminary results on a Mach 6 flat plate shows good agreement with experimental transition location detected via the heat flux distribution.

Keywords: Laminar to turbulent transition, Hypersonic, Uncertainty Quantification (UQ), Computational Fluid Dynamics (CFD)

1. Introduction

Simulations of aerospace applications are challenging problems involving many complex physical phenomena ; for instance, predicting the response of thermal protection materials to extreme reentry conditions involve flow transition from laminar to turbulent and aerothermochemistry. Reliable predictions of such complex systems require sophisticated mathematical models to represent the physics and phenomena such as transition. A systematic and comprehensive validation, including the quantification of uncertainties inherent in such models, is required.
Conventionally, engineers resort to safety factors to account for uncertainty parameters and to determine the quantities of interest, such as the heat shield thickness. These factors allow to avoid space mission failure and ensure safety of the astronauts and payload, but this is at the expense of reduced mass of embarked payload. Uncertainty Quantification (UQ) is a systematic approach to establish “error bars“ on quantities of interest, such as the heat flux, yielding to the design of the heat shield with more confidence. At the interface of physics, mathematics and statistics, UQ tools are still in constant development in computational science. These tools aim at developing rigorous methods to characterize the impact of “limited knowledge“ on the quantities of interest.
We propose to develop a UQ methodology to study transition from laminar to turbulent in hypersonic flows. Moreover, the methodology that we propose to develop will be general and can be applied to many other research topics such as flow transition in turbo machinery.

2. Objectives

The project general goal is to propose a new approach in transition prediction. In order to achieve this goal, it will be necessary to also improve our understanding of transition mechanisms in hypersonic flows. A variety of tools will be used to model turbulence (DNS, RANS, e^N, PSE) and coupled with UQ in order to yield a reduced model suitable for engineering applications. All uncertainties and errors will be taken into account in order to define the design margins for space vehicles. The uncertainties will comprise the free stream conditions (Mach number, pressure, temperature, turbulence intensity), surface parameters (roughness element height), transition model parameters and wall chemistry models, in order to investigate a wide range of cases including natural and bypass transition.

3. State of the art

One of the most critical tasks in the design of space vehicle is the prediction of transition from laminar to turbulent flow. Transition depends on several parameters and, in particular, it is promoted by the presence of surface unevenness as roughness, steps, gaps and ramps (Fig.1). A sound transition model valid in the hypersonic regime is still lacking.

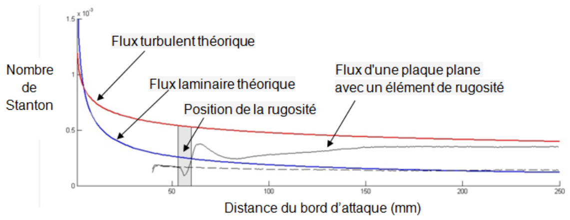

Figure 1: Theoretical(blue and red lines)-experimental(black line) comparison of the heat flux on a flat plate with a ramp roughness element (P_0 = 31 Bar, T_0 = 500 K, M = 6) [29].

Experimental investigations in hypersonics are quite expensive and they can be only be performed in short times and for limited operating conditions. CFD allows to simulate a wide range of conditions even if there are difficulties to model and predict transition at high Mach number. Models include Wilcox's procedure to use the low-Reynolds number $k - \epsilon$ model, reported in [4], as a transition region model where a roughness strip is used to fix the transition point. Schmidt and Patankar's production term modifications for low-Reynolds number $k - \epsilon$ models is an attempt to solve the problems these models have in simulating the transition region. Moreover, Warren, Harris and Hassan [5] developed a one equation turbulence model that accounts for the first and second mode disturbances in the transition region. Other models that can be considered include the algebraic transition region model of ONERA/CERT and the linear combination model of Dey and Narashima [6]. An interesting approach is the eddy viscosity-intermittency transition model $(R - \gamma)$ which is based on the work of Ryong Cho and Kyoon Chung [7]. The model exploits the transport equation for the eddy viscosity (R) of Goldberg's one-equation turbulence model reported in [8] that is similar in form to the model of Spalart-Allmaras shown in [9]. The model was applied in [10] by the author for roughness induced transition prediction in hypersonic flows. The model was able to correctly predict the onset of transition even though all the physical processes (vortices and flow topology) were not completely reproduced.
In conclusion, these methods fail because of 3 reasons: conditions vary for each particular mission, random nature of transition (uncertainty in free stream turbulence, surface unevenness), simple models do not reflect all the physical processes. UQ is the strategy which aims to investigate the effects of those uncertainties in numerical simulations with a probabilistic approach.

4. Scientific strategy

4.1. Role of Uncertainty Quantification in predictive simulation

UQ allows to simulate a system by taking into account all uncertainties regarding the boundary, initial conditions and the model parameters.
All the uncertainties are modeled with a distribution which resembles the expected behavior of the considered variable. Each distribution is then modulated with a transfer function to obtain the output quantity of interest. We will calculate how the quantities of interest are influenced when the random variables describing the sources of uncertainties take different values. We therefore study how the uncertainties "propagate" through the simulations.
The most common approaches in propagation are the Monte Carlo method and the polynomial chaos method [12]. With respect to conventional sensitivity approaches, UQ offers the possibility to take into account the effect of statistical distributions in numerical simulations.

4.2. Methodology

The novelty of the approach consists in using UQ in numerical transition prediction. Simulations will be carried out with a case-dependent random parameter which, for instance, will mimic the uncertainty of the disturbance spectrum. The probabilistic distributions as well as the range of variations of the variables will be based on experimental data. Once these parameters will be selected, numerical simulations will be performed and a quantity of interest will be computed to evaluate the effects of the parameters. This quantity can be the stream wise location of increase in skin friction or in heat transfer, which may be regarded as representative of the transition location. Several independent simulations will be performed in order to use, for example, a Monte-Carlo sampling to build the response approximately, as an interpolant of a response surface (the collocation points), using a Lagrange polynomial. Several research codes developed at the VKI will be used in the proposed research.

- Simulations will be carried out with a Reynolds Average Navier Stokes (hereafter RANS) and a Linear Stability Theory (hereafter LST) codes. UQ on LST codes [24] will be used to investigate the onset of transition. UQ on RANS codes will be used to determine both the onset of transition and the successive turbulent flow. Turbulence models based on different transport equations will be used in order to obtain different transfer functions. This will contribute to complete the lack of knowledge derived by using such approximations and to reduce the uncertainties due to the models.

- Direct Numerical Simulations (DNS) will be used to investigate some interesting cases highlighted with the RANS/LST simulations. For instance, RANS models predict transition by switching the solution from laminar to turbulent flow. Experimental results showed that, when transition occurs, the skin friction and the heat flux distribution are characterized by an overshoot immediately following its onset (Fig.1). RANS models are not capable of reproducing such an overshoot so that a further investigation is necessary by performing DNS on limited zone of interest with the codes mentioned in [20] and [21].

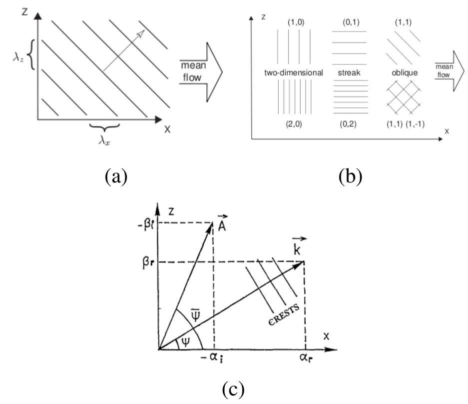

Figure 2: (a)Wave propagating in the mean flow with streamwise wave number λ_x and spanwise wave number λ_z, (b)Examples of notation for wave disturbances[13], (c) Notation for the oblique waves

- The strategy and the conclusions derived by test cases will be used for the final validation case and for the eventually application of the inverse problem. This will be the EXPERT re-entry vehicle configuration. A wide experimental database based on wind tunnel tests is available which will give important contribution to investigate real flight conditions with the proposed methodology.

5. Application

The methodology is currently applied in transition prediction for the oblique breakdown mechanism occurring in supersonic boundary layers. In this case, the LST code VESTA, developed at the VKI by Pinna [24], is used to compute the linear amplification of oblique waves on a Mach 6 flat plate. The code is used to compute the N factor for the e^N transition prediction method in order to detect the transition location on the flat plate to be compared with experimental data. The linear stability is coupled with the UQ which consists in assigning an uncertain spectrum, that is a probability density function (pdf), to the frequency and to the propagation angle of the oblique waves traveling inside the domain(Fig. 2).

Then, the quantity of interest, that is the N factor, is computed at each location as a 2D function dependent on both the frequency and the wave angle. Results of the LST are then sampled by using a Monte Carlo method to compute the main statistical moments of the quantity of interest. The criterion for transition is the N factor experimentally determined in the facility where the test has been carried out. Finally, the probability of transition is computed at each station on the flat plate as the probability of having the computed N factor exceeding the threshold value given by experimental results as represented in Fig.3.

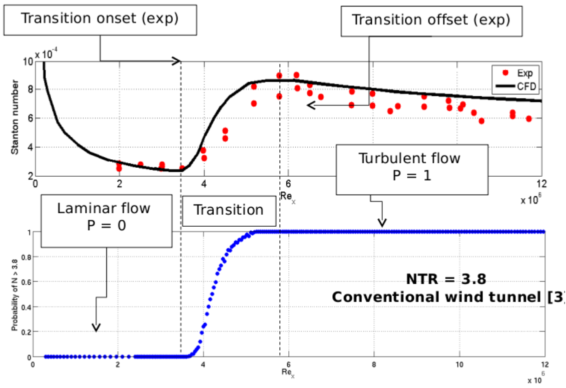

Figure 3: Comparison between experimental data (red dots), RANS solver (black line) and probability of transition (blue dots) for the Mach 6 flat plate test case in [27]

6. Conclusions

A probabilistic transition prediction methodology is proposed by combining numerical simulations and Uncertainty Quantification. Results on test case concerning a hypersonic flat plate demonstrates the agreement with experiments in terms of transition onset location. Good agreement was achieved on the transition point but the prediction of transition offset occurs slightly before experimental value thus the numerical transition length is shorter than in the experiments. Comparison is made between the probability of transition (N-factor greater than the threshold value for transition) and the experimental/computed heat flux distribution. It is possible to infer a parallel between the computed probability and the intermittency since the range of variability is the same [0,1] and also the physical meaning, since the intermittency is defined as the turbulent-laminar time ratio. Further investigation will involve a second test case on a 5° sharp and blunt cone. Preliminary results are promising and it will be interesting to determine in future work the impact of the methodology on simulations of higher complexity as RANS, with transitional models, and DNS.

Acknowledgments

The author gratefully acknowledges the “Fonds de la Recherche Scientifique” for the FRIA fellowship which is financing the current doctoral research.

References

[1] H. Schlichting, Boundary Layer Theory, Springer, 1995.
[2] Anderson J.D., Hypersonic and High Temperature Gas Dynamics, AIAA, 1986.
[3] R.D. McDaniel, R.P. Nance and H.A. Hassan, Transition Onset Prediction for High-Speed Flow, Journal of Spacecraft and Rockets, vol. 37 n3, 2000.
[4] Wilcox David C., Turbulence Modeling for CFD, DCW Industries, 1993.
[5] Warren E., Harris J. and Hassan H., A Transitional Model for High Speed Flow, AIAA-94-1851-CP, 1994.
[6] Narashima R., The Laminar Turbulent Transition Zone in the Boundary Layer, Progress in Aerospace Science,vol.22, pages 29-82, January 1985.
[7] Ryong Cho Ji, Kyoon Chung M., A $k-\epsilon$ Equation Turbulence Model, Journal of Fluid Mechanics, vol.237, pages 301-322, 1992.
[8] Goldberg U., Turbulence Closure with a Topography-Parameter-Free Single Equation Model, International Journal of Computational Fluid Dynamics, vol. 17. pages 27-38, 2003.
[9] Spalart,P.R., Allmaras,S.R., A one equation turbulence model for aerodynamic flows, American Institite of Aeronautics and Astronautics (AIAA), vol. 92-0439, 1992.
[10] Serino G., Numerical prediction of transition in hypersonic flow, von Karman Institute for Fluid Dynamics, DC report 2011.
[11] Malik, M. R., Hypersonic flight transition data analysis using parabolized stability equations with chemistry effects, Journal of Spacecraft and Rockets 40 (3), 332, 2003.
[12] G. Iaccarino, T. Chantrasmi, A. Doostan, Towards Uncertainty Quantification in High-Speed Turbulent Flow Simulations, Stanford PSAAP Center - UQ Workshop - July 2008.
[13] Berlin, S., *Oblique Waves in Boundary Layer Transition*, Doctoral Thesis, Stockholm, 1998.
[14] Marco Panesi, Kenji Miki, E. Prudencio, Serge Prudhomme, Quantification of Uncertainty in Hypersonic Flows, RTO-AVT-VKI short course on Uncertainty Quantification, Stanford University, California, 2010.
[15] Ioana Cozmuta, Uncertainty Quantification and Statistical Engineering for Hypersonic Entry Applications, RTO-AVT-VKI short course on Uncertainty Quantification, Stanford, CA, 2011.
[16] Ren Pecnick, Jeroen A.S. Witteveen, and Gianluca Iaccarino, Uncertainty quantification for laminar-turbulent transition prediction in RANS turbomachinery applications, AIAA 2011-660, Orlando, Florida, 49th AIAA Aerospace Sciences Meeting including the New Horizons Forum and Aerospace Exposition 4 - 7 January 2011.
[17] S.C.Tirtey, O.Chazot, L.Walpot, Characterization fo hypersonic roughness-induced boundary-layer transition, PhD Thesis, von Karman Institute for Fluid Dynamics, 2010.
[18] Magin, T. E., A model for inductive plasma wind-tunnels, Ph.D. thesis, von Karman Institute for Fluid Dynamics, Rhode-Saint-Gense, 2004.

[19] Marxen, O., Iaccarino, G. & Shaqfeh, E., Disturbance evolution in a Mach 4.8 boundarylayer with 2-D roughness-induced separation and shock, Journal of Fluid Mechanics, in press, 2009.

[20] Marxen O., Iaccarino G., Shaqfeh S.G., Boundary-layer transition via spatially growing oblique waves, Center for Turbulence Research, Stanford University, Under consideration for publication in Journal of Fluid Mechanics, 2009.

[21] Marxen O., Iaccarino G., Shaqfeh S.G., Uncertainty quantification for linear and weakly non-linear supersonic boundary-layer instability, Center for Turbulence Research, Stanford University, Annual Research Briefs 2009, 2009.

[22] Marxen O., Iaccarino G., Instabilities in supersonic boundary layers in the presence of uncertainty, Center for Turbulence Research, Stanford University, 2009.

[23] Iaccarino G., Magin T., Prudhomme S., Abgrall R., Bijl H., RTO-AVT-VKI Short Course on Uncertainty Quantification, Bruges BE, May 13-14, 2011.

[24] Pinna F., Numerical study of stability and transition of flows from low to high Mach number, von Karman Institute for Fluid Dynamics, Universitá "La Sapienza" di Roma, PhD thesis, 2012.

[25] Arnal D.,Special Course on Progress in Transition Modeling, AGARD report 793, 1993.

[26] Horvath T.J., Berry S.A., Hollis B.R., Chang C.L. and Singer B.A., Boundary layer transition on slender cones in conventional and low disturbance Mach 6 wind tunnels, NASA Langley Research Center, AIAA 2002-2743.

[27] Dilley A.D.,Evaluation of CFD turbulent heating prediction techniques and comparison wit hypersonic experimental data, NASA/CR-2001-210837.

Conjugate Heat Transfer using Large Eddy Simulation in Rib Roughened Cooling Channels

Sebastian Scholl

Turbomachinery and Propulsion Department, von Karman Institute for Fluid Dynamics, Belgium, sebastian.scholl@vki.ac.be

Supervisor: Tom Verstraete

Assistant Professor, Turbomachinery and Propulsion Department, von Karman Institute for Fluid Dynamics, Belgium, tom.verstraete@vki.ac.be.

University Supervisor: Wolfgang Schröder

Professor, RWTH Aachen, Aerodynamisches Institut, office@aia.rwth.de.

Abstract

In this work, computations will be performed to study the flow and the conjugate heat transfer in rib roughened cooling channels of turbine blades. Turbulence will be simulated and modeled via Large Eddy Simulation. The computation will be validated through the comparison with existing experimental data for the cooling channel flow.

Keywords: Conjugate Heat Transfer, Large Eddy Simulation, Gas Turbines, Turbine Blade, Cooling Channels

1. Introduction

The Turbomachinery industry tries to comply with both the claims for environmental awareness and the rising use of energy. Hence, the requirements for performance and efficiency of gas turbines increase. One method to improve the cycle performance of gas turbines is to increase the turbine inlet fluid temperature. Although improvements of the temperature resistance of the materials have been made over the last decades, the turbine inlet temperature exceeds the melting temperature of the material in modern gas turbines (see figure 1). Hence, the turbine blades have to be cooled. Since life of a turbine blade is reduced by half with an increased temperature of 30 Kelvin [2], engineers have to predict the local heat transfer coefficients and temperatures accurately. Furthermore, the pressure drop should be as low as possible and at the same time, the cooling efficiency as high as possible. Therefore, cooling channels are turbulated, for instance by obstacles such as ribs. Thus, the complexity of the flow field increases and it is not possible to predict the wall temperature a priori.

To gain reliable results for efficient thermal design of turbine blade cooling, both the heat conduction in the solid and the convection have to be taken into account simultaneously, which is called a conjugate heat transfer (CHT) problem.

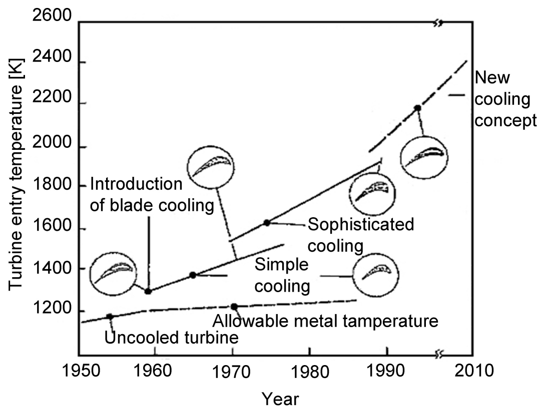

Figure 1: Variation of turbine entry temperature and the allowable metal temperature over several decades[1].

Although CHT is a coupled problem, many studies compute the solid and the flow field separately. It could be shown that this approach does not lead to satisfactory results in comparison with experimental investigations [3]. Besides the attempt to calculate CHT uncoupled, there are mainly two different approaches to solve CHT problems in a coupled manner as described by Verstraete [4] and summarized as follows. The first approach, the conjugate method, computes both the fluid domain and the solid domain at each time step simultaneously. For the conjugate method, one monolithic solver for both fields is used.

However, a major problem in CHT is that the characteristic time scale in the solid is usually about orders of magnitude larger than in the fluid. Due to the computation of both fields at a small time step, the conjugate method is computationally less efficient than the second approach, the coupled method. In this method, the fluid and the solid field are solved by separate solvers. The fluid field is solved and interrupted after some time steps in order to renew the boundary conditions at the interface to the solid domain which is computed by a steady state approach. By using two different solvers for the solid and the fluid, the coupled method provides an opportunity to treat the different appearing time scales computationally more efficient, although an iterative procedure is needed between the fluid and the solid solvers.

The complex, unsteady flows in cooling channels affect the heat transfer coefficient. Reynolds Averaged Navier-Stokes (RANS) methods are not able to reproduce those complex flow conditions. Large Eddy Simulations (LES), which resolve a part of the turbulent spectrum, provide more accurate results to predict the heat transfer [5].

2. Objectives

After reviewing literature and the state of the art, we aim to solve the CHT problem in cooling channels with a coupled approach using LES for the flow computation in order to achieve more accurate results in comparison with RANS simulations. Since LES are more expensive than RANS, we aim to accelerate the process of the coupled computations by developing a method which takes the different characteristic time scales of the solid conduction and the flow convection into account.

Finally, after validating our numerical approach with analytical solutions and existing experimental investigations [6], we aim to study rib roughened cooling channels and the influence of different parameters of the turbulators on the heat efficiency and the pressure drop.

Acknowledgments

The research leading to these results has received funding from the European Community's Seventh Framework Programme (FP7, 2007-2013), PEOPLE programme, under the grant agreement No.FP7-290042 (COPAGT project).

References

[1] B. Lakshminarayana, Fluid Dynamics and Heat Transfer of Turbomachinery, John Wiley & Sons, Inc., Hoboken, NJ, USA, 2007.

[2] J.-C. Han, S. Dutta, S. Ekkad, Gas turbine heat transfer and cooling technology, Taylor & Francis, 2001.

[3] A. Heselhaus, A hybrid coupling scheme and stability analysis for coupled solid /fluid turbine blade temperature, in: ASME, International Gas Turbine & Aeroengine Congress & Exhibition, 43rd, Stockholm, Sweden, 1998.

[4] T. Verstraete, Multidisciplinary Turbomachinery Component Optimization Considering Performance, Stress, and Internal Heat Transfer, Ph.D. thesis, Universiteit Gent (2008).

[5] F. Duchaine, F. Wlassow, G. Leroy, N. Gourdain, Advanced nmerical simulation dedicated to the prediction of heat transfer in a highly loaded turbine guide vane., in: Proceedings of ASME Turbo Expo: Power for Land, Sea and Air, 2010.

[6] L. Casara, T. Arts, Experimental investigation of the aerothermal performance of a high blockage rib-roughened cooling channel, ASME Journal of Turbomachinery 127 (2005) 580–588.

Heat Transfer in High Subsonic Velocity Environments behind the Fan of a Gas Turbine

Francesco Baldani

Mechanics Department, Belgium Royal Military Academy, Belgium, francesco.baldani@rma.ac.be

Supervisor: Tony Arts

Professor, Head, Turbomachinery and Propulsion Department, von Karman Institute for Fluid Dynamics, Belgium, arts@vki.ac.be.

Supervisor: Walter Bosschaerts

Professor, Head, Mechanics Department, Belgium Royal Military Academy, Belgium, Walter.Bosschaerts@rma.ac.be

University Supervisor: Souad Harmand

Professor, Head, Fluid Dynamics and Heat Transfer Department of the TEMPO Lab, Valenciennes and Hainaut-Cambresis University (France), Souad.harmand@univ-valenciennes.fr

Abstract

The aim of the project is to propose a methodology to retrieve the heat flux through a finned heat exchanger placed downstream of the fan of a turbine jet engine. The core of the Ph.D. study is the solution of the so called Inverse Heat Conduction Problem (IHCP). To solve the IHCP the surface temperature of the heat conducting body has to be used as boundary condition of the problem. The Infra Red thermography is used to measure the heat exchanger surface temperature. The experiments are performed at low speed and at high subsonic speed, the latter in a blow-down wind tunnel capable to reach Mach numbers of the order of 0.75. The flow field in the blow-down wind tunnel test section is characterized by exploiting the Constant Temperature Anemometry (C.T.A.) technique. In order to be able to perform multi-point measurements, an 'ad-hoc' hot-wire probes support has been conceived and manufactured.

Keywords: Inverse Heat Conduction Problem, High Subsonic Speed, Infra Red Thermography, Constant Temperature Anemometry, hot-wire probes support

1. Introduction

The improvements in the manufacturing techniques as well as in the available materials push the aero-thermal engineers to find better solutions in order to improve engine performance. Indeed, improving turbine engine performance for military and civil purposes has a deep impact on thermal efficiency, fuel consumption, life-time and consequently allows the new environmental, noise and emissions standards to be met.

The aim of the project is to study the heat transfer from a hot surface to a cold flow under conditions similar to those encountered by aircraft turbine engines, hence using the main flow of the engine to study a heat exchanger placed just downstream of the fan. The main part of the research project deals with the solution of the "inverse heat conduction problem" which consists of imposing the object surface temperature as boundary condition and computing via numerical methods the resulting heat flux. The heat transfer coefficient is to be studied both locally and globally, since a global study of h is fundamental in the preliminary design phase while a local study of h is useful to understand the effects of the geometry on the local flow conditions (i.e. the turbulence intensity level) and on the achievable heat exchange.

We should remind that in the case of forced convection the flow is influenced by the amount of heat injected and that the flow rate versus the heat power in-

jected is one of the major triggers for the flow that develops. On top of this the conduction within the plate adds up with the heat convection from the surface.
It should also be clear that in order to deepen the understanding of the heat transfer occurring in installations such as finned heat exchangers one always has to consider that a simple superposition of the heat exchange phenomena is not enough. Indeed, one should rather talk of "conjugate" heat transfer, which is the actual coupled interaction of conduction and convection. Neglecting the effect of the wall conduction, for instance, will result in imposing unrealistic thermal boundary conditions at the solid-fluid interface since this greatly affects the temperature distribution. This leads to wrong heat transfer rates and coefficients.
For all these reasons the characterization of the wind tunnel test section flow field is a crucial issue. This is why the C.T.A. technique is chosen to characterize the flow field obtainable in the wind tunnel.

2. Conjugate Heat Transfer Concept

Since the studies conducted by Perelman[1] the importance of imposing correct boundary conditions when dealing with heat transfer problems involving a solid submerged in a flowing fluid is well known. Indeed, it is proven that in the presence of large thermal gradients (in space) and if the fluid encounters obstacles (rib, fin, etc..) the thermal boundary conditions imposed (uniform T_{surf}, uniform heat flux) in the classical study (purely convective) are unrealistic.It is therefore very important imposing the correct boundary conditions at the solid-fluid interface. The theory of choice is the conjugate heat transfer theory. It is based on the concept that the effects of the solid domain conduction have to be coupled with the convection phenomenon happening over the solid surface. The idea is to perform surface temperature measurements of the finned heat exchanger under analysis with the I.R. thermography technique after having characterized the wind tunnel test section flow field exploiting the C.T.A. technique and/or the P.I.V. technique in order to be able to impose the correct boundary conditions for computing the surface heat flux distribution (via commercial FEM solvers or as proposed hereafter via a numerical solution of the so obtained Inverse Heat Conduction Problem)[2; 3; 4].

3. Transient Inverse Heat Conduction Problem

Determining local convection coefficients accurately or performing accurate local heat flux measurements is a hard and expensive task but for many cases the heat flux distribution is an indispensable parameter. For finned heat exchangers this task is particularly challenging [5; 6; 7]. Indeed heat transfer measurements at the fin base would introduce a thermal resistance between the primary surface and the fin due to the presence of the measurement device. Therefore the heat fluxes at the fin base have to be determined indirectly by measuring the heat fluxes through the extended surface and the primary surface. Among the available techniques to perform such measurements (heat flux sensors, local temperature measurements) the inverse heat conduction technique is probably the most suitable for our study. It is mainly used to estimate temperatures or heat fluxes at surfaces that are inaccessible for measurements. The advantage of this method is that the experimental studies can be performed under similar conditions and similar environment as during the operation. To solve an inverse heat conduction problem, a mathematical optimization method is required, which uses temperature measurements as input. Based on surface temperatures of a solid object, heat fluxes on one or more surfaces of the object can be estimated, so the need for internal temperature measurements can be omitted. Depending on the temperature measurement technique, the disturbance of the local temperature fields and heat flux distribution is limited or even absent. It also has the advantage that the temperature field in the whole object can be reconstructed based on surface temperature measurements, together with the coupled heat flux distribution. The proposed code allows the determination of the local convective heat exchange coefficient h(x,y,t), taking into account the conductive flux in the heated plate. In general the heat flux can rise and fall abruptly and can be both positive and negative where negative values indicate heat losses from the surface. According to Beck, Blackwell and St.Clair [8] the source of heating is immaterial to the IHCP procedures. Mathematically the IHCP (for the 1-D case) can be described as in the set of equations 1 to 4.

$$\frac{\partial}{\partial x}\left(k\frac{\partial T}{\partial x}\right) = \rho c\frac{\partial T}{\partial t} \tag{1}$$

Where the thermal conductivity k, the density ρ and the specific heat c are postulated to be known functions of temperature.

$$T(x,0) = T_0(x) \tag{2}$$

$$\frac{\partial T}{\partial x} = 0 \; at \; x = L \tag{3}$$

One can rewrite the temperature at the first location at one time as in equation 4.

$$T(x_1, t_i) = Y_i \tag{4}$$

The objective is to estimate the surface heat flux at discrete times, t_i, from

$$q(t_i) = -k \left. \frac{\partial T(x, t_i)}{\partial x} \right|_{x=0} \tag{5}$$

After the paper by Beck, Blackwell and Haji-Sheikh [9], where a review of some inverse heat conduction methods can be found, the chosen method to solve the IHCP is the so called 'function specification method' (FSM). The FSM has the advantage to be simple in concept and to not change the physics of the problem since the intrinsic parabolic nature of the problem is unchanged. The FSM is sequential in nature and thus computationally efficient and moreover the measurements in the distant future do not affect the 'present' estimates as for other methods [9]. The FSM can be used for linear and nonlinear problems and finite differences, finite elements or numerical convolution can be used. The method itself consists in minimizing, with respect to the heat flux q_M the sum of squares function as described by Eq. 6[9]. The equations 6 to 11 refer to measurements acquired by one sensor over multiple time steps.

$$S_M = \sum_{i=1}^{r} = (Y_{M+i-1} - T_{M+i-1})^2 \tag{6}$$

which involves the times $t_M,\ t_{M+1},\ \ldots,\ t_{M+r-1}$. Hence 'future' information is used to obtain q_M. Some functional form for $q(t)$ for t_M to t_{M+r-1} is selected, the simplest being

$$q_{M+1} = q_M, \; i = 1, 2, \ldots, r \tag{7}$$

The calculated temperature T_{M+i-1} is expanded in a Taylor series for q_M obtaining

$$T_{M+i-1} = T_{M+i-1}|_{\hat{q}_M} + X_{M+i-1,M}(q_M - \hat{q}_M) \tag{8}$$

where $X_{M+i-1,M}$ is the sensitivity coefficient defined by

$$X_{M+i-1,M} = \frac{\partial T_{M+i-1,M}}{\partial q_M} \tag{9}$$

the resulting algorithm after minimizing Eq. 6 with respect to q_M is

$$\hat{q}_M = \hat{q}_{M-1} + \frac{\sum_{i=1}^{r} \left[Y_{M+i-1} - T_{M+i-1}|_{q_M=\cdots\simeq\hat{q}_M} \right] X_{M+i-1,M}}{\sum_{i=1}^{r} X_{M+i-1,M}^2} \tag{10}$$

Only $\hat{q}_M$ is retained for time t_M, and M is increased by one and the procedure is repeated. The iterative regularization method minimizes the whole domain function

$$S_M = \sum_{i=1}^{I} = (Y_i - T_i)^2 \tag{11}$$

where I is the total number of measurements. It should be noticed that in our analysis we use multiple sensors (i.e. surface temperature cartography $T(x, y, t)$ measured by the I.R. camera). Anyway this does not affect the exposed solution methodology but just the mathematical formalism.

3.1. IHCP Solution Validation

One can validate the proposed solution methodology for a flat plate of very thin thickness in a laminar flow. The validity of the proposed solution can be checked by solving twice the direct model via a CFD software (*Fluent*© in our case). We compute first the heating phase with equations 17 to 22. In Eq. 17 the heat transfer coefficent h is computed from the Nusselt correlation (see equations 12 to 16).

$$Nu = 0.332 \cdot Re^{1/2} \cdot Pr^{1/3} \tag{12}$$

Equation 12 can be rewritten as follows to take into account for the Nusselt number evolution along the plate:

$$Nu(x) = \frac{0.332 \cdot Re(x)^{1/2} \cdot Pr^{1/3}}{\left[1 - \left(\frac{x_0}{x}\right)^{3/4}\right]^{1/3}} \tag{13}$$

If we take $x_0 = 0$ then the equation 13 reduces to:

$$Nu(x) = 0.332 \cdot Re(x)^{1/2} \cdot Pr^{1/3} \tag{14}$$

Since fluid properties (such as viscosity, diffusivity, etc.) can vary significantly with temperature, there can be some ambiguity as to which temperature one should use to select property values. The recommended approach is the use of the average of the wall and free-stream temperatures, defined as the film temperature $T_{film} = \frac{T_{surface} + T_{air}}{2}$.

Now recalling that the Nusselt number can be also expressed as reported in equation 15 we will be able, once $Nu(x)$ is known, to compute $h(x)$ as from equation 16.

$$Nu(x) = \frac{h(x) \cdot x}{k_{air}} \tag{15}$$

$$h(x) = \frac{Nu(x) \cdot k_{air}}{x} \tag{16}$$

The equation 12 holds for a laminar, isothermal, local situation with $Pr > 0.6$ which is the situation we will deal with imposing a flow velocity (U_∞) of 10 m/s and a flow bulk temperature (T_∞) of 18° C.

$$(dzdxdy)\,\lambda\left(\frac{\partial^2 T}{\partial x^2} + \frac{\partial^2 T}{\partial y^2}\right) + P\,(dzdxdy) \quad = \quad \rho c_p \frac{\partial T}{\partial t}\,(dzdxdy) + hdxdy\,(T - T_\infty) \tag{17}$$

with as initial condition

$$T\,(x, y, 0) = T_0 \tag{18}$$

and as boundary conditions

$$-\lambda \left.\frac{\partial T}{\partial x}\right|_{x=0} = 0 \tag{19}$$

$$-\lambda \left.\frac{\partial T}{\partial x}\right|_{x=L} = 0 \tag{20}$$

$$-\lambda \left.\frac{\partial T}{\partial y}\right|_{y=0} = 0 \tag{21}$$

$$-\lambda \left.\frac{\partial T}{\partial y}\right|_{y=H} = 0 \tag{22}$$

The result of this first direct simulation is the surface 'hot' reference temperature cartography $T\,(x, y, t_1) = T_1$. The second direct simulation is performed to compute the cooling phase and therefore to retrieve the surface 'cold' reference temperature cartography $T\,(x, y, t_2) = T_2$ (exploiting Eq. 23 and equations 18 to 22).

$$(dzdxdy)\,\lambda\left(\frac{\partial^2 T}{\partial x^2} + \frac{\partial^2 T}{\partial y^2}\right) \quad = \quad \rho c_p \frac{\partial T}{\partial t}\,(dzdxdy) + hdxdy\,(T - T_\infty) \tag{23}$$

It is now possible to use T_1 and T_2 as boundary conditions for the solution of the IHCP. The obtained result is reported in Figure 1.

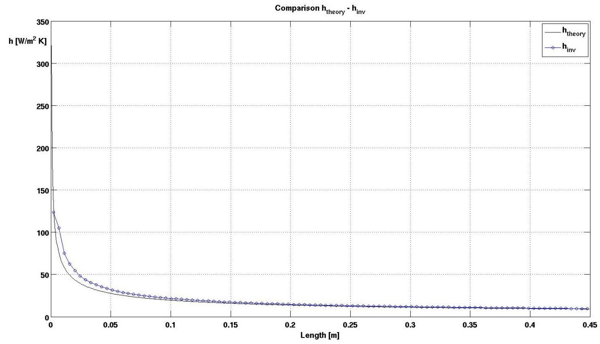

Figure 1: Theory - IHCP solution Comparison

4. Experimental Facilities and Set-up

The facility used for the high speed experiments is a blow-down wind tunnel where the air coming from a pressurized tank can be heated.
A velocity $U_{mean} \approx$ 30-230 *m/s* with a flow temperature $T_{mean} \approx$ 290-320 *K* are flow conditions that can be considered satisfying the similarity rules to those appearing at the inlet of an aircraft engine during various flight conditions. See Figure 2 for the working scheme of the installation. The test section sketch and the installation of the measuring tools are sketched in Figure 3.

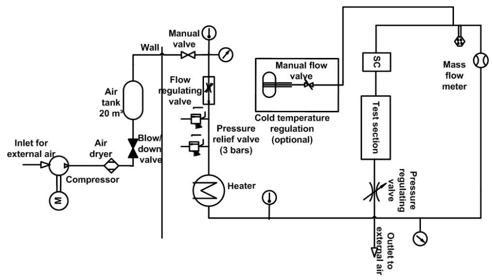

Figure 2: Facility Working Principle Diagram (Courtesy of ULB)

The experimental set-up for the low speed experiments is shown in Figure 4. In the picture it is possible to see the I.R. camera used to acquire the surface thermographs, a hot-wire rake used to check the test section velocity and the heating resistance together with its power supply.

5. Experimental Campaigns and Data Analysis

The following sections summarize the sets of experimental campaigns that have been conducted in order to characterize the high speed wind tunnel test section

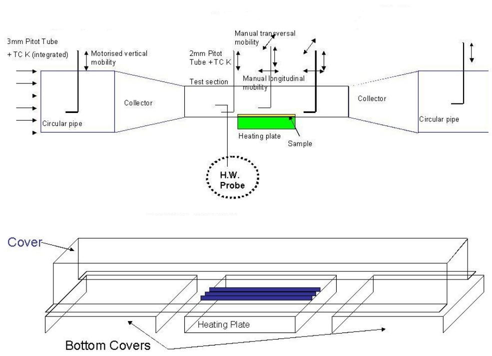

Figure 3: Test Section and Measuring Tools Installation Sketch (Courtesy of ULB)

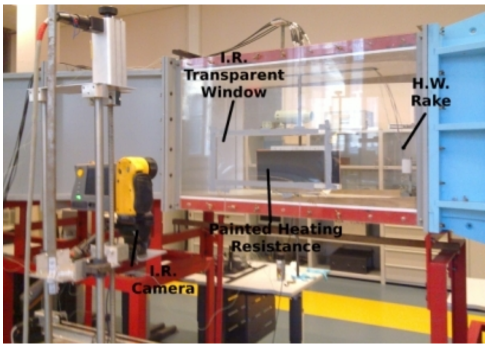

Figure 4: I.R. Low Speed Experiments setup

flow field and to validate the inverse heat conduction problem solution method.

5.1. High Speed Experimental Campaign

The aim of the high speed experimental campaign is to characterize the blow-down wind tunnel flow field via the C.T.A. technique. Using hot-wire probes five different regimes of interest are investigated. A second experimental campaign is performed to measure the velocity profile and the effect of the presence of a finned heat exchanger in the section. A third series of experiments is performed to test the capabilities of a manufactured hot-wire probes rake.

5.1.1. Mean Flow Field Measurements

The tests are performed with a plane bottom wall. The five investigated regimes classified according to the velocity and the mean total temperature of the fluid in the test section are summarized in table 1.

5.1.2. Traverses Experiments

This experimental campaign is performed with the finned heat exchanger placed in the test section but

Regime #	U_{mean}	T_{total}
1	230 m/s	315 K
2	160 m/s	305 K
3	130 m/s	300 K
4	60 m/s	295 K
5	30 m/s	295 K

Table 1: Tested Regimes

with no heat injection (i.e. no heat exchange between the finned surface and the flow) during the measurements. The experiments consist in hot-wire probe traverses in order to measure the velocity profiles before and after the prototype. The sketch in Figure 5 shows the positions and the locations where the experiments are performed.

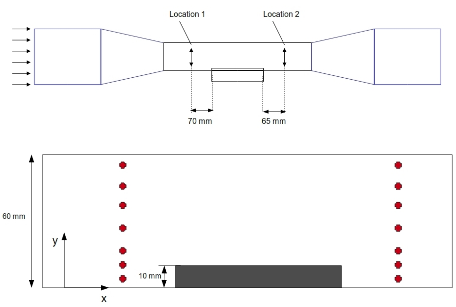

Figure 5: H-W. Traverses Experiments

According to the frame of reference shown in Figure 5 the positions analyzed for the two locations are: y = 6-11-16-26-36-46-56 *mm*. The measurements in the two locations are performed during two different experiments.

5.1.3. Hot-wire Rakes

A major issue while performing the traverses experiments is to keep the flow conditions perfectly constant in order to let the moving probe face the same flow field. To overcome this problem a design for a hot-wire probes rake is proposed, so that the velocity could be measured in different positions at once.

The designed support is based on a well known *NACA* 4 digits symmetrical wing. The manufactured 3 probes support installed in the test section can be seen in Figure 6. The reasons why after some preliminary studies a symmetrical wing based on a NACA-0025 airfoil is chosen are reported next. The support has to be inserted in a high velocity environment, which

Figure 6: Manufactured 3 Probes Support

means that important forces could occur. Therefore, to greatly reduce the forces acting on the rake, and consequently the need for stout holders any kind of shape creating important drag forces should be avoided. The area facing the flow should be as small as possible to reduce the blockage and consequently the interference with the free flow. Additionally when dealing with velocities of the order of 230 *m/s* reducing the vibrations of the support becomes also very important. The adopted solution besides satisfying the above mentioned requirements allows also to minimize the wake size drastically reducing the interference effects on other measuring tools installed behind the rake itself. After the validation of the 3 probes support we decided to manufacture a 5 probes support that could grant the vertical velocity profile measurement of the whole test section at once.

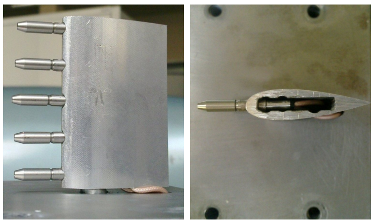

Figure 7: Manufactured 5 Probes Support

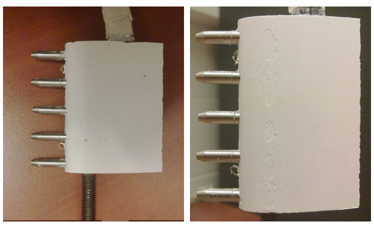

Figure 8: Manufactured 5 Probes Support (Plaster)

In the rake shown in Figure 7 the probes are installed at a distance of 12.5 *mm* from each other. In Figure 8 we can see the last version of the H.W. rake, prepared with molding plaster and where two thermocouples have been embedded in the support. This probe support has been tested only at low speed.

5.2. C.T.A. Data Analysis

When dealing with signals like those obtainable with the C.T.A. one can perform mainly three kind of analysis:

1. Descriptive static statistic analysis:
    - averaged values
    - skewness, kurtosis
    - variance, standard deviation
2. Spectral analysis
3. Signal correlation analysis
    - autocorrelation
    - cross-correlation

Since the C.T.A. technique is an indirect measurement technique a calibration law is required. Calibration units are available for this purpose, letting us associate to a known velocity the voltage measured by the hot-wire probe [10]. But this procedure cannot be exploited to analyze the data when the temperature varies during the measurements. Since the environment in which the hot–wire probe is placed is characterized by rather significant temperature variations, 6/7 *K* during the same regime and from 320 *K* to 295 *K* from the beginning to the end of a complete run, rather than a calibration curve a calibration surface with the temperature as additional variable would be required. The biggest issue to obtain such a calibration surface is that a dedicated wind tunnel is needed, where both the velocity and the flow temperature can be controlled. The one available at the Royal Military School can reach a maximum velocity of 30 *m/s* under controlled temperature conditions but during the experiments the velocity ranges between 40 *m/s* and 230 *m/s*. Therefore an alternative calibration procedure is needed. The "in-situ" calibration proposed consists in extracting the measured voltage, velocity and temperature for each investigated flow regime. The raw voltages are then corrected in temperature according to equation 25 and an iterative procedure implemented in *Matlab*© computes simultaneously the *"reference King's Law coefficients"*. The basic idea is to retrieve a "unique" calibration law that can be used even if the temperature is changing, the scheme in Figure 9 presents the strategy to obtain the proposed calibration curve.

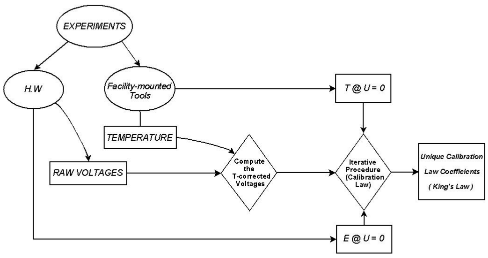

Figure 9: Unique Calibration Law Procedure Logical Scheme

In this way it is possible to perform experiments and exploit the acquired data to obtain a calibration law that is corrected in temperature. Equation 24 shows the King's law while in equation 25 the correction applied before linearization of the data is reported [11].

$$E_{corr}^2 = A_{ref} + B_{ref} \cdot U^{n_{ref}} \tag{24}$$

$$E_{corr} = E_{meas} \cdot \left(\frac{T_w - T_{ref}}{T_w - T_a} \right)^{0.5 \cdot (1 \pm m)} \tag{25}$$

where T_w is the wire temperature, T_{ref} is the reference temperature (in this case the temperature in the test section immediately before the experiment), T_a is the ambient temperature, measured by the facility mounted instrumentation. The parameter m is called *"Temperature Loading Factor"* and is suggested by Dantec for temperature correction purposes, it should be kept between 0.2 and 0.3 and added or subtracted depending on whether T_a is bigger or smaller than T_{ref} respectively. An example of the resulting "unique" calibration law is reported in Figure 10.

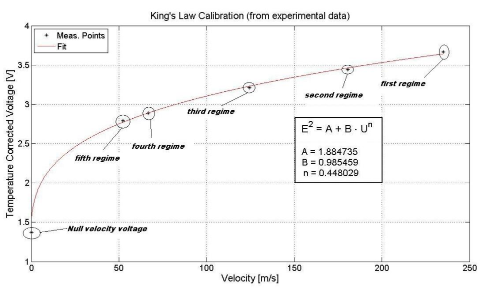

Figure 10: Unique Calibration Law Example

5.2.1. *Correction for Fluid Temperature Drift*

To obtain the actual velocities the reference King's law coefficients are "tuned" according to the measured fluid temperature. The corrected King's law coefficients are computed as described by the set of equations 26.

$$\begin{cases} A_{corr} = \left(\dfrac{T_w - T_a}{T_w - T_0} \right)^{(1 \pm m)} \cdot \dfrac{K_{f_a}}{K_{f_0}} \cdot \left(\dfrac{Pr_{f_a}}{Pr_{f_0}} \right)^{0.2} \cdot A_{ref} \\ B_{corr} = \left(\dfrac{T_w - T_a}{T_w - T_0} \right)^{(1 \pm m)} \cdot \dfrac{K_{f_a}}{K_{f_0}} \cdot \left(\dfrac{Pr_{f_a}}{Pr_{f_0}} \right)^{0.33} \cdot \\ \qquad \cdot \left(\dfrac{\rho_{f_a}}{\rho_{f_0}} \right)^{n} \cdot \left(\dfrac{\mu_{f_a}}{\mu_{f_0}} \right)^{-n} B_{ref} \end{cases} \tag{26}$$

The physical air properties in equation 26 are computed at the temperatures T_{f_a} and T_{f_0} respectively the ambient and reference film temperatures obtainable as follows:

$$\begin{cases} T_{f_a} = \dfrac{T_w + T_a}{2} \\ T_{f_{ref}} = \dfrac{T_w + T_{ref}}{2} \end{cases} \tag{27}$$

So after the correction the King's calibration law should be rewritten as follows:

$$E^2 = A_{corr} + B_{corr} \cdot U^n \tag{28}$$

Eventually the velocity in the wind tunnel test section is computed as reported by the expression in equation 29.

$$U = \left(\frac{E^2 - A_{corr}}{B_{corr}} \right)^{\dfrac{1}{n}} \tag{29}$$

5.3. *Low Speed Experimental Campaign: I.R. Analysis*

The aim of the low speed experimental campaign is to validate the methodology and the tools to be used to solve the IHCP. In a low speed wind tunnel a quasi-2D heating resistance has been placed in the test section and surface thermographs are recorded [12] in order to exploit a numerical procedure capable to compute the heat conduction coefficient. The analysis of the requirements and of the constraints led to the conception of the experimental model as sketched in Figure 11.

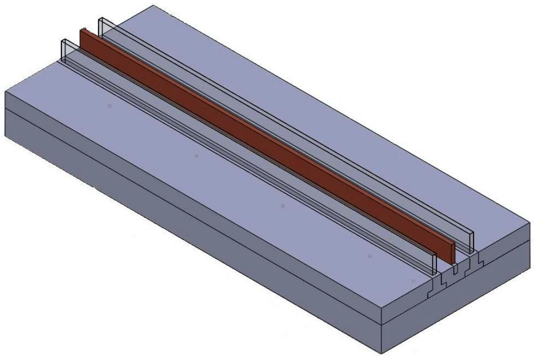

Figure 11: Experimental Model Conception Sketch

The real heat exchanger is reproduced by means of a central fin, made of copper and acting as heating resistance. On the two sides of this central fin is placed a set of two fins made of I.R. transparent material (CaF_2 for instance). The idea is to exploit the prototype symmetry in order to simplify its testing model. Additionally using a heating resistance as central fin allows us to know and control the heat injected.
According to the mentioned needs the proposed procedure to perform the experiments can be summarized as follows:

1. Heat the central fin up to the maximum allowed temperature
2. Open the facility valve in order to reach a stabilized velocity
3. Increase the heating power injected in the fin according to the velocity increase in order to keep the heating resistance at a constant temperature
4. Once the velocity and the fin T_{surf} are stabilized acquire a reference surface thermograph (hot surface)
5. Switch off the heating resistance
6. Record the fin T_{surf} evolution with the I.R. camera (cold surface)
7. Solve the IHCP via the numerical calculation

For what concerns the experiments presented in this work one should remind that the configuration proposed in Figure 11 has been replaced by a stand alone very thin (0.25 mm) but with a bigger surface (170 x 450 mm) heating resistance for a sake of simplicity. The heating resistance is of the order of 20Ω and it is fed with 12 $Volts$. The flow velocity in the wind tunnel test section is 10 m/s. The above mentioned procedure is then applied as described.

5.4. *I.R. Experiments Data Analysis*

The code exploited to solve the IHCP needs to be fed with a matrix of data representing the thermograph acquired by the I.R. camera. Therefore once recorded, the images must be prepared in order to be used as boundary conditions for the numerical method proposed. The rebuilding procedure could be summarized as follows:

1. An I.R. image where the color map palette is present is needed in order to be able to know the color levels to be linked to the temperature levels (see Figure 12).
2. Retrieve a vector able to translate the R(ed)-G(reen)-B(lue) data contained in the I.R. images into a matrix containing the surface temperature.
3. Pick up conveniently a frame from the recorded I.R. video, this will be the cold surface and fix the time step for the numerical solution (see Figure 13).
4. Translate the image into a *Matlab*© exploitable matrix.
5. Crop the image in order to contain only the surface of interest (i.e. only the flat plate and not the supports, etc. . . .), see Figure 14.

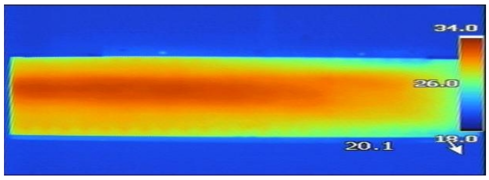

Figure 12: Color Vs. Temperature Levels

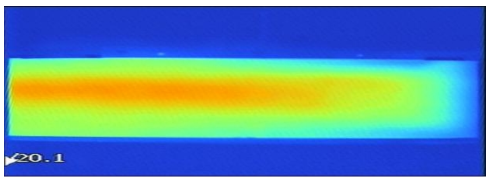

Figure 13: Cold Surface I.R. Image

Once prepared the I.R. images for the analysis one should just insert the right surface dimensions, time step and material characteristics in the script and feed the script with the hot surface and the cold surface informations matrices [13].

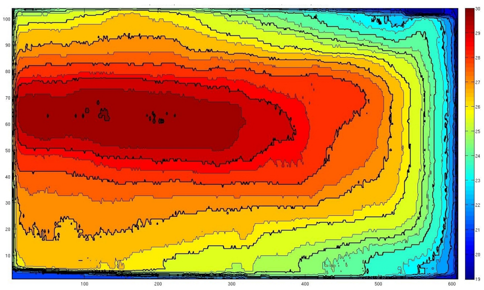

Figure 14: Cropped and Translated Image Example

6. CFD Low Speed Simulation

The purpose of these simulations is to check the behavior of the hot-wire probes support when inserted in the flow field. For this work the calculations have been used also to define the distance at which should be placed the heating resistance used for the I.R. experimental campaign. Indeed it is important to reduce at the maximum the influence of the wake released by the probe rake so that the recorded I.R. images depict the actual situation of a "hot" object submerged by an undisturbed "cold" flow. In Figure 15 is reported the geometry used to perform the simulations, it is possible to notice that the probe prongs and the wires are not modeled.

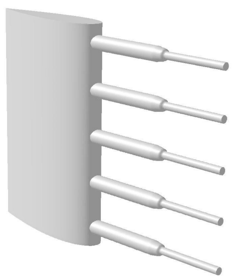

Figure 15: H.W. Rake Model

The model is created with the open source software K-3D ($http://www.k-3d.org/$) while the mesh is produced with the automatic mesher $HEXPRESS^{TM}/Hybrid$. The calculations have been performed with the commercial solver *Fluent*©. The domain reproducing the R.M.A. wind tunnel test section (60 *cm x* 60 *cm x* 120 *cm*) is of about two millions cells. The 3-D steady state simulations have been performed using a standard $k-\epsilon$ turbulence model and the *Fluent*© enhanced wall treatment option enabled. The discretization schemes used are the *Fluent*© standard scheme for the pressure and the first order upwind scheme for the momentum, the turbulent kinetic energy and the turbulent dissipation rate. The velocity used for the simulation is the same as the one used for the I.R. test, 10 m/s.

7. Results

In this section the obtained results are presented. The flow field analysis of the blow-down wind tunnel are presented first. The low speed I.R. analysis experiment are only partially presented as they are performed for validation purposes and the whole methodology could not be fully discussed in this article. Eventually are presented the numerical simulations of the H.W. rake behavior performed at low speed.

7.1. Mean Flow Field Results

It is of crucial importance to characterize the turbulence in the testing chamber, the size of the turbulent scales and the frequency content. In the following table the results of the static statistic analysis and of the autocorrelation analysis are summarized [14; 15; 16; 17; 18]. The results for each flow regime are resumed in Table 2.

Table 2: EXPERIMENTAL CAMPAIGN RESULTS RESUME

Regime	***1***	***2***	***3***	***4***	***5***
U_{meas} $[m/s]$ (Pitot)	226.29	180.65	126.35	72.33	45.33
U_{comp} $[m/s]$ (H.W.)	234.19	170.57	123.10	71.04	47.26
Uncertainty $[m/s]$	±4.47	±4.44	±4.08	±0.99	±0.35
Uncertainty %	1.91	2.60	3.32	1.39	0.74
Re_d	42.25	31.25	22.81	13.31	8.91
Mach number	0.66	0.49	0.35	0.21	0.14
T_{mean} $[K]$	≈ 315	≈ 307	≈ 301	≈ 296	≈ 293
R.M.S.	5.615	3.398	2.846	1.753	1.267
Variance	31.523	11.549	8.098	3.072	1.604
Turbulence Intensity %	2.397	1.992	2.312	2.467	2.680
Skewness	-0.695	-0.506	-0.320	-0.314	-0.286
Kurtosis	3.655	3.791	3.483	3.565	3.512
Int. Length Scale $[mm]$	37.897	38.572	41.617	20.740	19.330
Taylor Micro Scale λ $[mm]$	6.795	4.855	4.163	2.739	2.468
Dissipation Rate ϵ $[m^2/s^3]$	283.83	200.56	189.11	163.86	104.82
Kolmogorov Length Scale η $[mm]$	0.0931	0.1003	0.1010	0.1038	0.1155

The frequency analysis is performed exploiting the F.F.T. (Fast Fourier Transform) algorithm of Matlab which uses a special version of the discrete Fourier transform to filter the data. The error analysis for the presented results is performed according to the error propagation theory (the Kline-McClintock approach) always using a confidence interval of the 95%.

7.2. Hot-wire Traverses Results

The measures, coupled with pressure measurements, allow computing the pressure losses caused by the presence of the heat exchange. The test conditions repeatability being one of the main issues, the results presented cannot be retained as quantitatively precise. This is especially true since the traverses at the two locations have been performed during two different tests. However the experimental campaign gives meaningful information about the general flow field behavior [19].

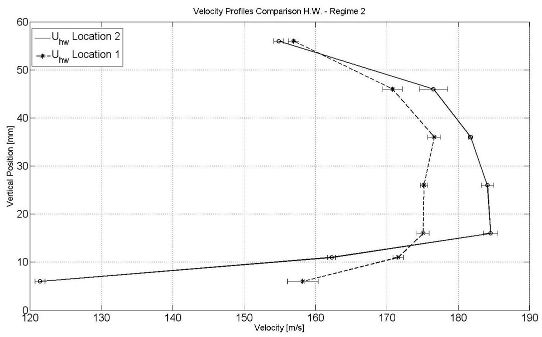

Figure 16: Velocity Profiles - H.W. Measures

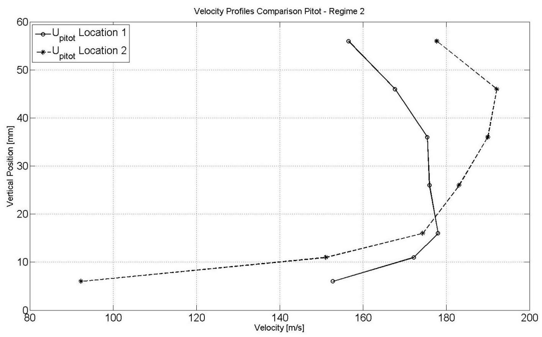

Figure 17: Velocity Profiles - Pitot Measures

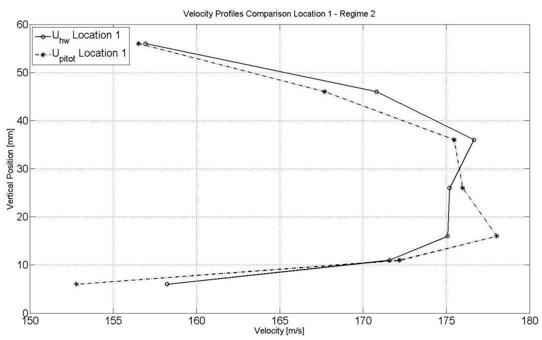

Figure 18: Velocity Profiles - Location 1, H.W. - Pitot Comparison

From Figure 18 and Figure 19 we can notice a discrepancy between the measurements performed with

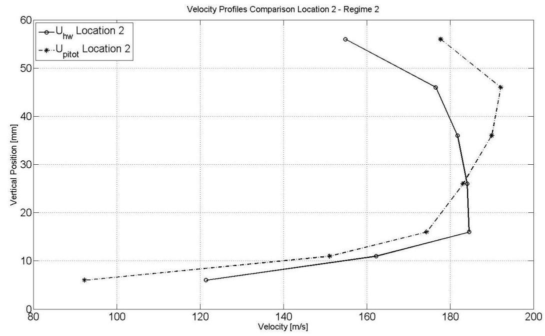

Figure 19: Velocity Profiles - Location 2, H.W. - Pitot Comparison

the hot-wire and the Pitot tube that seems to be mainly due to the fact that the wind tunnel is a blow-down facility. In facts with such facilities one of the biggest issues is to be certain to have exactly the same flow conditions for enough time to perform a full traverse analysis. If we compare these results with the results in table 3 it is clear that performing multi-point measurements gives much more reliable measurements since we are certain that the flow conditions will be the same.

7.3. Hot-wire Rake Results

Since the wind tunnel is exploited in parallel by ULB and some modifications have been performed on it the results obtained with the hot-wire rakes should not be compared with above reported results. The main purpose of the performed experiments is to validate the manufactured rakes.

Regime	***Position***	U_{meas} Pitot	U_{meas} H.W.
1	1	$\approx 205.04\ m/s$	$\approx 205.64\ m/s$
	2	$\approx 207.01\ m/s$	$\approx 207.95\ m/s$
	3	$\approx 201.64\ m/s$	$\approx 203.40\ m/s$
2	1	$\approx 177.59\ m/s$	$\approx 171.01\ m/s$
	2	$\approx 173.34\ m/s$	$\approx 173.70\ m/s$
	3	$\approx 169.77\ m/s$	$\approx 170.78\ m/s$
3	1	$\approx 120.89\ m/s$	$\approx 121.88\ m/s$
	2	$\approx 124.40\ m/s$	$\approx 125.97\ m/s$
	3	$\approx 119.61\ m/s$	$\approx 124.54\ m/s$

Table 3: H.W. Rake 3 Probes Vs. Pitot

In table 3 are reported the velocities measured with the 3-probes support and a Pitot tube at the same positions but at a different distance from the test section inlet during the same test. It is easy to understand as the possibility to simultaneously measure the whole velocity profile drastically reduce the uncertainty linked to the capacity of maintaining exactly the same flow conditions for a long period of time. Therefore the accuracy of the velocity profiles measured with the rake is much higher and the profile shape gives indications on the actual test section flow field being not linked to the wind tunnel working parameters controlled by the operator.

7.4. CFD Simulation Results

In Figure 20 is plotted the computed velocity profile along the x-axis extracted from the wing trailing edge to the end of the numerical domain.

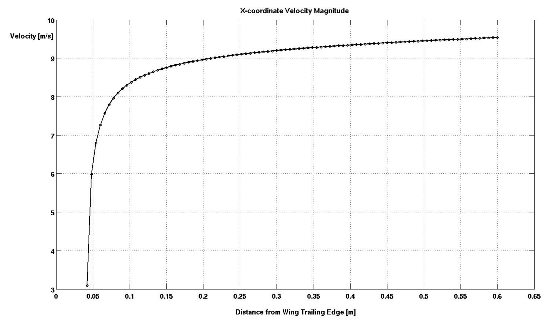

Figure 20: X-coordinate Velocity Plot

It is possible to notice that after 35 cm the influence of the rake wake starts being negligible, this why the heating resistance used for the I.R. experiment has been placed at about 40 cm from the probe support.

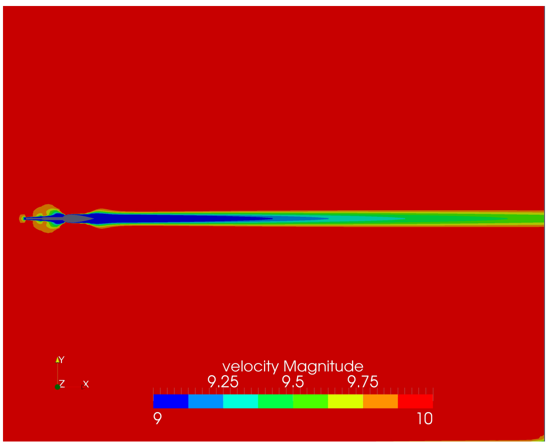

Figure 21: CFD-computed Velocity Contour Plot

From the contour plot reported in Figure 21 it is possible to see the influence of the presence of the rake in the whole domain. The results obtained could be used for comparison with oil flow visualization. This will be more interesting when moving to the high velocity case as the oil visualization allows to clearly see if the transition to supersonic occurs and where the flow in case detach from the wing surface.

8. Conclusions

The analysis performed to check the flow field quality makes us assume that modifications should be performed on the wind tunnel. Indeed the very low turbulence level, together with the almost parabolic velocity profiles measured, let us assume that flow could probably not be fully developed when entering the test section. Though the absence of spectral peaks lets us deduce that the turbulence in the flow field is homogeneous and no frequency correlated structures are present (no vortex shedding or other phenomena). This leads to the conclusion that performing minor modifications should be enough to improve the flow field quality. The coupling of Pitot tube and hot-wire probe traverse measurements shows that the general behavior of the flow field is maintained almost constant. Nevertheless it also testifies that the wind tunnel is not able to reproduce exactly the same conditions (p_{tot} profile, U profile, etc..) for two consecutive tests. The tests performed with the hot-wire probes rake show the quality of the chosen support design in order to overcome the main issue affecting a blow-down facility: maintain exactly the same working conditions for a long period of time. Indeed the rake allowed us to measure the velocity at five different positions instantaneously without affecting significantly the flow field itself. The obtained results have been taken into account by the U.L.B. engineers while conceiving a revised version of the facility that is now under construction. The flow field of this new wind tunnel will be investigated in the next months.
For what concerns the numerical solution of the IHCP the validation test performed gave encouraging results. Though the lesson learned from the preliminary test performed is that one has to carefully prepare the experimental setup in order to reduce as much as possible the heat losses (very high thermal insulation on the sides and on the back face of the fin). Furthermore, preparing the experimental setup to work with a finned heat exchanger at high subsonic velocity will be even more challenging. Nevertheless the task to validate the methodology and develop a consistent approach to this kind of analysis can be considered as accomplished. The simulations performed over the H.W. probe rake have been very helpful to correctly

prepare the I.R. low velocity experimental setup. Additionally the geometry and the meshing procedure are now well established so that it will be easier to move to high subsonic velocity case.

9. Future Developments

One of the main and more imminent tasks will be to check the flow field quality in the revised version of the blow-down wind tunnel. Besides this task the capabilities of the H.W. rake made in plaster should be validated, indeed CFD simulations and flow oil visualization at high speed are scheduled in order to accomplish the task. The I.R. experiments proposed methodology and the proposed algorithm to solve the IHCP should be validated at low speed. Furthermore the procedure needs to be optimized for a flow reaching $M \approx 0.7$ where possible issues could be the very small amount of time to grab I.R. images, the flow stabilization, the fin temperature stabilization, etc ...

Acknowledgments

I would like to thankfully acknowledge the “TEMPO Laboratory“ of the University of Valenciennes guided by Professor Souad Harmand for giving me the opportunity to exploit their knowledge on the IHCP.

I also would like to sincerely thank the ULB research engineer Nicolas Heintz for the months of work performed together and the availability he showed.

References

[1] T. Perelman, On conjugated problems of heat transfer, International Journal of Heat Mass Transfer (Vol. 3, pp. 293-303).

[2] F. Kreith, Principles of Heat Transfer, second revised edition Edition, International Text Books in Mechanical Engineering, International Textbook Company Ltd, 158 Buckingham Palace Road London, 1965.

[3] P. H. Groeber, D. S. Erk, Fundamentals of Heat Transfer, third revised edition by dr. u. grigull Edition, McGraw-Hill Series in Mechanical Engineering, McGraw-Hill Book Company, INC., 1962.

[4] F. Coletti, A. Armellini, T. Arts, C. Scholtes, Aero-thermal investigation of a rib-roughened trailing edge channel with crossing jets - part ii: Heat transfer analysis, ASME paper No. GT2008 - 50695.

[5] A. Willockx, Using the inverse heat conduction problem and thermography for the determination of local heat transfer coefficients and fin effectiveness for longitudinal fins, Ph.D. thesis (2009).

[6] B. Cukurel, T. Arts, C. Selcan, Conjugate heat transfer characterization in a ribbed cooling channel, Conference Proceedings (ISAIF10-161).

[7] F. Coletti, Coupled flow field and heat transfer in an advanced internal cooling scheme, Ph.D. thesis (2010).

[8] J. Beck, B. Blackwell, C. S. C. Jr., INVERSE HEAT CONDUCTION - Ill-posed Problems, first edition Edition, International Text Books in Mechanical Engineering, Wiley Interscience Publication, 1985.

[9] J. Beck, B. Blackwell, A. Hoji-Sheikh, Comparison of some inverse heat conduction methods using experimental data, International Journal of Heat Mass Transfer (Vol. 39, pp. 3649-3657).

[10] Various, Measurement Techniques in Fluid Dynamics - An Introduction, second revised edition Edition, VKI Lecture Series, von Karman Institute, 2001.

[11] F. E. Jorgensen, How to measure turbulence with hot–wire anemometers, Dantec Dynamics, Tonsbakke 16-18, DK-2740 Skovlunde, Denmark, 2005.

[12] G. Cardone, T. Astarita, G. Carlomagno, Wall heat transfer in static and rotating 180 degrees turn channels by quantitative infrared thermography, Re. Gén. Therm. (37, 644-652).

[13] F. Baldani, W. Bosschaerts, R. Wagemakers, High velocities wind tunnel flow field investigation and heat exchanger infrared analysis. part 1: Experimental set-up, experiments and first results, Conference Proceedings (ISAIF10-11).

[14] H. Bruun, Hot–wire Anemometry, Principles and Signal Processing, Oxford University Press Inc., 1995.

[15] D. Hanson, K. Horan, Turbulence/cascade interaction: spectra of inflow, cascade response and noise (A98-30871).

[16] AIAA, Turbulence in Complex Flows: A Selected Review, AIAA, Reno, NV, 1992.

[17] AIAA, Preliminary Measurements of Velocity, Density and Total Temperature Fluctuations in Compressible Subsonic Flow, AIAA, Reno, NV, 1983.

[18] P. Stainback, K. Nagabushana, Review of hot-wire anemometry techniques and the range of their applicability for various flows, Electronic Journal of Fluids Engineering, Transactions of the ASME.

[19] F. Baldani, W. Bosschaerts, Turbulence measurements in a high subsonic non-isothermal flow field. turbine engines inlet conditions analysis, Conference Proceedings (ISABE-2011-1815).